Supplement to January / February 2024
Volume 53, Number 1

AppliedRadiology®
The Journal of Practical Medical Imaging and Management

Leaders on the Horizon Residents' Program 2023

Tej I. Mehta, MD
The Johns Hopkins Hospital

Monica M. Matsumoto, MD
University of Pennsylvania

Peterson Chang, MD
West Visayas State University Medical Center

Helena Bentley, MD
University of British Columbia

William Raynor, MD
Rutgers Robert Wood Johnson Medical School

Sherif B. Elsherif, MD
University of Florida, College of Medicine Jacksonville

Supported by Bracco Diagnostics, Inc.

Applied Radiology®

The Journal of Practical Medical Imaging and Management

Anderson Publishing, Ltd
180 Glenside Avenue,
Scotch Plains, NJ 07076
Tel: 908-301-1995
Fax: 908-301-1997
info@appliedradiology.com

PRESIDENT & CEO

Oliver Anderson

GROUP PUBLISHER

Kieran N. Anderson

EDITOR-IN-CHIEF

Erin Simon Schwartz, MD, FACR

EXECUTIVE EDITOR

Joseph F. Jalkiewicz

PRODUCTION

Barbara A. Shopiro

FOREWORD

We here at *Applied Radiology* are pleased to present this special supplement showcasing the winning papers of the 2023 Leaders on the Horizon Residents' program. Supported by an unrestricted educational grant from Bracco Diagnostics, Leaders on the Horizon challenges radiology residents to prepare and submit their best work for evaluation by an esteemed review panel of radiology professionals.

New for the 2023 program was the addition of a category for clinical review articles and expansion of participation to international residents. As a result, we received an overwhelming number of submissions from residents of seven countries on four continents. The top three winners in each category were honored during a special reception at RSNA 2023 by imaging industry professionals from around the globe. The winners of Leaders on the Horizon 2023 are:

Research Papers

1. Tej I. Mehta, MD, The Johns Hopkins Hospital
2. Monica M. Matsumoto, MD, University of Pennsylvania Medical Center
3. Peterson Chang, MD, West Visayas State University Medical Center

Clinical Review Papers

1. Helena Bentley, MD, MSc, University of British Columbia
2. William Raynor, MD, Rutgers RW Johnson Medical School
3. Sherif B. Elsherif, MD, University of Florida College of Medicine

The Leaders on the Horizon program offers residents the opportunity to work with their academic mentors and colleagues to further their passion for radiology. Equally, if not more importantly, the program affords participants the opportunity to be recognized for their commitment to excellence in medical imaging.

On behalf of *Applied Radiology* and Bracco Diagnostics, I would also like to thank the panel of reviewers who gave of their time to read and evaluate every submission and to provide their authors with invaluable feedback.

The panel members were: Lorna Browne, MD; Christopher Comstock, MD; Mark C. DeLano, MD,FACR; Paul Finn, MD; Alessandro Furlan, MD; Christine Glastonbury, MBBS; Ryan Lee, MD, MBA; Louis Mazzarelli, MD; John McGahan, MD; Mahmud Mossa-Basha, MD; Medhat Osman, MD, ScM, PhD, and Neil Rofsky, MD.

For information on participation requirements for the 2024 Leaders on the Horizon Residents' Program, including the deadline for submissions, please visit appliedradiology.com/leaders.

Sincerely,

Kieran N. Anderson

Publisher, Applied Radiology

LEADERS ON THE HORIZON 2023

Automated Machine Learning with Radiomics for Predicting Chronicity of Pulmonary Nodules in Patients with Nontuberculous Mycobacterial Lung Infection

Capt. Tej I. Mehta, MD; Caleb Heiberger, MD; Andrew Lancaster, BS; Muhammad Umair, MD; Dilek Oncel, MD; Harrison Bai, MD; Cheng Ting Lin, MD

Abstract

Objective and Hypothesis: This study aimed to create a machine learning model to differentiate acute and chronic pulmonary nodules using radiomics-based analysis. Distinguishing between acute and chronic nodules on computed tomography (CT) is essential for patient management but remains challenging due to absence of standardized imaging criteria. We hypothesized that radiomic features could predict nodule acuity.

Materials Methods: We retrospectively analyzed 110 adult subjects with non-tuberculous-mycobacterial respiratory-infection with at least two chest CT scans between 2005 and 2021. Acute nodules were those initially present and subsequently resolved, while chronic nodules persisted beyond 30 days on follow-up scans. A total of 260 acute and 249 chronic nodules were individually segmented by a radiologist and radiology resident, with the overlapping segments extracted for radiomics analysis; 112 radiomic features were extracted. A test set of 108 nodules was assessed blinded by four radiologists; their performances were compared to the AI model. Recursive-feature-elimination and permutation-importance were used to reduce overfitting, resulting in eight final features used for model development. An auto-machine learning package developed the final predictive model. Test performance metrics between the model and the individual radiologists were compared using McNemar's test and the area under the receiver operating curves (AUCs) for the model and the individual radiologists were compared using the DeLong test.

Results: The most accurate model was an ensemble model with sensitivity of 0.65, specificity of 0.92, positive predictive value of 0.88, negative predictive value of 0.75, and AUC of 0.88. The test performance metrics were significantly greater than two of the radiologists (P=0.011 and 0.020) and the AUC was significantly greater than all the radiologists (P value range:<0.0001–0.048).

Conclusions: This study demonstrates the feasibility of a machine learning model for predicting pulmonary nodule acuity using radiomics. The final model achieved an AUC of 0.88, significantly outperforming four radiologists.

Keywords: Nontuberculous mycobacterium, Machine learning, Radiomics, Pulmonary disease

Affiliations: Department of Radiology, The Johns Hopkins Hospital, Baltimore, Maryland (Drs Mehta, Heiberger, Umair, Oncel, Bai, Lin, Mr Lancaster); The United States Air Force Medical Corps, Falls Church, Virginia (Dr Mehta). Disclosures: The authors disclose no conflicts of interest and no relevant sources of financial support per ICMJE guidelines.
Conflict of interest and support statement: The authors declare no competing interests and received no funding or external support for this work.
Prior publication: No prior publication of this data has occurred.
Data sharing statement: No data are available. All data used in this study either were or were derived from DICOM images from The Johns Hopkins Hospital and are stored on internal databases. The original data are not publicly available. The Python code used to derive the radiomics data and generate the automated machine learning algorithm are provided as a supplement to this text.

Introduction

Nontuberculous mycobacterium (NTM) are pervasive organisms increasingly implicated in global respiratory morbidity and mortality. Evaluation of pulmonary changes related to NTM-induced lung disease (NTM-LD) via chest computed tomography (CT) scans is crucial for both diagnostic precision and therapeutic monitoring. In particular, the recognition of specific manifestations of NTM-LD is pivotal to clinical management. For example, patients with primarily nodular and bronchiectatic changes visible on CT imaging generally exhibit improved responses to antimycobacterial therapies, and patients with cavitary lesions or consolidations tend to respond more poorly to antimycobacterials.[1] Further supporting this notion, patients achieving full resolution of lung nodules on high-resolution CT (HRCT) scans after a six-month treatment course are more likely to experience successful therapeutic outcomes, and patients with persistent nodules are more likely to experience treatment failure or relapse.[2]

While the tracking and evaluation of radiographic alterations are crucial for understanding NTM-induced lung disorders (NTM-LD), the nuanced assessment of evolving pulmonary nodule features can be laborious and subject to inter-observer variability. Various classification methods and radiologic features of disease for NTM-LD nodules have been suggested, particularly for distinguishing NTM-LD from *Mycobacterium tuberculosis* (TB) infection, although none have achieved universal acceptance.[3,4]

Artificial intelligence (AI) applications in medical imaging are increasingly becoming an integral part of clinical practice, revolutionizing the healthcare landscape in the process. These AI solutions often equal or outperform traditional computer-aided diagnostic methods. Specifically, deep convolutional neural networks (DCNNs) have demonstrated efficacy in classifying patients with active TB versus healthy individuals through chest X-rays and distinguishing between NTM-LD and TB-related pulmonary conditions using chest CT scans.[5] Radiomics is another advanced imaging technique that can be particularly useful when dealing with smaller datasets and can describe and quantify human-recognizable features of imaging data, such as shape and pixel intensity features. Radiomics data may then be used for predictive or classification tasks.

Unlike DCNNs that often require large training datasets, radiomics can function efficiently on smaller data sets. The feature-based approach of radiomics also makes it more interpretable, allowing clinicians to trace back the outcomes to specific, understandable imaging features. This interpretability can be crucial for gaining clinical trust and for medical decision-making, especially in complex cases where the pathophysiological relevance of extracted features may be better understood. Therefore, radiomics offers an approach that may be more suited to certain diagnostic challenges.

This study hypothesizes that a radiomics-based model has the potential to reliably forecast the activity status of CT-identified NTM-LD nodules over a minimum timeframe of 30 days, with non-inferiority to the diagnostic accuracy of radiologists.

Materials and Methods

This retrospective study received approval from the Institutional Review Board (IRB), with a waiver for informed consent owing to its retrospective nature and minimal risk to patients.

Data Sets

Patients were recruited from the Johns Hopkins Center for Nontuberculous Mycobacteria and Bronchiectasis and were diagnosed with NTM-LD between 2005 and 2021, in accordance with standard clinical guidelines.

Chest CT scans available on our institutional picture archiving and communication system (PACS) were reviewed. Exclusion criteria consisted of patients with either one or no available CT scans, insufficient scan quality, or lack of suitable nodules for annotation. Both contrast-enhanced and non-contrast CT scans, including those from external institutions uploaded to our PACS, were considered.

Imaging Evaluation

A radiologist specializing in thoracic imaging with 9 years of experience, blinded to clinical information, assessed the axial CT images. Images were evaluated using lung window settings (window width: 1400 HU; window level: -500 HU) to identify and categorize non-fully-calcified pulmonary nodules. Acute and chronic nodules were characterized based on their stability or resolution in subsequent scans. Acute nodules were defined as those present on the initial scan but which were no longer apparent within 30 days of follow-up. Chronic nodules were defined as those present on the initial scan that persisted beyond 30 days.

We selected a subset of the data consisting of 57 acute pulmonary nodules and 51 chronic pulmonary nodules, which a group of four radiologists (Readers 1-4) labeled in a blinded fashion. These same nodules were used to create the testing data set (108 nodules) and the remaining nodules were used to create the training data set (401 nodules), with no patient overlap between the two.

Acute Nodule

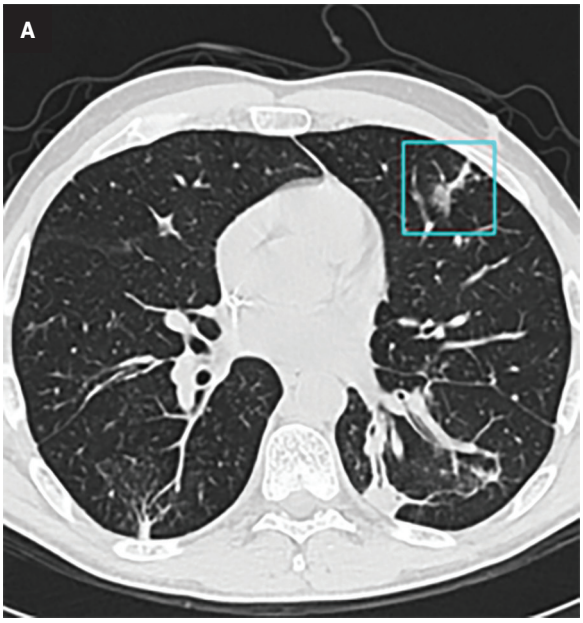

Predicted Label = Acute Nodule
Predicted Probablitiy Acute = 78.5%
Predicted Probability Chronic = 21.5%

Acute Nodule

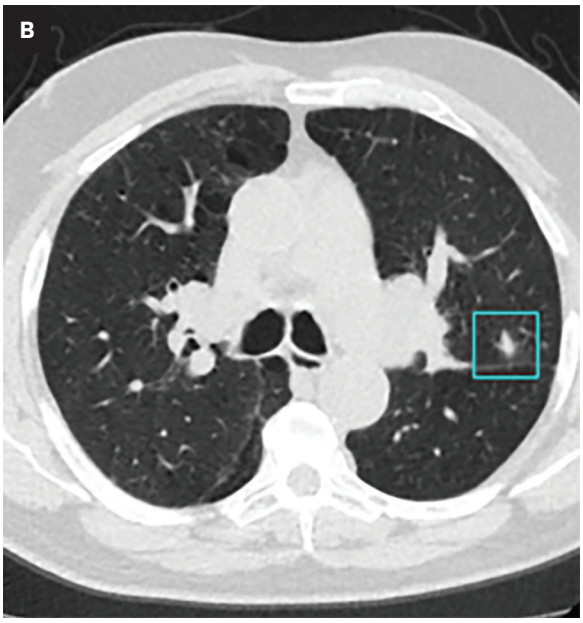

Predicted Label = Chronic Nodule
Predicted Probablitiy Acute = 35.3%
Predicted Probability Chronic = 64.7%

Chronic Nodule

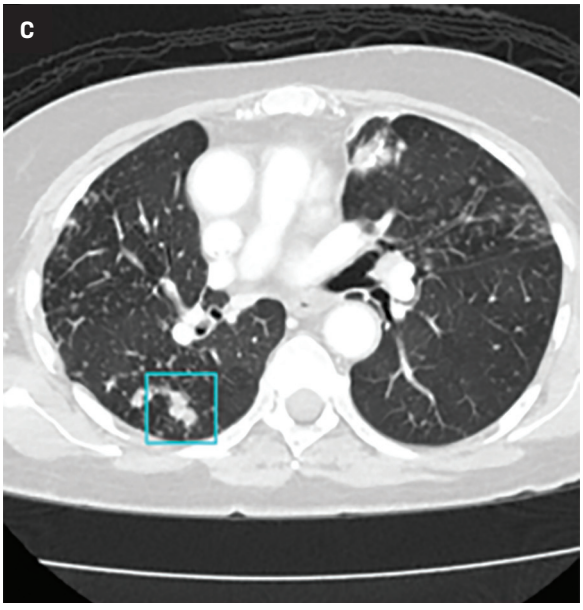

Predicted Label = Chronic Nodule
Predicted Probablitiy Acute = 15.1%
Predicted Probability Chronic = 84.9%

Chronic Nodule

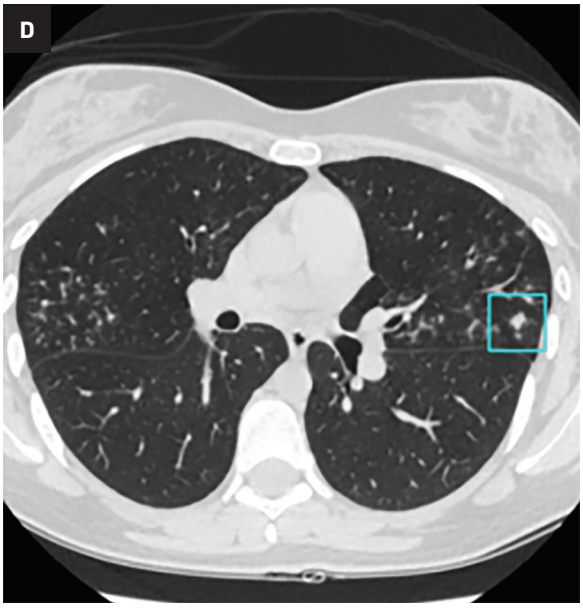

Predicted Label = Acute Nodule
Predicted Probablitiy Acute = 52.1%
Predicted Probability Chronic = 47.9%

Figure 1. Examples of correctly and incorrectly labeled acute and chronic nodules. (A) represents a nodule that the model correctly predicted to be acute with a predicted probability of 78.5%. (B) represents an acute nodule the model incorrectly predicted as chronic with a predicted probability of 64.7%. (C) represents a nodule the model correctly predicted as chronic with a predicted probability of 84.9%. (D) represents a chronic nodule the model incorrectly predicted as acute with a predicted probability of 52.1%.

Table 1. Performance metrics of the AI model and individual radiologists (readers 1-4) on the test data and p-values of the McNemar and DeLong tests comparing contingency table and AUC data respectively.

READER	ACCURACY	SENSITIVITY	SPECIFICITY	PPV	NPV	P-VALUE (MCNEMAR)	AUC	P-VALUE (DELONG)
AI Model	0.79	0.65	0.92	0.88	0.75	-	0.87	-
Reader 1	0.60	0.67	0.53	0.61	0.59	0.011	0.60	<0.0001
Reader 2	0.73	0.63	0.84	0.82	0.67	0.414	0.74	0.048
Reader 3	0.69	0.82	0.53	0.66	0.73	0.131	0.68	0.007
Reader 4	0.64	0.61	0.67	0.67	0.61	0.020	0.64	0.007

PPV – Positive Predictive Value; NPV – Negative Predictive Value; AUC – Area Under the Receiver Operating Curve

Segmentation, Radiomics, and Automated Machine Learning

Manual segmentation of all identified nodules was performed by a radiologist with 2 years of post-graduate experience and a third-year radiology resident, using 3D Slicer—an open-source software. The Dice Similarity Coefficient (DSC) was used to quantify the spatial overlap between the individual segmentations, and the overlapping areas were used for radiomic feature extraction.

Radiomic features were extracted and normalized using Pyradiomics (version 3.1.0).[6] One-hundred-twelve radiomic features (comprising all features available in the base Pyradiomics library) were extracted. Dimensionality reduction techniques were employed to select a subset of optimized features for modeling; specifically, recursive feature elimination was employed with a Random Forest algorithm to identify 30 key radiomic features, which generated an initial model. Feature importances from these 30 were subsequently analyzed, and features that detracted from model performance were excluded. The model was subsequently recreated on the features with optimal performance.

The selected radiomic features were then analyzed using the Autogluon auto-machine learning package (version 0.8.2) to develop predictive models.[7] During initial training, Autogluon constructs an ensemble of various models optimized for the chosen evaluation metric. From this ensemble, we extracted the highest-performing model based on the area under the receiver operating curve (AUC) performance. The evaluation metric was set to the AUC. The hyperparameters were configured to include bagging with 10 folds, 6 bagging sets, and 3 stacking levels. Training was limited to 120 minutes. Training was conducted on a GPU for computational efficiency. Additional hyperparameters were automatically optimized by Autogluon. Autogluon natively selects validation datasets from the training set.

Statistical Analysis

Model performance was assessed by accuracy (AC), sensitivity (SE), specificity (SP), positive predictive value (PPV), negative predictive value (NPV) and AUC on the testing dataset. The differences between the model's SE and SP were compared to the results from the testing data of each radiologist individually using McNemar's test and the differences between the model's and radiologists' AUCs were compared using the DeLong test, both with an alpha of 0.05. The contribution of individual features to the model was first assessed via feature ranking and subcategorization from recursive feature elimination. Individual feature importance was assessed via permutation shuffling with 5 shuffle sets. Statistical significance of feature importance was assessed via a t-test with the null hypothesis: importance = 0, vs the (one-sided) alternative: importance > 0 with an alpha of 0.01. Model confidence scores for individual label examples were derived from the predicted probabilities of the model.

Results

Nodule Segmentation and Model Configuration

A total of 509 pulmonary nodules—comprising 260 acute and 249 chronic nodules—were segmented. Interobserver agreement between the two radiologists responsible for the segmentation yielded an average DSC of 0.89, with a standard deviation of 0.07. The final machine learning architecture employed was a Neural Net Fast AI model; bagging techniques were utilized to augment the model's generalization capabilities.

Diagnostic Performance

Diagnostic metrics for the AI model and individual radiologists are summarized in Table 1. Visual examples of both accurately and inaccurately labeled nodules, accompanied by model-derived confidence scores as predicted probabilities, are presented in Figure 1.

McNemar's test identified significant differences in the classification performances between the AI model and two of the radiologists (Readers 1 and 4, P=0.011 and 0.020 respectively). Specifically, the SEs of the AI model and the two readers were similar (Se_{AI}=0.65, $SE_{Reader\ 1}$=0.67, $SE_{Reader\ 4}$=0.61); however, the

Figure 2. Receiver operating curves for the four radiologists (A) and the AI model (B). The area under the curve (AUC) for each receiver operating curve is displayed in the bottom right corner.

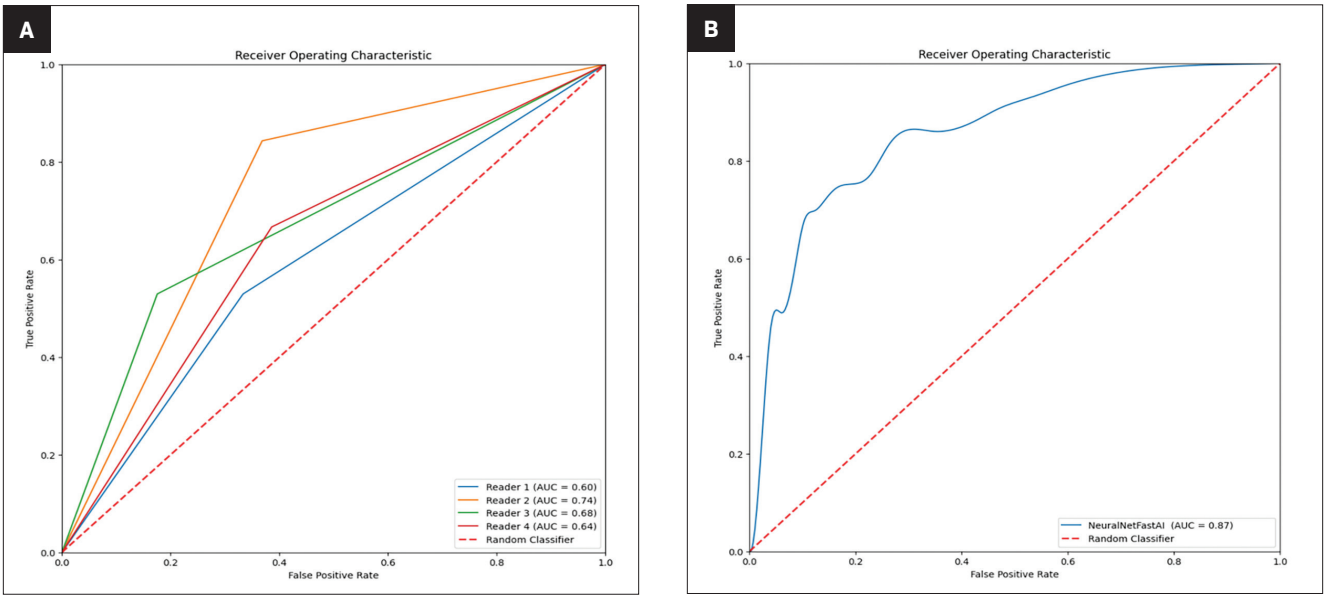

SP of the AI model was approximately 50% greater than the two radiologists (SP_{AI}=0.92, $SP_{Reader\ 1}$=0.53, $SP_{Reader\ 4}$=0.67, Table 1). Additionally, the AI model's AUC outperformed all of the radiologists (AUC_{AI}=0.87, $AUC_{Reader\ 1}$=0.60, $AUC_{Reader\ 2}$=0.74, $AUC_{Reader\ 3}$=0.68, $AUC_{Reader\ 4}$=0.64, P-value range:<0.0001–0.048, Table 1, Figure 2). The model had overall high performance in the classification of chronic nodules with PPV of 0.88 and moderate performance in the classification of acute nodules with NPV of 0.75. The radiologists achieved a wide range of PPVs (0.61-0.82) and NPVs (0.61-0.73).

Feature Importance and Contributions

Feature importance metrics are delineated in Table 2, and corresponding feature rankings are visually represented in Figure 3; eight features were found to significantly contribute to the model. Subcategories of features and their respective counts in the final model are outlined in Table 3. The majority of the chosen features were first-order statistics (N=5). The categories of original images values, shape, and gray level run length matrix each contributed one significant feature as shown in Table 3. The feature with the greatest permutation importance was gray level run length matrix run entropy (Permutation Importance=0.223).

Discussion

This study investigated the efficacy of a radiomics-based machine-learning model to accurately determine the chronicity of pulmonary nodules in patients with NTM-LD. The model had a significantly greater AUC for the classification of acute vs. chronic pulmonary nodules than any of four individual radiologists. The model also had overall high performance in the classification of chronic nodules with PPV of 0.88 and moderate performance in the classification of acute nodules with NPV of 0.75. These findings underscore the potential of radiomics in predicting the future behavior of NTM-LD based on complex imaging patterns.

The variability in predicting nodule chronicity between human readers and the AI algorithm suggests an avenue for further investigation into human interpretive patterns. Specifically, the important features extracted from the radiomics analysis may provide insight into features that humans look for in determining nodule chronicity.

Radiomic features may be categorized into various groups depending on the nature of image transformation algorithms and other techniques to identify high-dimensional patterns. The Image Biomarker Standardisation Initiative has outlined a widely recognized set of radiomic features, which were used in this study.[8] The most salient features in this context were first-order features, which describe basic distributions of voxel intensities within a region of interest. In this case, first-order features such as the range of voxel intensities, minimum and maximum voxel values, etc. constituted the majority of important features to the model. Shape and original image values were also of importance. Human expert readers are able to discern shape-based, original, and first-order features.[9] Only one of the eight significant features was a high-dimensional

Table 2. Significant features from the final model categorized by radiomic feature category.

FEATURE	PERMUTATION IMPORTANCE	STANDARD DEVIATION	P VALUE	N	99%CI HIGH*	99%CI LOW*
First Order Statistics						
10th Percentile Pixel Value	0.059	0.015	<0.001	5	0.089	0.029
Mean Absolute Deviation Pixel Values	0.046	0.012	<0.001	5	0.070	0.022
Maximum Pixel Value	0.045	0.009	<0.001	5	0.064	0.025
Range Pixel Values	0.025	0.003	<0.001	5	0.030	0.020
Minimum Pixel Value	0.021	0.005	<0.001	5	0.031	0.010
Gray Level Run Length Matrix						
Run Entropy	0.223	0.027	<0.001	5	0.279	0.168
Original Image Values						
Image Mean Pixel Value	0.023	0.004	<0.001	5	0.031	0.014
Shape						
Elongation	0.016	0.005	0.001	5	0.027	0.005

*Upper and lower bound of the 99th percentile confidence interval

Figure 3. Significant model features ranked by permutation importance. Permutation importance values are listed along the right side of each bar.

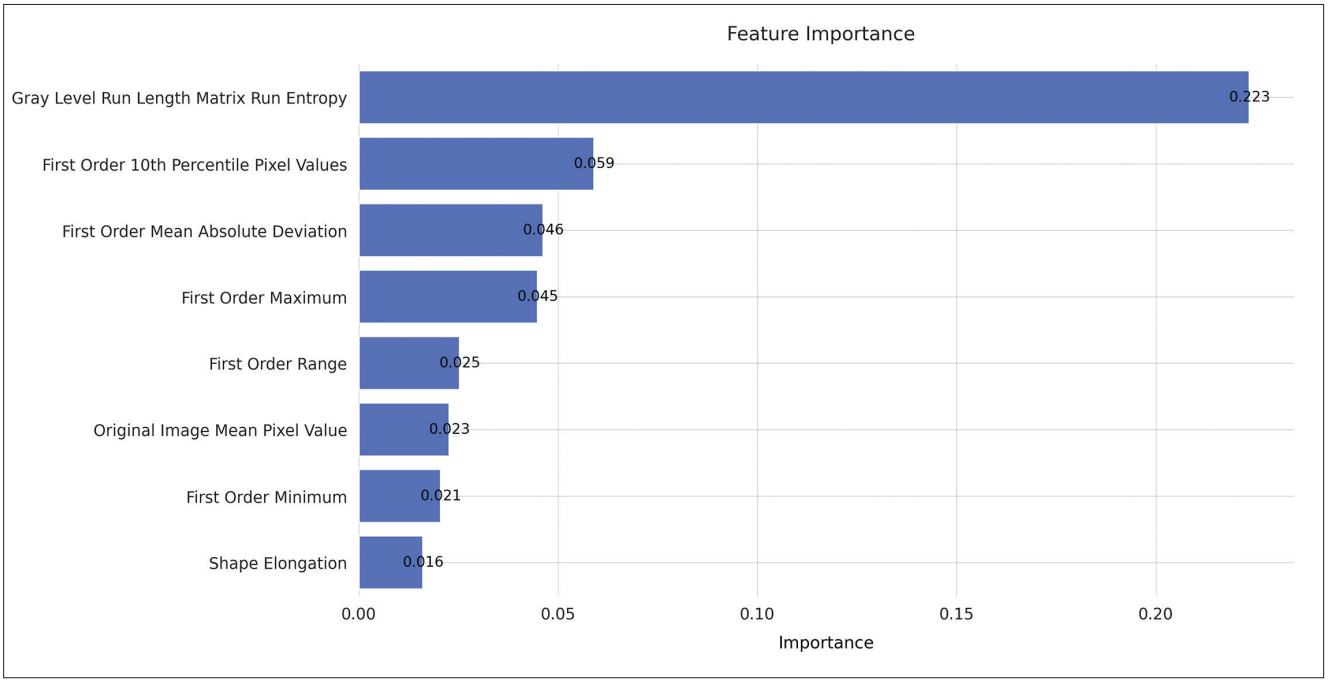

Table 3. Number of selected radiomic features per feature category from the final model.

FEATURE CATEGORY	NUMBER OF SELECTED FEATURES
Original Image	1
First Order Statistics	5
Shape	1
Gray Level Run Length Matrix	1

feature (gray level run length matrix run entropy), being a feature not generally perceptible to humans. However, this high-dimensional feature was the single most important feature to the model as determined by permutation importance. Taken together, the fact that the majority of significant features to the model were perceptible by humans but that the

most important feature was high-dimensional, indicates that there may be trends in the data imperceptible to humans, which may have implications on disease prognostication and possibly treatment.

Prior studies have employed deep convolutional neural networks (DCNNs) for NTM-LD prognostication,[10] but these are often limited by their "black-box" nature. Radiomics-based models, in contrast, provide a degree of interpretability by leveraging explicit radiomic features. For example, DCNNs have successfully been applied to predict outcomes such as mortality and differentiating between nontuberculous mycobacteria and *Mycobacterium tuberculosis*.[11] Similarly, radiomic-based analyses have been successfully applied to the prediction of NTM versus *M. tuberculosis*, with AUCs greater than 0.84, but have been able to identify specific features (both human interpretable and non-interpretable) to explain these predictions.[12] These results from the literature highlight the ongoing clinical applications of machine learning in the management of NTM-LD and related disorders and reiterate the point that high-dimensional features predictive of relevant pathologies exist which may be imperceptible to humans.

Our study has several limitations worth noting. First, this study, as with most radiomics-based approaches, required semi-automated image segmentation for data acquisition. Semi-automated segmentation has inherent subjectivity, which can affect accuracy, though we partially compensated for this by having two readers segment the same nodules and extracted the overlapping regions for radiomics analysis. Additionally, segmentation is a labor-intensive process, which can lengthen the time required to create a useable data set in comparison to DCNN techniques, wherein a single user can process orders of magnitude more data in the same amount of time, assuming these data are available. This data set primarily includes patients who sought care at a single tertiary care center in the United States. This may limit generalizability and, more specifically, may reduce the stability of the significant features to the model. A different patient population or scan technique may identify different significant features than the ones we identified. The representation of each nodule in our dataset is limited to a single axial CT slice rather than a 3D dataset, restricting our ability to fully capture the nodule's morphology and texture.

Our analysis is further limited to patients with follow-up CT scans. Patients with follow-up scans are generally either those with unresolved/worsening symptoms and/or those with the means to follow up with their exams. Lastly, we did not have pathologic confirmation for all of the detected nodules, adhering to the standard of care for NTM-LD surveillance, which generally reserves biopsy or surgery for specific refractory lesions or suspected malignancies.

Multiple future directions from this research may be considered. In a broad scope, one may envision a real-time probability indicator tool integrated into PACS systems for the radiologist and clinician's use. A nodule could be segmented and the future behavior of the nodule predicted with probability scores provided for clinical reference. To reach such a point, a larger, ideally multi-institutional, dataset would be required, and the final layers of the ensemble model could be retrained on data native to specific institutions to enhance per-institution model reliability. Additionally, integration of clinical and demographic information into the model may be of use. An approach such as this, integrating radiologic and clinical data in a systematic fashion, could help improve clinical decision making in NTM-LD.

In conclusion, our radiomics-based model shows promising utility for differentiating between acute and chronic pulmonary nodules in NTM-LD patients. Its diagnostic performance was comparable to that of experienced radiologists, suggesting its value as a diagnostic adjunct. Such tools could ultimately improve clinical decision-making and patient outcomes in the management of NTM-LD.

References

1) Haworth CS, Banks J, Capstick T, et al. British Thoracic Society guidelines for the management of non-tuberculous mycobacterial pulmonary disease (NTM-PD). *Thorax*. 2017;72(Suppl 2):ii1-ii64.

2) Lam PK, Griffith DE, Aksamit TR, et al. Factors related to response to intermittent treatment of Mycobacterium avium complex lung disease. *Am J Rresp Crit Care Med.* 2006;173(11):1283-1289.

3) Wang Y, Lin A, Lai Y, Chao T, Liu J, Ko S. The high value of high-resolution computed tomography in predicting the activity of pulmonary tuberculosis. *Int J Tuberc and Lung Dis.* 2003;7(6):563-568.

4) Wang Y, Shang X, Wang L, et al. Clinical characteristics and chest computed tomography findings related to the infectivity of pulmonary tuberculosis. *BMC Infect Dis.* 2021;21(1):1-7.

5) Liu C-J, Tsai CC, Kuo L-C, et al. A deep learning model using chest X-ray for identifying TB and NTM-LD patients: a cross-sectional study. *Insights into Imaging*. 2023;14(1):1-12.

6) Van Griethuysen JJ, Fedorov A, Parmar C, et al. Computational radiomics system to decode the radiographic phenotype. *Cancer Res.* 2017;77(21):e104-e107.

7) Erickson N, Mueller J, Shirkov A, et al. Autogluon-tabular: Robust and accurate automl for structured data. *arXiv preprint arXiv:200306505*. 2020;

8) Zwanenburg A, Leger S, Vallières M, Löck S. Image biomarker standardisation initiative-feature definitions. *arXiv preprint arXiv:161207003*. 2016;10

9) Gillies RJ, Kinahan PE, Hricak H. Radiomics: images are more than pictures, they are data. *Radiology*. 2016;278(2):563-577.

10) Andrew C. Lancaster B, Mitchell E. Cardin B, Jan A. Nguyen M, et al. Utilizing deep learning and computed tomography to determine pulmonary nodule activity in nontuberculous mycobacterial lung disease patients. *J Thorac Imag.* 2023;(Article in Press)

11) Xing Z, Ding W, Zhang S, et al. Machine learning-based differentiation of nontuberculous mycobacteria lung disease and pulmonary tuberculosis using CT images. *BioMed Res Internat.* 2020;2020

12) Yan Q, Wang W, Zhao W, et al. Differentiating nontuberculous mycobacterium pulmonary disease from pulmonary tuberculosis through the analysis of the cavity features in CT images using radiomics. *BMC Pulm Med*. 2022;22:1-12.

Understanding Patient Barriers to Utilization of Low-dose CT Lung Cancer Screening in a High-risk Population

Monica M. Matsumoto, MD; Cherie P. Erkmen, MD; Farouk Dako, MD, MPH

Abstract

Objective and Hypothesis: The purpose of this study was to assess factors that may affect low-dose CT (LDCT) utilization for lung cancer screening in a diverse population. The authors hypothesized that a lack of medical provider support may contribute to underutilization of LDCT for lung cancer screening.

Methods and Materials: A 22-question survey tool was developed and distributed to patients in the radiology department waiting room of a large, urban academic institution over a four-week period. The questionnaire assessed demographics, smoking history, knowledge about LDCT, and potential barriers to getting screened. Data are reported and frequencies.

Results: A total of 124 patients responded to the questionnaire. 50% were current or former smokers. 94% of respondents saw their primary care provider within the past year, although 89% said they had not heard about LDCT from their doctors. 90% knew that that smoking is the most common cause of lung cancer, although only 64% knew that lung cancer can be treated successfully at least "sometimes." 85% reported to be at least somewhat concerned that they or someone they know could die of lung cancer, and 86% were willing to visit their provider to learn more about lung cancer screening. Cost and conflict with work schedules were the most frequently reported reasons for nonadherence to medical appointments.

Conclusions: These data identified an information and communication gap related to lung cancer screening with LDCT, especially in a high-risk population. These results support the need to better understand factors contributing to this gap and to reduce barriers to communication and access.

Key Words: lung cancer; cancer screening; low-dose CT; health disparities; patient centered care

Introduction

Lung cancer is the second-most common cancer and the leading cause of cancer-related deaths in the United States.[1] Cigarette smoking is the number one risk factor for lung cancer, linked to about 80-90% of lung cancers in the United States.[1] Like most cancers, the stage of diagnosis strongly influences length of survival, with a five-year relative survival of 60% for localized disease, 30% for regional disease, and 6% for metastatic disease.[1] Over 50% of cases continue to be diagnosed at the metastatic stage.[2] Although advances in healthcare and disease prevention have led to improved lung cancer outcomes, racial and socioeconomic disparities persist.[1,3,4] Black Americans who smoke have a higher incidence of lung cancer, advanced disease on diagnosis, and mortality even when their cancer is diagnosed at the same stage as White individuals.[5,6]

Affiliations: Department of Radiology, Penn Medicine, Philadelphia PA (Drs Matsumoto and Dako). Department of Thoracic Medicine and Surgery, Temple University, Philadelphia, PA (Dr Erkmen). The authors declare no conflicts of interest or sources of financial support. Prior publication/presentation: Parts of the data have been presented as conference abstracts.
Data availability statement: All data relevant to the study are provided in the article or supplement.

Low-dose CT (LDCT) has become the preferred method of lung cancer screening, although adoption remains inconsistent, with several disparities in the community setting.[6] The landmark National Lung Screening Trial (NLST) demonstrated a 20% reduction in mortality among high-risk patients when utilizing LDCT instead of chest X-rays for screening, which has been attributed to disease detection at an earlier, more localized stage.[3]

The U.S. Preventive Services Task Force (USPSTF) updated its recommendations in 2021, which increased the number of people eligible for LDCT screening to include those 50-80 years old with a 20 pack-year history and who currently smoke or have quit within the past 15 years.[7,8] The need to screen high-risk individuals has also been recognized by numerous medical societies, and LDCT lung cancer screening is covered by Medicare, although variability exists for Medicaid coverage across states.[8-12]

Unfortunately, screening prevalence has been lagging and heterogeneous, with recent studies showing that only 5-20% of eligible individuals receive LDCT screening, with ongoing concerns about inequities across racial and ethnic groups.[4,13-18]

Furthermore, limited data exist on the impact of lung cancer screening in racial and ethnic minority populations despite their higher disease burden.[6,11,19] There is also concern that the NLST results may not be generalizable to all populations, as 91% of the participants were White, and efforts to introduce racial and ethnic diversity into the NLST have had limited success .[18,20-22]

Based on these unmet needs and health disparities, more data on community perceptions and barriers to LDCT screening are needed, especially among diverse populations. Identification of barriers and system failures can help guide the development of interventions. We hypothesized that a lack of medical provider support plays a role in underutilization of LDCT for lung cancer screening. Thus, the purpose of this study was to assess for factors that may affect LDCT utilization for lung cancer screening in an urban population that is already connected with a healthcare system.

Methods and Materials

The authors developed a questionnaire based on background research on disparities in lung cancer screening. Questions were designed to obtain data and elicit potential barriers to lung cancer screening with LDCT. The survey (available online at appliedradiology.com) comprised 22 questions:

- 5 on patient demographics;
- 2 on access and utilization of healthcare;
- 3 on smoking history;
- 1 on concern about lung cancer;
- 2 on knowledge about lung cancer;
- 1 on willingness to learn more about lung cancer screening;
- 1 on whether LDCT had been mentioned by a healthcare provider;
- 6 on awareness of and knowledge of LDCT lung cancer screening; and
- 1 on reasons for non-adhering to appointments.

Question formats included rating scale, dichotomous, and multiple-choice. Institutional review board approval was obtained prior to study initiation, and all participants consented to participate.

This study focused on barriers to obtaining lung cancer screening in patients who already had access to healthcare. Thus, participants were recruited from the waiting room of a radiology department in a large, urban academic institution over a four-week period. A designated research assistant distributed questionnaires to patients after they registered for their radiology diagnostic imaging or procedure. Participants were given the option to either return the questionnaire upon completion prior to leaving the registration area or to complete the questionnaire with the research assistant. A total of 124 questionnaires were collected.

Data are summarized as frequencies. The knowledge score about the lung cancer screening process was calculated on a scale of 0 to 5 based on correct answers, with a higher score indicating higher knowledge. Tabulation and analysis were performed using Stata SE 14.2 (StataCorp, College Station, TX).

Results

Table 1 presents the demographic information of respondents. 52% identified as Black/African American, and 59% had Medicare or Medicaid for insurance. 98% of respondents reported having a primary care provider; 94% reported visiting their provider within the past year. 54% of respondents were current or former smokers, and 77% had friends and/or family members who were heavy/long-time smokers.

Table 2 presents data on perspectives and knowledge about lung cancer and screening. 91% of respondents agreed that smoking is the most common cause of lung cancer, although only 64% thought that lung cancer can be treated successfully at least “sometimes.” 85% of respondents reported being at least somewhat concerned that they or someone they know can die of lung cancer. 89% of respondents

Table 1. Demographic information of survey respondents.

CATEGORY	SUBGROUP	N (%)
Age (y)	Mean (range)	50 (18-81)
	Median	52
Sex	Female	81 (65)
	Male	43 (35)
Race	Black or African American	65 (52)
	White	33 (27)
	Hispanic or Latino	25 (20)
	Asian	1 (1)
Highest level of education	No high school diploma	14 (11)
	High school diploma/some college	80 (65)
	College graduate	30 (24)
Health insurance	Uninsured	3 (2)
	Medicare or Medicaid	73 (59)
	Private insurance	48 (39)
Has a primary care provider	Yes	122 (98)
	No	2 (2)
Smoking status	Never smoker	57 (46)
	Current or previous smoker	67 (54)
Has close family/friend who is a heavy or long-time smoker	Yes	96 (77)
	No	28 (23)

Table 2. Responses to questions and knowledge about lung cancer and screening.

CATEGORY	SUBGROUP	N (%)
Believe that smoking is the most common cause of lung cancer	Yes	113 (91)
	No	11 (9)
Believe that lung cancer can be successfully treated	At least sometimes	79 (64)
	Almost never/never	45 (36)
Is worried that they or someone they know can die of lung cancer	Yes	105 (85)
	No	19 (15)
Has heard about LDCT from their doctor	Yes	14 (11)
	No	110 (89)
Is willing to go a doctor's appointment to learn more about lung cancer screening	Yes	107 (86)
	No	17 (14)
Knowledge score about lung cancer screening	Mean (Range)	2.2 (0-5)
	Median	2

Figure 1. Breakdown of reasons that respondents thought contributed to inability to attend scheduled medical appointments (>1 response possible, N = 255).

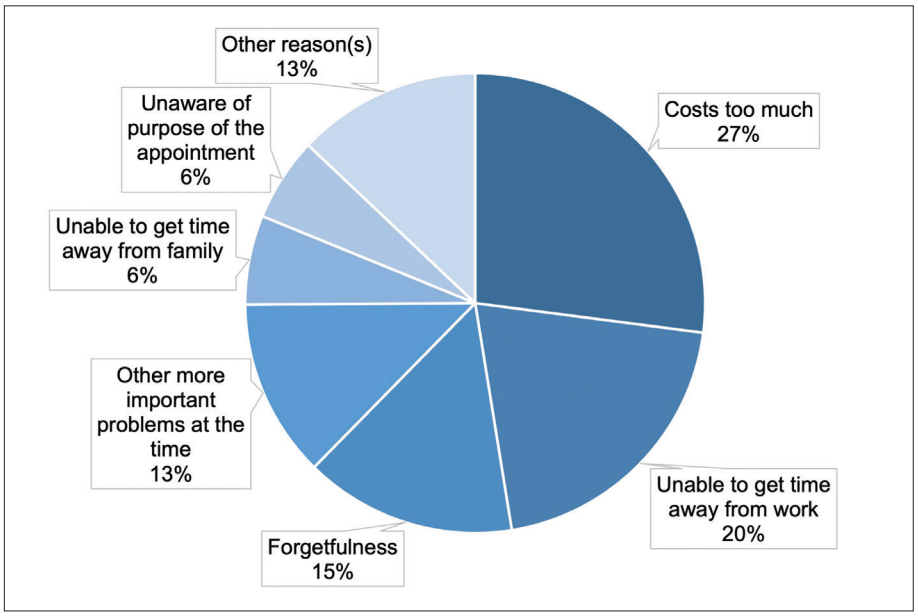

said they had not heard about LDCT lung cancer screening from their doctors, although 86% reported a willingness to visit a doctor to learn more about screening. The mean score on items assessing knowledge about lung cancer screening was 2/6 (33%). Figure 1 presents the breakdown of reasons that respondents thought contributed to their inability to attend scheduled medical appointments. Overall, 56% and 43% of respondents cited cost and inability to get out of work, respectively, as the most likely reasons.

Discussion

Low-dose CT for lung cancer screening has been shown to be at least as efficacious and cost effective as screening programs for breast and colon cancer.[21] However, recruitment of racial and ethnic minority patients at high risk of developing lung cancer requires time, effort, and infrastructure support.[22,23] Among the range of hurdles to introducing lung cancer screening into a community of diverse backgrounds, the authors specifically aimed to evaluate barriers that could be alleviated by changes made among hospitals and healthcare providers. For example, previous studies have demonstrated that Black individuals often live in more racially segregated communities compared to their White counterparts, which is associated with a later stage of diagnosis and lower cancer-specific survival.[24]

Therefore, the study population comprised patients at an urban institution in a Black-predominant community with the assumption that these patients were more likely to have insurance and connection to the healthcare system; thus, it was projected these patients would have a greater ability to access medical care, including appropriate screening exams.

These data demonstrated that respondents were relatively well informed about the link between smoking and the risk of developing lung cancer and were concerned about the associated morbidities. However, most respondents lacked fundamental knowledge about lung cancer screening and treatment opportunities, as approximately one-third did not believe that lung cancer was treatable. Patients may thus be unaware of the opportunity and importance of screening if their physicians are not appropriately assessing for or recommending it.

Nevertheless, most respondents indicated a willingness to visit a provider for more information, highlighting the importance of the doctor-patient relationship. Understanding the barriers for this communication gap and interventions facilitating provider communication with patients about lung cancer screening could help support patient adherence to such screening, especially since primary care physicians may be less familiar with the USPSTF recommendations.[17,25-27] For example, the American Academy of Family Physicians has previously stated that evidence is insufficient to recommend for or against lung cancer screening with LDCT, and their recommendation to follow the USPSTF guidelines was not updated until March of 2021.[28]

The doctor-patient relationship has been shown to be an influential component of obtaining lung cancer and other disease-related screenings.[29] Provider-level support, such as through patient navigators and development of culturally competent, shared decision-making tools, can help support the doctor-patient relationship and reduce barriers to care.[5,11,27]

In addition to deficient communication, respondents endorsed socioeconomic reasons for lack of adherence to appointments, especially cost and inability to take time off from work, likely related to accessibility and transportation. These findings are concordant with findings from other studies, and such barriers are of particular importance in lung cancer as it disproportionately affects patients of lower socioeconomic

status who, for example, often have less access to healthcare services and may experience higher levels of distrust of their providers.[5,6] Innovative interventions are needed to mitigate these barriers to screening, especially in communities that are at higher risk of death from lung cancer. Such interventions could include mobile imaging campaigns, provision of transportation benefits, expansion of telehealth consultations, and collaboration with community leaders.[5,6,23]

Study Limitations

Limitations of this study include the voluntary nature of the survey, convenience sampling of patients in the radiology waiting room at a single institution, and limited generalizability beyond the specific urban setting. No baseline population data were gathered, so response rate was not assessed. Nevertheless, the respondent demographics suggest a diverse cohort based on self-identified racial and educational backgrounds, which aligns with the study goals to evaluate an at-risk population. Additionally, the study assessed patients who already had access to the medical system, so these data likely overestimate knowledge and access. Appropriate access to and communication about lung cancer screening is likely even lower in the community setting.

In conclusion, this study identified a need for education of patients and providers with respect to the efficacy of early detection and treatment of lung cancer, as well as about the details of lung cancer screening. Ultimately, the success of LDCT for lung cancer screening depends on adequate awareness and patient access to the healthcare system, as well as a trusting patient-doctor relationship. Further studies are needed to better elucidate the factors contributing to disparities in LDCT lung cancer screening, with inclusion of other racial and ethnic minorities. The efficacy of interventions such as culturally appropriate educational material on LDCT, utilization of patient navigators to liaise with patients and doctors, and provision of transportation benefits to enable patients to keep medical appointments for lung cancer screening should also be evaluated.

References

1) Siegel RL, Miller KD, Fuchs HE, Jemal A. Cancer statistics, 2022. *CA Cancer J Clin.* 2022;72(1):7-33.

2) Cancer stat facts: Lung and bronchus cancer. National Cancer Institute. Surveillance, Epidemiology, and End Results (SEER) Program Web site. https://seer.cancer.gov/statfacts/html/lungb.html. Published 2023. Accessed 1 Aug, 2023.

3) Reduced lung-cancer mortality with low-dose computed tomographic screening. *N Engl J Med.* 2011;365(5):395-409.

4) Pinsky PF, Lau YK, Doubeni CA. Potential disparities by sex and race or ethnicity in lung cancer screening eligibility rates. *CHEST.* 2021;160(1):341-350.

5) Coughlin SS, Matthews-Juarez P, Juarez PD, Melton CE, King M. Opportunities to address lung cancer disparities among African Americans. *Cancer Med.* 2014;3(6):1467-1476.

6) Maki KG, Talluri R, Toumazis I, Shete S, Volk RJ. Impact of U.S. Preventive Services Task Force lung cancer screening update on drivers of disparities in screening eligibility. *Cancer Med.* 2023;12(4):4647-4654.

7) Force UPST. Screening for lung cancer: US Preventive Services Task Force recommendation statement. *JAMA.* 2021;325(10):962-970.

8) Pinheiro LC, Groner L, Soroka O, et al. Analysis of eligibility for lung cancer screening by race after 2021 changes to US Preventive Services Task Force screening guidelines. *JAMA Netw Open.* 2022;5(9):e2229741-e2229741.

9) Screening for lung cancer with low dose computed tomography (LDCT). Centers for Medicare & Medicaid. https://www.cms.gov/medicare-coverage-database/view/ncacal-decision-memo.aspx?proposed=N&ncaid=304. Published 2022. Accessed 1 Aug, 2023.

10) Gupta N, Halpern EJ, Rao VM. Association between Medicaid expansion status and lung cancer screening exam growth: Findings from the ACR lung cancer registry. *Clin Imaging.* 2021;73:79-85.

11) Rivera MP, Katki HA, Tanner NT, et al. Addressing disparities in lung cancer screening eligibility and healthcare access. An official American Thoracic Society statement. *Am J Respir Crit Care Med.* 2020;202(7):e95-e112.

12) Liu Y, Colditz GA, Kozower BD, et al. Association of Medicaid expansion under the Patient Protection and Affordable Care Act with non-small cell lung cancer survival. *JAMA Oncol.* 2020;6(8):1289-1290.

13) Jemal A, Fedewa SA. Lung cancer screening with low-dose computed tomography in the United States—2010 to 2015. *JAMA Oncol.* 2017;3(9):1278-1281.

14) Fedewa SA, Kazerooni EA, Studts JL, et al. State variation in low-dose computed tomography scanning for lung cancer screening in the United States. *J Natl Cancer Inst.* 2020;113(8):1044-1052.

15) Narayan AK, Gupta Y, Little BP, Shepard JO, Flores EJ. Lung cancer screening eligibility and use with low-dose computed tomography: Results from the 2018 Behavioral Risk Factor Surveillance System cross-sectional survey. *Cancer.* 2021;127(5):748-756.

16) Narayan AK, Chowdhry DN, Fintelmann FJ, Little BP, Shepard J-AO, Flores EJ. Racial and ethnic disparities in lung cancer screening eligibility. *Radiology.* 2021;301(3):712-720.

17) Lopez-Olivo MA, Maki KG, Choi NJ, et al. Patient adherence to screening for lung cancer in the US: A systematic review and meta-analysis. *JAMA Netw Open.* 2020;3(11):e2025102-e2025102.

18) Aldrich MC, Mercaldo SF, Sandler KL, Blot WJ, Grogan EL, Blume JD. Evaluation of USPSTF lung cancer screening guidelines among African American adult smokers. *JAMA Oncol.* 2019;5(9):1318-1324.

19) Kunitomo Y, Bade B, Gunderson CG, et al. Racial differences in adherence to lung cancer screening follow-up: A systematic review and meta-analysis. *Chest.* 2022;161(1):266-275.

20) Tanner NT, Gebregziabher M, Halbert CH, Payne E, Egede LE, Silvestri GA. Racial differences in outcomes within the National Lung Screening Trial: Implications for widespread implementation. *Am J Respir Crit Care Med.* 2015;192(2):200-208.

21) Pasquinelli MM, Tammemägi MC, Kovitz KL, et al. Risk prediction model versus United States Preventive Services Task Force lung cancer screening eligibility criteria: Reducing race disparities. *J Thorac Oncol.* 2020;15(11):1738-1747.

22) Duda C, Mahon I, Chen MH, et al. Impact and costs of targeted recruitment of minorities to the National Lung Screening Trial. *Clin Trials.* 2011;8(2):214-223.

23) Barta JA, Shusted CS, Ruane B, et al. Racial differences in lung cancer screening beliefs and screening adherence. *Clin Lung Cancer.* 2021;22(6):570-578.

24) Annesi CA, Poulson MR, Mak KS, et al. The impact of residential racial segregation on non-small cell lung cancer treatment and outcomes. *Ann Thorac Surg.* 2022;113(4):1291-1298.

25) Lin Y, Liang L-J, Ding R, Prosper AE, Aberle DR, Hsu W. Factors associated with nonadherence to lung cancer screening across multiple screening time points. *JAMA Netw Open.* 2023;6(5):e2315250-e2315250.

26) Martinez MC, Stults CD, Li J. Provider and patient perspectives to improve lung cancer screening with low-dose computed tomography 5 years after Medicare coverage: A qualitative study. *BMC Prim Care.* 2022;23(1):332-332.

27) Lee SJC, Lee J, Zhu H, et al. Assessing barriers and facilitators to lung cancer screening: Initial findings from a patient navigation intervention. *Popul Health Manag.* 2023;26(3):177-184.

28) Lung cancer - Clinical preventive service recommendation. American Academy of Family Physicians. https://www.aafp.org/family-physician/patient-care/clinical-recommendations/all-clinical-recommendations/lung-cancer.html. Published 2021. Accessed 1 Aug, 2023.

29) Borondy Kitts AK. The patient perspective on lung cancer screening and health disparities. *J Amer Coll Radiol.* 2019;16(4):601-606.

A Comparative Study of Renal Parenchymal Resistive Index, Ultrasonographic Grading of Renal Parenchymal Echogenicity, Kidney Length, and Estimated Glomerular Filtration Rate Among Chronic Kidney Disease Patients Undergoing Whole Abdominal Ultrasound at West Visayas State University Medical Center

Peterson Chang, MD; Emmanuel Pelingon, RVT

Abstract

Chronic kidney disease (CKD) is one of the leading causes of mortality in the Philippines. In a country with a poorly structured healthcare system, it is important to maximize available resources in the management of patients with this disease.

Ultrasound is the imaging modality of choice for screening and detection of kidney disease. Both morphologic (kidney length, renal parenchymal echogenicity grading) and hemodynamic (resistivity index) sonographic parameters are valuable in the assessment and determination of disease progression.

This is a prospective cross-sectional study correlating the ultrasonographic parameters (morphologic and hemodynamic) to the computed estimated glomerular filtration rate (eGFR) of CKD patients. A total of 42 subjects categorized as belonging to CKD grades 3 through 5 based on eGFR participated.

The study showed a significant correlation between renal parenchymal echogenicity and eGFR. In conclusion, the grading of renal parenchymal echogenicity is a useful parameter compared to the resistivity index and renal length in determining the renal status of CKD patients.

Key terms: chronic kidney disease, resistivity index, eGFR

Introduction

An estimated 1.2 million people worldwide died of chronic kidney disease (CKD) based on the 2017 Global Burden of Chronic Kidney Disease Study.[1] The prevalence of CKD in Asian countries is reported to be among the highest in the world. As of 2016, it was one of the leading causes of death, according to *The American Journal of Kidney Disease*.[2] In the Philippines, kidney diseases, especially end-stage renal disease (ESRD), are the seventh leading cause of death among Filipinos, according to the National Kidney and Transplant Institute.[3] Chronic kidney disease poses a tremendous financial burden on patients in developing countries with poorly structured public healthcare systems, such as the Philippines.[2]

Adequate evaluation of renal diseases with readily available diagnostic tools is essential to decision making that could offer a more favorable outcome for the patient. Ultrasonography is becoming a first-line modality in suspected cases of renal disease

Affiliation: West Visayas State University Medical Center, Jaro, Iloilo City, Iloilo, Philippines (Dr. Chang); Ng Teng Fong General Hospital, Singapore (Mr. Pelingon).
Acknowledgement: The authors would like to thank the chairman of the Department of Radiology, and the head and staff of the ultrasound department, of the West Visayas State University Medical Center, for their assistance and permission to conduct this study.

and postintervention surveillance. Since ultrasonography is relatively affordable, does not require contrast media or expose patients to ionizing radiation, and is non-nephrotoxic, it has become the most useful tool in evaluating renal disease.[4,5]

Morphological changes in the renal parenchyma were indisputably found to correlate with renal disease thus, Doppler ultrasound has been incorporated in greyscale imaging and is used to calculate the resistive index (RI) flow parameter, which has been considered in numerous studies to be a promising tool in obtaining quantitative diagnostic and therapeutic insight into CKD.[6]

Research Question

The major question at the center of this study was: which sonographic parameter (resistivity index, renal parenchymal echogenicity grading, or kidney length) is most sensitive to and correlates well with declining eGFR levels in patients with chronic kidney disease undergoing whole abdominal ultrasound at West Visayas State University Medical Center (WVSUMC)?

Statement of the Problem

The estimated glomerular filtration rate is the most widely used indicator for renal disease. The "2002 National Kidney Foundation–Kidney Disease Outcomes Quality Initiative (NKF-KDOQI) Clinical Practice Guidelines for Chronic Kidney Disease: Evaluation, Classification, and Stratification," and "The Kidney Disease: Improving Global Outcomes (KDIGO) 2012 Clinical Practice Guideline for the Evaluation and Management of Chronic Kidney Disease (CKD)," both define CKD as a decrease in eGFR (<60 ml/min/1.73 mm^2). They also recommend the use of eGFR and creatinine in the initial assessment. However, the availability of eGFR reports may not be instantaneous in outpatient clinics. Some studies highlight common limitations that challenge the utility of eGFR in the diagnosis of CKD.[7]

Ultrasound has been used for decades to evaluate the degree of kidney disease using morphologic changes in the renal parenchyma. Recently, renal parenchymal resistive indices have been found to help assess CKD. A study by Heine et al in 2006 concluded that ultrasound intrarenal RI independently reflects local renal damage and systemic vascular disease.[8]

Kidney sonography at our institution does not involve resistive index determination despite the ease of acquisition of RI values. There appears to be an insufficient comparative study regarding which parameter—ultrasound grading of the renal parenchyma, parenchymal RI, or kidney length—best correlates with abnormal eGFR levels. Moreover, the correlation between the sonographic variables is not well-documented in our setting.

Although various studies have independently correlated each parameter to eGFR, how these variables compare with each other in evaluating CKD is not known. Thus, this study aimed to determine how well sonographic grading of renal parenchymal echogenicity, kidney size, and the resistive indices correlate with declining eGFR grades in these patients.

Significance of the Study

In clinical settings, no single diagnostic parameter is recommended for initial assessment of the patient's condition. The KDOQI and KDIGO Guidelines define CKD based on structural abnormalities detected in imaging and decreased eGFR. Hence, this study seeks to correlate the sensitivity of ultrasound's morphological and hemodynamic parameters to the eGFR. The acceptable correlation of the two will impact clinicians, sonographers, radiologists, and patients.

Imaging with qualitative and quantitative parameters for detecting CKD presence, severity, and progression will provide clinicians with better guidance in managing the disease and help determine treatment efficacy. In certain conditions where eGFR calculations are hampered by overestimations or underestimations owing to discrepancies in the biomarkers being analyzed, sonography offers an alternative parameter. The current scanning protocol can be modified to incorporate vascular studies for CKD assessment and serve as alternative parameters where renal parenchymal echogenicity is indiscernible. A comprehensive imaging report with qualitative and quantitative assessment can provide patients with a more conclusive diagnosis, reducing the need for additional, costly imaging procedures.

Objectives of the Study

This study aimed to compare morphologic parameters (sonographic grading of renal parenchymal echogenicity and kidney length) and the hemodynamic parameter (renal RI) and their correlation to the eGFR of CKD patients undergoing whole abdominal ultrasound at West Visayas State University Medical Center. More specifically, it was performed to:

- Identify which parameter is more sensitive to and correlates well with deranged eGFR levels (Grades 3 to 5); and,
- Determine the correlations between different sonographic parameters (RI, renal parenchymal echogenicity grading or kidney length) as eGFR grades decline.

Table 1. Grading of renal parenchymal echogenicity.

	PARENCHYMAL ECHOGENICITY (COMPARED TO SPLEEN PARENCHYMA)	CORTICO-MEDULLARY DIFFERENTIATION
GRADE 0	Less	Well-maintained
GRADE 1	Same	Maintained
GRADE 2	More	Decreased
GRADE 3	More	Poorly maintained

Figure 1. Representative sonograms of renal parenchymal echogenicities at different gradings. Grade 0 (A) shows well-maintained cortico-medullary differentiation with cortical echogenicity less than the adjacent spleen. Grade 1 (B) shows isoechoic cortex with that of the adjacent splenic parenchyma with maintained cortico-medullary differentiation. Grade 2 (C) shows decreased cortico-medullary differentiation with hyperechoic cortex compared to adjacent splenic parenchyma. Grade 4 (B) shows decreased renal length with markedly increased cortical echogenicity and lack of cortico-medullary differentiation.

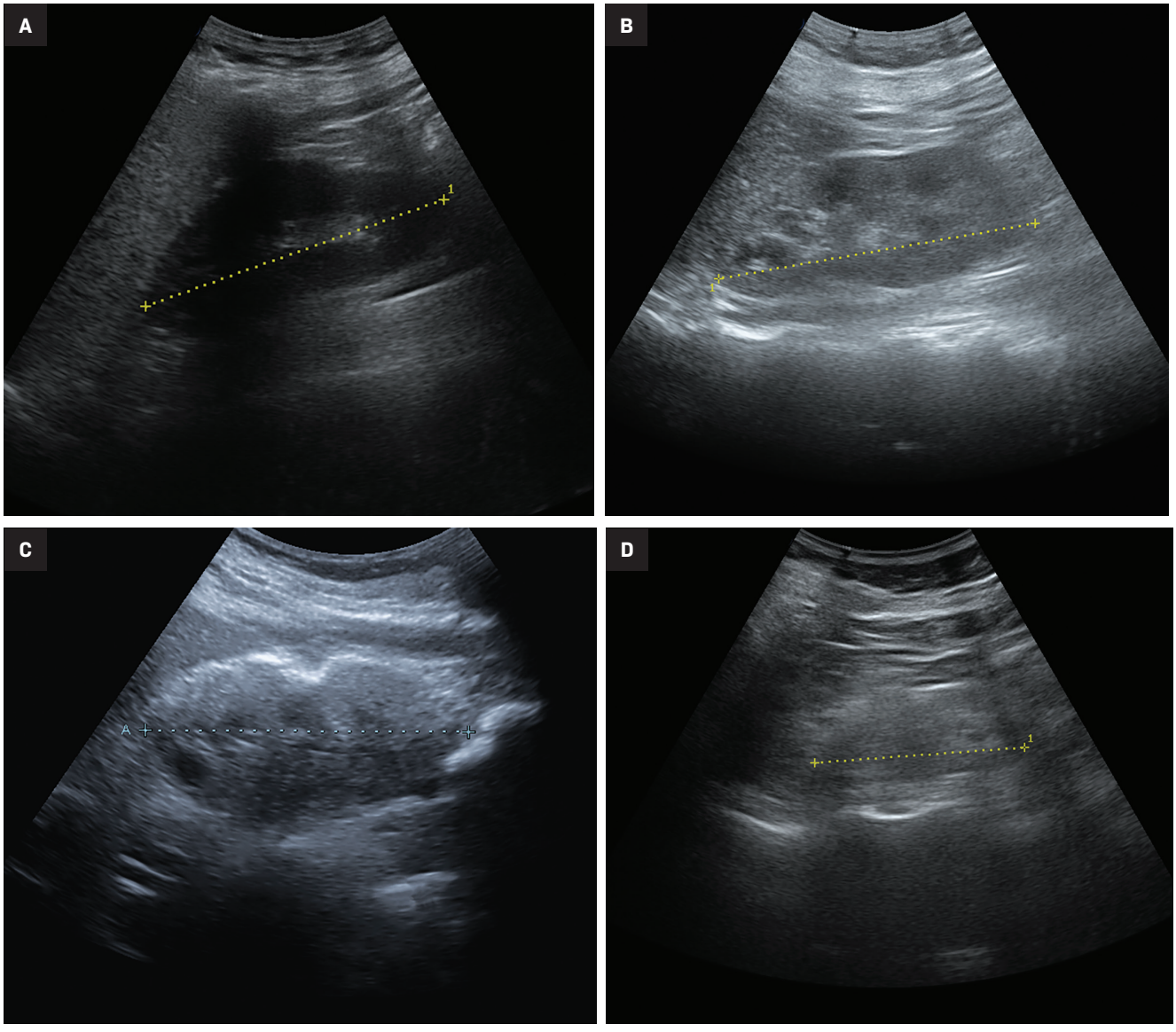

Review of Literature

A review of the literature was conducted to determine the subjects and conclusions of studies with respect to the utility of morphologic and hemodynamic parameters in ultrasound.

eGFR

According to the "KDIGO 2012 Clinical Practice Guideline for the Evaluation and Management of Chronic Kidney Disease," the kidney has many functions, including excretory, endocrine, and metabolic. The glomerular filtration rate (GFR) is one component of excretory function. However, it is widely accepted as the best index of overall kidney function because it is generally reduced following widespread structural damage, and most other kidney functions decline in parallel with GFR in CKD.[9]

For these reasons, the guidelines recommend eGFR in the assessment, management, and monitoring of disease progression of CKD patients. In a 2008 commentary appearing in the *Clinical Journal of American Society of Nephrology*, however, Richard J. Glassock and Christopher Winearls discouraged the use of eGFR alone in diagnosing and classifying CKD.[10]

Morphological Parameters

Unlike acute kidney injury, where healing is complete with total functional kidney recovery, sustained insults from chronic and progressive nephropathies progress to kidney fibrosis and destruction of the normal organ architecture.[11] Ultrasound scans that demonstrate small kidneys with reduced cortical thickness, increased echogenicity, scarring, or multiple cysts suggest a chronic process. [11]

In a 2015 study of 72 CKD patients with stages 1-4 disease, Lucisano et al concluded that the improved correlation of corrected parameters for body height with the GFR makes renal sonography a reliable tool for a more complete assessment of the disease.[12]

In 2017, Yaprak and colleagues published their findings on the role of kidney length, parenchymal thickness and echogenicity in assessing CKD. They utilized these parameters to interrogate each kidney of 120 patients with stages 1-5 CKD. An ultrasonographic CKD score was used, based on the mentioned parameters, which revealed that eGFR correlates with kidney length and parenchymal thickness.[13]

In a study by Shivashankara et al, renal parenchymal status was assessed effectively using a grading system that compared the echotexture of the renal parenchyma with that of the splenic parenchyma, as well as the degree of sonographic differentiation of the renal cortex to that of the medulla (Table 1).[5]

Ahmed et al in 2019 studied the correlation of the role of ultrasound with serum creatinine levels in the diagnosis of CKD. The researchers found that renal cortical echogenicity correlates best with serum creatinine over longitudinal kidney length, parenchymal thickness, and cortical thickness in patients with CKD.[14]

Hemodynamic Parameters

In their 2022 study, Radermacher et al hypothesized that in patients with CKD of any cause, the decline of renal function resulting from nonspecific renal scarring would correlate with a higher renal resistance index. Interstitial fibrosis and loss of capillaries and glomeruli are the hallmarks of renal scarring. Assessment of intrarenal vascular resistance helps determine the degree of renal parenchymal damage. Color Doppler ultrasonography was performed on 162 consecutive patients with renal disease. The researchers found that renal function declined over time in patients with RI >0.80. They concluded that a renal RI ≥0.80 reliably identifies patients at risk for progressive renal disease.[15]

A 2012 study published in *Biomed Central Nephrology* found an association between renal RI with histologic findings and renal outcome. The renal RI was measured prior to biopsy in 58 CKD patients. The study revealed that RI ≥ 0.65 were associated with severe interstitial fibrosis, arteriosclerosis, and declines in renal function.[16] However, the sample size was small, and CKDs arise primarily from glomerulonephritis.

In 2020, Sutikno et al compared the diagnostic value of renal RI and cortical echogenicity in 41 CKD patients. Resistive indices and degree of echogenicity were taken from both kidneys of subjects, all with a GFR ≤ 90 ml/min./1.73 m^2 at screening. They found renal RI to be superior to renal cortical echogenicity in terms of specificity for CKD.[4]

The literature clearly shows the significant correlation of morphologic and hemodynamic parameters of ultrasound in the diagnosis and management of CKD. The absence of studies comparing these parameters to the GFR challenges their sensitivity to CKD. It also raises the question of whether they can be reliable imaging tools in assessing CKD or in determining the potential for disease progression.

Methods

Study Design and Setting

This is a prospective observational (cross-sectional) study correlating ultrasonographic morphologic and hemodynamic parameters to the computed eGFR of CKD patients.

Table 2. GFR category based on MDRD formula.

GFR CATEGORY	EGFR (ML/MIN/M2)	TERMS
Grade 1	≥ 90	Normal or high
Grade 2	60-89	Mildly decreased
Grade 3a	45-59	Mildly to moderately decreased
Grade 3b	30-44	Moderately to severely decreased
Grade 4	15-29	Severely decreased
Grade 5	<15	Kidney failure

Table 3. Sociodemographics.

CHARACTERISTIC	AGE	SAMPLE (N)	PERCENTAGE (%)
Average age (56.10 ± 16.5246)			
Age groups			
	19-40	6	14.29
	41-60	18	42.86
	>60	18	42.86
Sex			
	Male	22	52.38
	Female	20	47.62
Marital status			
	Married	23	54.76
	Single	10	23.81
	Separated	-	-
	Widowed	9	21.43
Ethnicity			
	Asian	42	100
	Others	-	-

The data collection and processing were conducted at West Visayas State University Medical Center, a 300-bed tertiary hospital in Jaro, Iloilo City, Iloilo, Philippines.

Study Period, Patient Selection, Scope, and Limitations

Prospective reviews were conducted on the charts of admitted CKD patients scheduled to undergo abdominal ultrasound examination at the WVSU-MC between March and November 2022. Patients diagnosed with CKD were further evaluated according to inclusion/exclusion criteria, resulting in a sample size of 42 subjects. The following are the inclusion and exclusion criteria:

Inclusion criteria

- CKD patients with eGFR ≤59 mL/min/1.73 m^2 (computed using the MDRD formula) or eGFR Grades 3 to 5 (Table 2);
- Age ≥ 18 years

Exclusion criteria

- Undergoing renal replacement therapy (hemodialysis, peritoneal dialysis) or post-kidney transplant)
- Patients with major physical dismemberment; and
- Presence of nephrolithiasis, hydronephrosis, renal malignancies, or acute febrile illnesses.

Scope and Limitations of the Study

This study utilized a creatinine-based eGFR calculation in determining the severity of CKD, as it is a widely available and reliable assay recommended by the latest clinical practice guidelines. Although inulin clearance remains the gold standard for measuring GFR, the test is expensive and not readily available.

Study Population and Procedure

Forty-two patients who underwent whole abdominal ultrasound examinations at WVSUMC within the aforementioned timeframe were included. No randomization was done. The examinations were performed using either the Toshiba Ultrasound System Xario 200 (with serial number 99B1463412) or Sonoscape S50 (with serial number 0502505103).

Renal parenchymal echogenicity grading and kidney length measurements were obtained by the radiology resident-in-charge and double-checked by the radiology consultant on duty (Figure 1). Parenchymal echogenicity grading was based on comparative echogenicity for the spleen (Table 1), while a kidney length of <8 cm was considered decreased. Resistivity indices were obtained by a radiology resident experienced in vascular sonography, with >0.70 considered an abnormally increased RI.

Patient demographic and clinical data were uploaded to a secure database for patient confidentiality

Table 4. Morphologic and hemodynamic ultrasonographic features and eGFR category.

CHARACTERISTICS	SAMPLE (N)	PERCENTAGE (%)
Resistivity index (right)		
normal	16	38.10
abnormal	26	61.90
Resistivity index (left)		
normal	13	30.95
abnormal	29	69.05
Renal parenchymal echogenicity grade		
0	2	4.76
I	17	40.48
II	13	30.95
III	10	23.81
eGFR category		
3a	5	11.90
3b	8	19.05
4	8	19.05
5	21	50.00
eGFR	19.46 + 16.4908	
Mean kidney length (±SD) (cm)	9.19 + 1.3985	

Table 5a. Comparison of eGFR with RI-right.

EGFR GRADE	NO. OF PATIENTS	MEAN RI	SD	CHI-SQUARE	P-VALUE
3a	5	0.662	0.1096	3.667	0.2997
3b	8	0.755	0.0438		
4	8	0.794	0.1167		
5	21	0.768	0.1459		
Total	42	0.758	0.1250		

Table 5b. Comparison of eGFR with RI-left.

EGFR GRADE	NO. OF PATIENTS	MEAN RI	SD	CHI-SQUARE	P-VALUE
3a	5	0.696	0.0391	3.49	0.3220
3b	8	0.789	0.0848		
4	8	0.774	0.0816		
5	21	0.817	0.2277		
Total	42	0.789	0.1712		

and privacy. Each patient was assigned a code to maintain anonymity and data organization.

Resistive Index Determination

The patients were scanned using a curvilinear probe. Spectral Doppler images with clear waveform patterns were captured. The peak systolic velocity (PSV) and the end diastolic velocity (EDV) were measured. The RIs were automatically calculated by the machine presets using the equation (PSV-EDV)/PSV. The ntraparenchymal arteries in the upper, middle, and lower poles of both kidneys were sampled. The sample volume was set to a minimum with a narrow angle of insonation. The three RI measurements for each kidney were averaged. Only the highest average RI value from one sample was recorded. Reports were validated by a sonologist with adequate experience in vascular sonography.

Renal Length and Parenchymal Echogenicity

Kidney length was measured with a curvilinear probe in the coronal plane with the patient in the supine or lateral decubitus position. The maximum longitudinal section from both pole ends was recorded.

The renal parenchymal echotexture was compared to the splenic parenchymal echotexture and graded according to the criteria in Table 1 as in the study by Shivashankara et al. Representative sonograms at different renal parenchymal echogenic grades are also shown in Figure 1. All sonographic morphological parameters were conducted by resident radiology physicians and validated by experienced consultant radiologists.

eGFR Calculation

Serum creatinine (in mg/dl) level at patient admission, age, and sex were used for eGFR computation (in ml/min/1.73 m^2) using the

Table 6. Comparison of renal parenchymal echogenicity grade with eGFR

RPEG	NO. OF PATIENTS	MEAN EGFR (ML/MIN/M2)	SD	CHI-SQUARE	P-VALUE
0	2	33.90	19.7990	12.326	0.0063
I	17	28.76	17.3868		
II	13	10.47	9.9457		
III	10	12.47	12.0532		
Total	42	19.46	16.4908		

Table 7a. Comparison of eGFR with kidney length

EGFR GRADE	NO. OF PATIENTS	MEAN KIDNEY LENGTH (CM)	SD	CHI-SQUARE	P-VALUE
3a	5	9.34	1.0114	0.075	0.9947
3b	8	9.25	0.9024		
4	8	9.10	1.2694		
5	21	9.17	1.7161		
Total		9.19	1.3985		

Table 7b. Comparison of eGFR by kidney characteristic

	KIDNEY LENGTH (CM)				
EGFR GRADE	ABNORMAL	%	NORMAL	%	TOTAL
3a	1	20	4	80	5
3b	1	12.5	7	87.5	8
4	2	25	6	75	8
5	4	19.05	17	80.95	21
Total	8	19.05	34	80.95	42

Table 8. Correlation of eGFR with morphologic and hemodynamic parameters

PARAMETERS	SPEARMAN COEF.	P-VALUE
RI-right	-0.1934	0.2196
RI-left	-0.1640	0.2995
RPEG	-0.4967	0.0008
kidney length	0.1704	0.2806

Modified Diet in Renal Disease (MDRD) formula:

$$(175 \times (\text{serum creatinine}) - 1.154 \times (\text{Age}) - 0.203 \times (0.742 \text{ if female}) \times (1.212 \text{ if African American})$$

Chronic kidney disease, as defined by KDIGO, is the presence of abnormalities of kidney structure or function for >3 months and with health implications and graded according to serum creatinine-based eGFR computation (Table 2), with <60 ml/min/m^2 (Grades 3a to 5) as the threshold for CKD.

Data Processing and Analysis

Data processing and analysis were performed using the Stata MP Version 17. The mean and standard deviation were calculated for age, eGFR, and kidney length. Frequencies and percentages were used to determine other sociodemographic characteristics and morphological and hemodynamic parameters. – RIs and longitudinal kidney length were calculated for each eGFR grade. The eGFR was calculated for each grade of renal parenchymal echogenicity.

The Kruskal-Wallis H Test was performed to check for association between groups, and Spearman's rank correlation coefficient was used to determine the strength of association between variables. A p-value <0.05 was considered statistically significant.

Results

This study compared and identified the correlation between morphological parameters (sonographic grading of the renal parenchymal echogenicity and kidney length), hemodynamic parameters (renal RI), and eGFR of patients with CKD who underwent whole abdominal ultrasound.

A total of 42 subjects were accounted for in this study. All of

Figure 2. Scatterplot of eGFR (ml/min/1.72 m2) and RI of right kidney

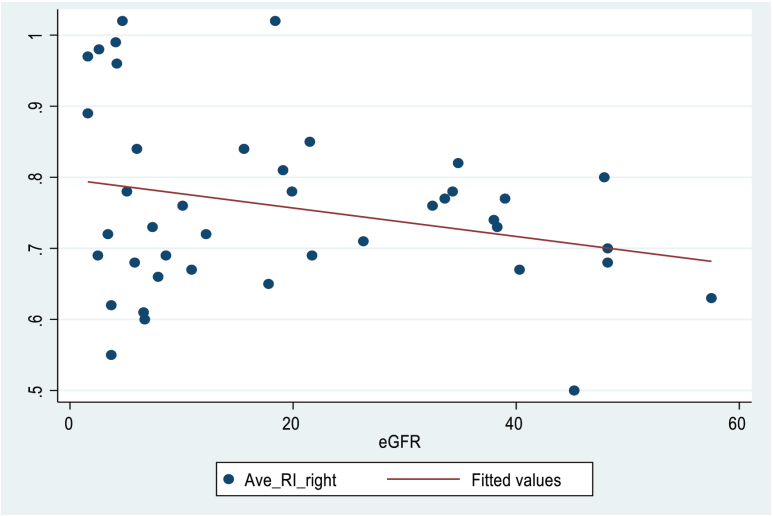

Figure 3. Scatterplot of eGFR (ml/min/m2) and RI of left kidney

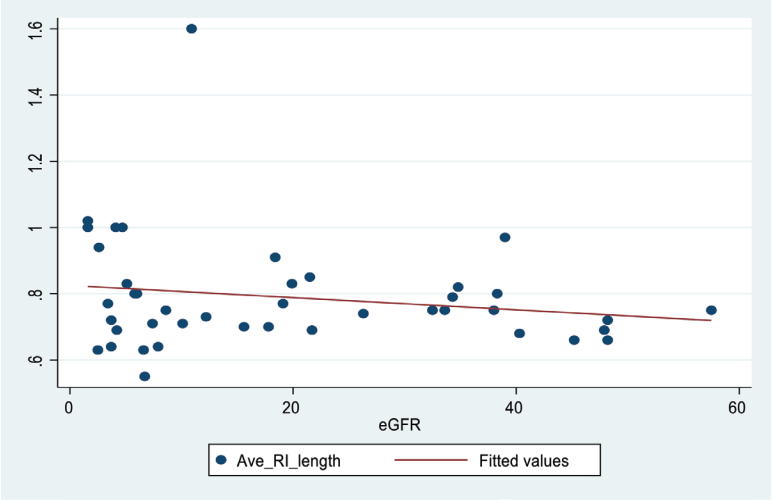

Figure 4. Scatterplot of eGFR (ml/min/m2) and kidney length (cm)

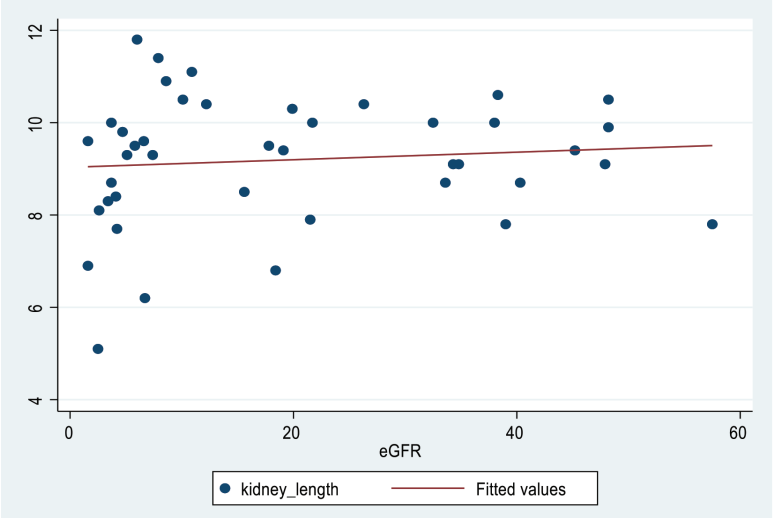

them were Asians with an average age of 56 years (± 16.5246). About 52.4% were male and 47.6% were female. The majority were married (54.8%), followed by single (23.8%), and separated (21.43%) (Table 3).

Resistive index results showed that 61.9% of patients had an abnormal right kidney, while 69.1% had an abnormal left kidney. Patients with renal parenchymal echotexture (RPE) grade I comprised 40.5% of the population, followed by those with RPE grade II at 31.0%, RPE grade III at 23.8%, and RPE grade 0 at 4.8%. The average eGFR was 19.5 ml/min/m2 (± 16.4908), and most of the patients fell in Grade 5 (n=21; 50%), followed by Grade 3b, Grade 4 (n=8; 19.1%), and Grade 3a (n=5; 11.9%). The average kidney length measured 9.19 cm (± 1.3985) (Table 4).

Statistical results showed that patients with eGFR grade 3a had an average right kidney RI of 0.662 (± 0.1096), eGFR Grade 3b patients had an average right-RI of 0.755 (± 0.0438), Grade 4 patients, an average right-RI of 0.794, and Grade 5 patients, an average of 0.768 (± 0.1459) (Table 5a). Meanwhile, the average RI of the left kidney for patients with eGFR grade 3a was 0.696 (± 0.0391), that for patients with Grade 3b had an average of 0.789 (± 0.0848), Grade 4, an average of 0.774 (± 0.0816), and Grade 5, an average of 0.817 (± 0.2277) (Table 5b).

Results of the Kruskal-Wallis test to compare the RIs of the left and right kidneys for each eGFR grade showed no significant difference between each grade (p-value > 0.05).

Comparing the actual eGFR values with the renal parenchymal echogenicity grade (RPEG). the average eGFR for RPEG 0 was 33.90 (± 19.790), RPEG I was 28.76 (± 17.3868); RPEG II, 10.47 (± 9.9457); and RPEG III, 12.47 (± 12.0532).

Using the Krustal-Wallis test, our study found evidence to conclude that a significant difference exists between eGFR and RPEG levels (see Table 6).

The average kidney length of patients with eGFR grade 3a was 9.34 (± 1.0114); those with eGFR grade 3b was 9.25 (± 0.9024); grade 4, 9.10 (± 1.2694); and grade 5, 9.17 (± 1.7161). Kruskal-Wallis test results showed no significant difference between the average kidney length for each eGFR grade (Table 7a). Additionally, only one out of five patients with eGFR grades 3a and 3b had been diagnosed with small kidneys. Meanwhile, two patients with eGFR grade 4 and four with eGFR grade 5 were identified to have abnormally-sized kidneys Table 7b).

Table 8 shows that RI has a weak negative correlation with eGFR (right: -0.1934; left: -0.1640). This means that as eGFR increases, the kidneys' resistivity decreases. Results also showed that the RPEG has a moderate negative correlation with eGFR (-0.4967). This implies that higher eGFR is associated with lower RPEG.

Lastly, kidney lengths positively associated with eGFR (0.1704) although weakly correlated. This indicates that eGFR increases with kidney length. These correlations were confirmed by Figures 2, 3, and 4, wherein the plots reflect linear but almost flat lines. Using Spearman's correlation test, only RPEG demonstrated a significant correlation with eGFR (p-value: 0.008). The remaining parameters did not show evidence of statistical significance (p-value > 0.05).

Discussion

Ultrasonography remains an important diagnostic imaging modality in the evaluation of the kidneys, giving clinicians an overview of renal status and function. Evaluation of renal parenchymal echogenicity, RI, and renal length are sonographic parameters used to correlate kidney status, especially in patients with CKD. Each of these parameters has advantages and disadvantages, as explored in this study.

This study comprised CKD patients, most with increased resistivity indices; however, a poor correlation was found with increasing eGFR grade. Although the samples with deranged RI belonged to CKD patients in stages 3b to 5, a linear correlation could not be established to properly set range RI values for each CKD stage. It has been shown that some factors may influence RI values despite the presence of renal disease; these include systemic vascular resistance, heart rate, and atherosclerosis. Systemic and non-renal factors should be considered in the use of RI for evaluating renal disease.[4] Because of the pitfall as mentioned earlier, studies suggest that RI may be useful for predicting AKI, as values may increase in the setting of sepsis, hepatorenal syndrome and obstructive uropathy. The utility of RI has been correlated with patient age and histological changes such as sclerosis and tubulointerstitial damage in kidney tissue samples. Studies have also shown that in CKD patients with RI values >0.70, there is poorer renal survival compared to patients with RI of <0.65 upon follow-up.[6]

Kidney length showed the least statistically significant correlation with eGFR, although most of the patients with decreased kidney length fell into CKD categories 4 and 5. This implies that changes in renal dimensions may not be sonographically apparent, even though worsening renal function and kidney atrophy are more common at the severe end of the CKD spectrum. This also highlights the relative differences in kidney size based on gender, age, weight, and height.[4] Obtaining renal volume and cortical thickness may be more meaningful in assessing renal status compared to renal length alone. Renal size assessment through ultrasonography has been shown to be of value for residual renal function evaluation in patients who are already undergoing renal replacement therapy.[9]

Findings suggest that renal cortical echogenicity correlates well with eGFR in CKD compared to RI and renal length,. Local and widespread renal cortical changes in the setting of interstitial and cicatricial conditions, respectively, produces consequent linear cortical echogenicity changes. This may be attributed to findings that support significant histologic correlation (glomerular sclerosis, tubular atrophy, interstitial inflammation, and fibrosis) with echogenicity of the renal cortex.

Flow changes, cell infiltration and deposition of substances such as fat, connective tissue and calcium contribute to increased cortical echogenicity of the kidneys.[3] The renal echogenicity grading also correlated well with the use of creatinine levels in patients with CKD in comparison to other sonographic parameters in one study.

Furthermore, changes in renal echogenicity are irreversible compared to serum creatinine levels, which can be corrected with renal replacement therapy. As a tool for determining renal status in CKD patients, sonographic grading of the renal cortex relative to the liver or splenic parenchyma can be performed easily, with a high reproducibility rate.[17]

Conclusion

Parenchymal echogenicity grading can be a useful sonographic parameter, among others, in determining

the renal status of patients with CKD, correlating well with declining levels of eGFR. This may be due to renal parenchymal echogenicity being more representative of changes occurring at the tissue level. In addition, non-renal factors may affect renal length and RI values; thus, they may not correlate well with the current renal status of CKD patients.

For further study, the authors suggest that more than one evaluator be used for RI determination. Increasing sample size and study duration may also be needed. A more meaningful, albeit tedious, measurement may be performed through the acquisition of renal volume rather than length alone.

References

1) Bikbov B, Purcell CA, Levey AS, et al. Global, regional, and national burden of chronic kidney disease, 1990–2017: a systematic analysis for the Global Burden of Disease Study 2017. *The Lancet*. 2020;395(10225):709-733. doi:10.1016/S0140-6736(20)30045-3

2) Tang SCW, Yu X, Chen HC, et al. Dialysis care and dialysis funding in Asia. *Am J Kidney Dis*. 2020;75(5):772-781. doi:10.1053/j.ajkd.2019.08.005

3) Kidney Health Plus Quezon City, Manila. National Kidney and Transplant Institute. https://nkti.gov.ph/index.php/patients-and-visitors/kidney-health-plus.

4) Sutikno DA, Baskoro N. Comparing diagnostic value of renal parenchymal resistive index and cortical echogenicity in chronic kidney disease patients. Resistive Index; renal cortex echogenicity; chronic kidney disease; glomerulus filtration rate (GFR). *Int J Human Health Sci*. 2020;4(3):6. doi:10.31344/ijhhs.v4i3.200

5) Shivashankara VU, Shivalli S, Pai BHS, et al. A comparative study of sonographic grading of renal parenchymal changes and estimated glomerular filtration rate (eGFR) using modified diet in renal disease formula. *J Clin Diagn Res: JCDR*. 2016;10(2):TC09-TC11. doi:10.7860/JCDR/2016/16986.7233

6) Viazzi F, Leoncini G, Derchi LE, Pontremoli R. Ultrasound Doppler renal resistive index: a useful tool for the management of the hypertensive patient. *J Hypertension*. 2014;32(1):149-153. doi:10.1097/HJH.0b013e328365b29c

7) Alaini A, Malhotra D, Rondon-Berrios H, et al. Establishing the presence or absence of chronic kidney disease: Uses and limitations of formulas estimating the glomerular filtration rate. *World J Methodol*. Sep 26 2017;7(3):73-92. doi:10.5662/wjm.v7.i3.73

8) Heine GH, Reichart B, Ulrich C, Köhler H, Girndt M. Do ultrasound renal resistance indices reflect systemic rather than renal vascular damage in chronic kidney disease? *Nephrology Dialysis Transplantation*. 2007;22(1):163-170. doi:10.1093/ndt/gfl484

9) KDIGO 2012 Clinical Practice Guideline for the Evaluation and Management of Chronic Kidney Disease. *Kidney International Supplements*. 2012;3(1)

10) Glassock RJ, Winearls C. Screening for CKD with eGFR: doubts and dangers. *Clin J Am Soc Nephrol*. Sep 2008;3(5):1563-8. doi:10.2215/cjn.00960208

11) Vaidya SR, Aeddula NR. Chronic Kidney Disease. In: *StatPearls*. Treasure Island (FL): StatPearls Publishing; October 24, 2022.

12) Lucisano G, Comi N, Pelagi E, Cianfrone P, Fuiano L, Fuiano G. Can renal sonography be a reliable diagnostic tool in the assessment of chronic kidney disease? *J Ultrasound Med*. Feb 2015;34(2):299-306. doi:10.7863/ultra.34.2.299

13) Yaprak M, Çakır Ö, Turan MN, et al. Role of ultrasonographic chronic kidney disease score in the assessment of chronic kidney disease. *Int Urol Nephrol*. 2017;49(1):123-131. doi:10.1007/s11255-016-1443-4

14) Ahmed S, Bughio S, Hassan M, Lal S, Ali M. Role of ultrasound in the diagnosis of chronic kidney disease and its correlation with serum creatinine level. *Cureus*. Mar 12 2019;11(3):e4241. doi:10.7759/cureus.4241

15) Radermacher J, Ellis S, Haller H. Renal Resistance Index and progression of renal disease. *Hypertension*. 2002;39(2):699-703. doi:10.1161/hy0202.103782

16) Bigé N, Lévy PP, Callard P, et al. Renal arterial resistive index is associated with severe histological changes and poor renal outcome during chronic kidney disease. *BMC Nephrol*. 2012;13:139. doi:10.1186/1471-2369-13-139

17) Karunakar C, T D. Sonographic grading of renal cortical echogenicity and raised serum creatinine in patients with chronic kidney disease. *Int. J Health Clin Res*. 2021;4(8):211-214. https://ijhcr.com/index.php/ijhcr/article/view/1450

Radiation-associated Angiosarcoma of the Breast: A Clinicopathological and Multimodality Imaging Review

Helena Bentley, MD MSc; Joanna Yuen, MD; Malcolm Hayes, MBChB, LRCP, MRCS MMed Path, FRCPath, FRCPC; Tetyana Martin, MD, FRCPC

Abstract

Patients diagnosed with breast cancer who have been treated with breast conserving surgery and radiation therapy have an increased risk of developing radiation-associated angiosarcoma of the breast. With the increased use of breast conserving surgery and radiation therapy in the management of breast cancer, greater awareness and understanding of the disease is required. This review describes the epidemiology, etiology, clinical presentation, imaging features, differential diagnosis, and histopathological features of radiation-associated angiosarcoma of the breast. Multimodality imaging includes mammography, ultrasound, and magnetic resonance imaging. Moreover, we highlight key clinical practice points for radiologists regarding identification and management of the disease.

Key words: breast imaging, breast cancer, angiosarcoma, radiation-associated angiosarcoma

Introduction

Angiosarcomas are malignant tumors that originate from endothelial cells lining vascular channels. They are a rare histologic subtype of soft-tissue sarcomas and they represent only 1 to 2% of all soft-tissue sarcomas.[1] The breast is a common tissue in which angiosarcoma may arise. Angiosarcoma of the breast may arise spontaneously (primary angiosarcoma of the breast) or it may arise secondary to a biological insult (secondary angiosarcoma of the breast), such as radiation therapy (radiation-associated angiosarcoma of the breast [RAAS], Box 1).[2-4]

In recent years, RAAS has become increasingly reported and it has been suggested to be associated with the increased use of breast conserving surgery and radiation therapy in the management of breast cancer.[2,5] Diagnosis of the disease yields poor prognosis with significant metastatic potential.[5] As such, radiologists' ability to appropriately recognize RAAS is integral. We provide a comprehensive review of RAAS as well as a multimodality imaging review of the disease.

Epidemiology

Risk and incidence

Studies have demonstrated that patients diagnosed with breast cancer who are treated with breast conserving surgery and radiation therapy have an increased risk of developing RAAS as compared to those patients who did not receive radiation therapy.[6] Large population-based studies utilizing the Surveillance, Epidemiology, and

Affiliations: Department of Radiology, Faculty of Medicine, University of British Columbia, Vancouver, Canada (Drs Bentley, Yuen, Martin); Department of Pathology and Laboratory Medicine, Faculty of Medicine, University of British Columbia, Vancouver, Canada (Dr Hayes); Department of Pathology and Laboratory Medicine, BC Cancer, Vancouver, Canada (Dr Hayes); Department of Medical Imaging, BC Cancer, Vancouver, Canada (Dr Martin).
Financial Disclosures and Conflicts of Interest: None.
Prior Publication: Figure 2 has been previously published in a manuscript authored by the corresponding author.[12] The authors have obtained permissions for reproduction.

Box 1. Definition of radiation-associated malignancy.

Criteria developed by Cahan and Woodward (1948) and further adapted by Arlen et al (1971) provides specifications for a malignancy to be considered as radiation-associated.[47,48] This criteria includes that: (1) the malignancy must have arisen in a previously irradiated field; (2) the latency period between which the malignancy arose and the radiation therapy occurred is at least 3 years; and (3) the malignancy possesses histological distinction from the primary malignancy.[47,48]

Table 1. Summary of studies reporting the incidence of angiosarcoma of the breast after breast conserving surgery and radiation therapy for the treatment of breast cancer.

REFERENCE	YEARS DURING WHICH DATA WAS COLLECTED	POPULATION STUDIED	NUMBER OF CASES OF BREAST CANCER TREATED WITH RADIATION THERAPY	NUMBER OF CASES OF ANGIOSARCOMA	REPORTED INCIDENCE OF ANGIOSARCOMA
Strobbe et al. (1998)	1987 to 1995 (8 years)	Netherlands	16 500	21	0.16%[a]
Marchal et al. (1999)	1975 to 1996 (21 years)	France*	18 115	9	0.05%
West et al. (2005)	1989 to 1997 (8 years)	California, USA**	423	4	1.11%[b]
Fodor et al. (2006)	1996 to 2004 (8 years)	Hungary**	6 729	8	0.14%[b]
Bentley et al. (2020)	1993 to 2017 (25 years)	British Columbia, Canada	41 094	22	0.05%

[a]Incidence calculated on assumption that 6% of the cohort did not receive radiation and an 85% 5-year survival, [b] Incidence calculated on assumption of 85% 5-year survival, *data reported from 11 of 20 national cancer centers, **data reported from a single center.

End Results (SEER) database have reported the incidence rate of RAAS to be 7.6 per 100 000 person years.[7] Five studies have estimated the incidence proportion of RAAS, with the incidence proportion reported varying from 0.05% to 1.11% (Table 1).[8-12] While certain studies have demonstrated an increased number of cases of RAAS over time, the incidence proportion of RAAS reported over time has not increased.[12,13]

Etiology

The etiology of RAAS remains poorly understood. Genome instability arising from DNA damage and direct tumor induction arising from radiation therapy through mutations of relevant cancer-related genes are thought to be central to pathogenesis.[14] Prolonged cellular stimulation during tissue repair associated with radiation-induced ischemic changes may also have a role in the development of disease. Malignant transformation of pre-existing primary benign lesions after radiation therapy has also been proposed.[14,15]

The risk of RAAS in *BRCA 1/2* patients has also been evaluated. Deficiencies in the DNA repair mechanisms of these patients have been hypothesized to increase radiosensitivity and susceptibility to carcinogenesis in surviving cells.[14] Kadouri et al (2013) observed a high frequency of *BRCA 1/2* mutations among patients diagnosed with RAAS.[16] Nonetheless, while a two-fold increased risk of RAAS among *BRCA 1/2* carriers was estimated, given the rarity of the disease this increased risk was not found to be significant as compared to patients without the mutation.[16] *BRCA 1/2* mutations should thus not be considered in the decision to pursue treatment with radiation therapy, and they ought not to preclude its use.[16]

The use of chemotherapy has not been identified as a risk factor for the diagnosis of RAAS. A systematic review of radiation-associated sarcomas completed by Sheth et al (2012) did not find any association between the use of chemotherapy and the development of the disease.[14]

Clinical Presentation

Radiation Latency

Huang and Mackillop (2001) demonstrated that the risk of developing RAAS is increased within 10 years after radiation therapy, with peak risk being between 5 and 10 years after radiation therapy.[6] Most studies have reported a median radiation latency, defined as the interval between radiation therapy and the development of RAAS, of approximately 7 years.[9,13,12,17-19] Nonetheless, radiation latency may vary greatly, with a range of 11 months to 24 years being reported.[20]

Table 2. Summary of multimodal imaging findings of RAAS.

IMAGING MODALITY	SUMMARY OF IMAGING FINDINGS	IMPORTANT NOTES
Ultrasonography	A hypoechoic, hyperechoic or heterogeneous mass with or without posterior acoustic shadowing may be present.	Imaging findings are nonspecific. Patients with the disease may or may not have imaging findings on ultrasonography.
Mammography	Post-treatment changes following radiation therapy may be observed. An ill-defined, non-calcified mass or focal asymmetry may be observed if the breast parenchyma is involved.	Imaging findings are nonspecific. Post-radiation therapy changes may obscure imaging findings of the disease. Patients with the disease may or may not have imaging findings on mammography.
MRI	Skin thickening, nipple involvement, skin enhancement, cutaneous nodules, and parenchymal masses as well as associated findings of pectoralis muscle involvement or lymphadenopathy may be observed. Hyperintense skin thickening on T2 imaging may be observed as well as hypointense, heterogenous, and hyperintense lesions may also be identified.	MRI is superior to ultrasonography and mammography in the evaluation of RAAS.

Age at Presentation

RAAS generally presents in older women. The median age at presentation is 70 years, with a range of 36 to 92 years being reported.[20]

Clinical Features

The clinical presentation of RAAS varies. RAAS most often affects the dermis, though the disease may also occasionally affect the breast parenchyma.[2,3] Skin changes are often nonspecific and may include discoloration, bruising, nodularity, induration, thickening, fibrosis, telangiectasia, and/or bleeding of the skin. Discoloration associated with RAAS is often described as faint purple, blue, or black or a bruise-like change in the skin.[3,21] A palpable lesion underlying skin changes may also be present.[13] While skin changes are most often localized to the vicinity of the previous surgical site or site of radiation therapy, there may also be diffuse involvement of the breast or adjacent area.[3] Thorough clinical assessment is imperative to avoid the omission of satellite lesions, which are oftentimes identified.[21] Given the nonspecific nature of the clinical presentation of the disease, diagnosis is often challenging, as skin changes or lesions may be easily mistaken for radiodermatitis, trauma, or another cutaneous lesion.[4,21] Of the 21 patients observed by Strobbe et al (1998), 6 patients were reported to have delays in appropriate diagnosis, which was attributed to unfamiliarity with the disease.[8] Documentation of skin changes identified by clinicians or by technologists during image acquisition is thus integral to ensure appropriate diagnosis.

Imaging Features

Imaging features of RAAS are summarized in Table 2.

Mammography

Mammography findings of RAAS are nonspecific. Often only post-treatment changes after radiation therapy may be seen mammographically, including skin thickening, skin retraction, and architectural distortion (Figure 1).[2,22-24] These post-treatment changes may obscure other mammographic findings of the disease.[24] If the breast parenchyma is involved, an ill-defined, non-calcified mass or focal asymmetry of the breast may be observed (Figure 2).[25] Mammographic imaging has also been reported to be negative despite skin changes being observed clinically.[5,26-28]

Ultrasonography

Ultrasound may serve as a useful initial screening modality at sites of previous radiation therapy or previous tumor localization. Ultrasound may also provide temporal comparison if patients develop clinically significant findings at the site of previous radiation therapy, such as skin nodularity or thickening.[29]

Ultrasound imaging findings of RAAS are generally nonspecific. Ultrasound may demonstrate a hypoechoic, hyperechoic, or heterogeneous mass with or without acoustic shadowing. Color Doppler flowmetry may be useful if enhanced vascularity is observed (Figure 3).[2,25] Of the 6 patients observed by Chikarmane et al (2015), 3 patients underwent ultrasound imaging, which revealed skin thickening and non-specific post-radiation therapy skin changes and underlying irregular masses.[22]

Figure 1. (A) Baseline mediolateral oblique view mammogram of the left breast in a 65-year-old female with a prior history of invasive breast cancer treated with partial mastectomy, sentinel lymph node biopsy, and radiation therapy demonstrated post-therapy changes (arrow). (B) Two years later, mild skin thickening of the inferior breast was observed (arrow). (C) Three years later, the skin thickening was noted to have substantially increased (arrow). (D) Histology revealed high-grade RAAS. Irregular sheets of oval and polygonal atypical cells showing numerous mitoses lacking vascular channel formation were observed (arrows).

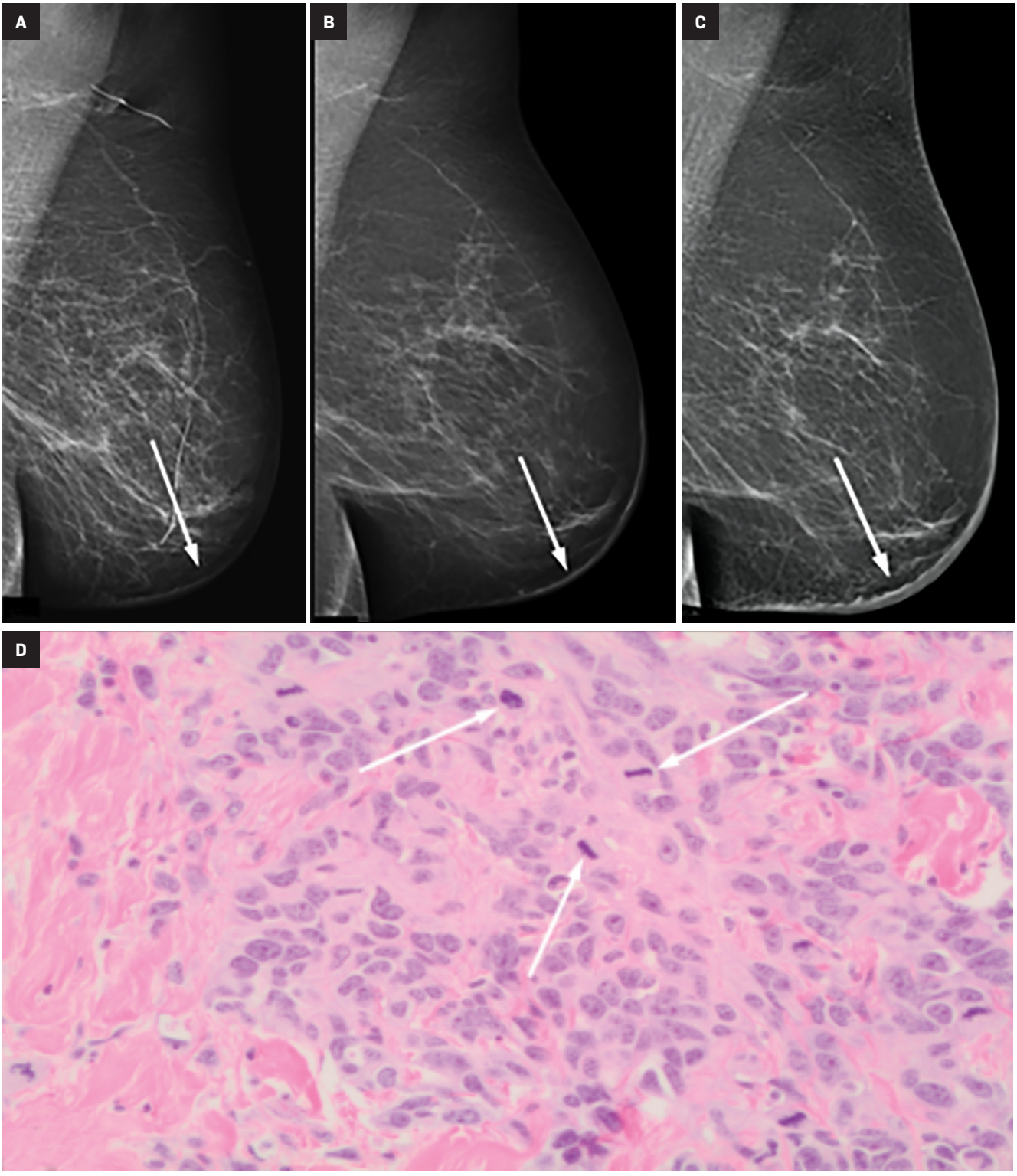

Figure 2. An 82-year-old female with a previous history of left-sided invasive breast cancer managed with partial mastectomy, radiotherapy, and tamoxifen 10 years prior who presented with a lump in the areolar region of the left breast. Mammographic craniocaudal (A) and mediolateral oblique (B) views demonstrated a 2cm focal asymmetry. (C) Ultrasound of the retro-areolar region demonstrated an ill-defined mixed echogenicity mass with minimal internal vascularity.

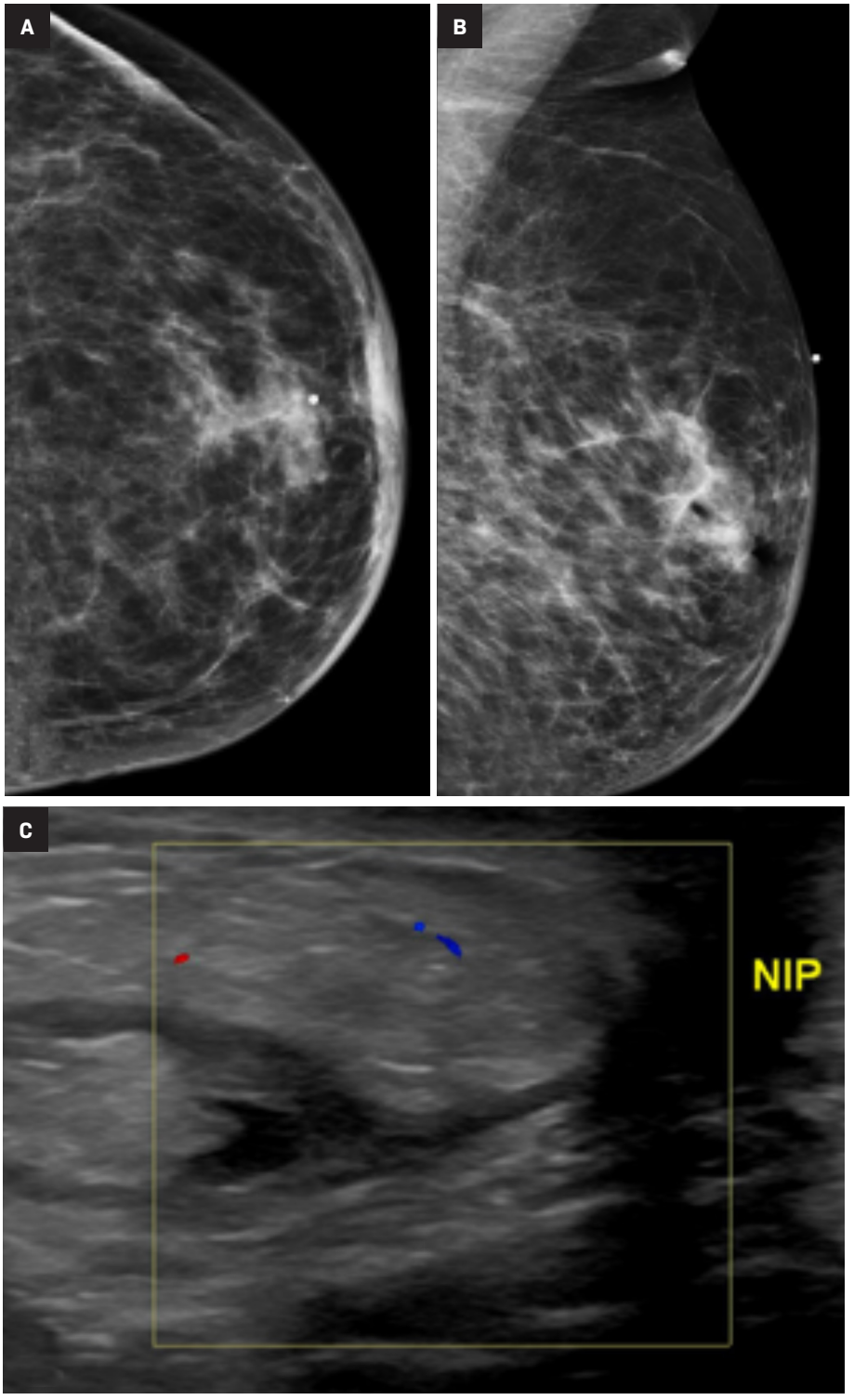

Magnetic Resonance Imaging

Magnetic resonance imaging (MRI) may be utilized as a surveillance modality in patients at high risk for disease recurrence or development of subsequent disease after radiation therapy. The non-specific findings on ultrasonography and potential false negatives on mammography make MRI an exceptionally valuable imaging modality in the evaluation of RAAS.[5] Cutaneous findings, such as skin thickening, skin enhancement, and cutaneous nodules, may be evaluated by MRI. MRI also enables visualization of nipple involvement, parenchymal masses, pectoralis muscle involvement, and lymphadenopathy (Figure 4). Moreover, MRI may assist in identifying residual disease after excisional biopsy and may also guide surgical and treatment planning.[24,29]

MRI findings of 16 patients with RAAS were reported by Chikarmane et al (2015).[22] All patients demonstrated T2 hyperintense skin thickening, while approximately 50% of patients were observed to have discrete lesions with varying intensities and heterogeneity. Four patients had a parenchymal mass, of which all were likewise identified on mammography and 3 were picked up on ultrasonography. Fast initial and washout delayed phase kinetics on contrast enhanced T1 images of cutaneous and intraparenchymal masses were further investigated.[22] Sanders et al (2006) described the MRI findings of two cases of angiosarcoma of the breast.[30] A nodule in the skin adjacent to a lumpectomy scar with fast initial and plateau delayed phase kinetics was observed in 1 patient while cutaneous enhancement at the lumpectomy scar with fast initial and delayed phase washout kinetics was observed in another patient.[30]

Figure 3. A 57-year-old female with previous history of left-sided breast cancer treated with breast conserving surgery and radiation therapy 9 years prior who presented with skin thickening and discoloration of the left breast. Ultrasound images of the left breast at the 12 o'clock position demonstrated a circumscribed heterogenous, hypoechoic mass with minimally irregular margins (A) and positive color Doppler flow (B).

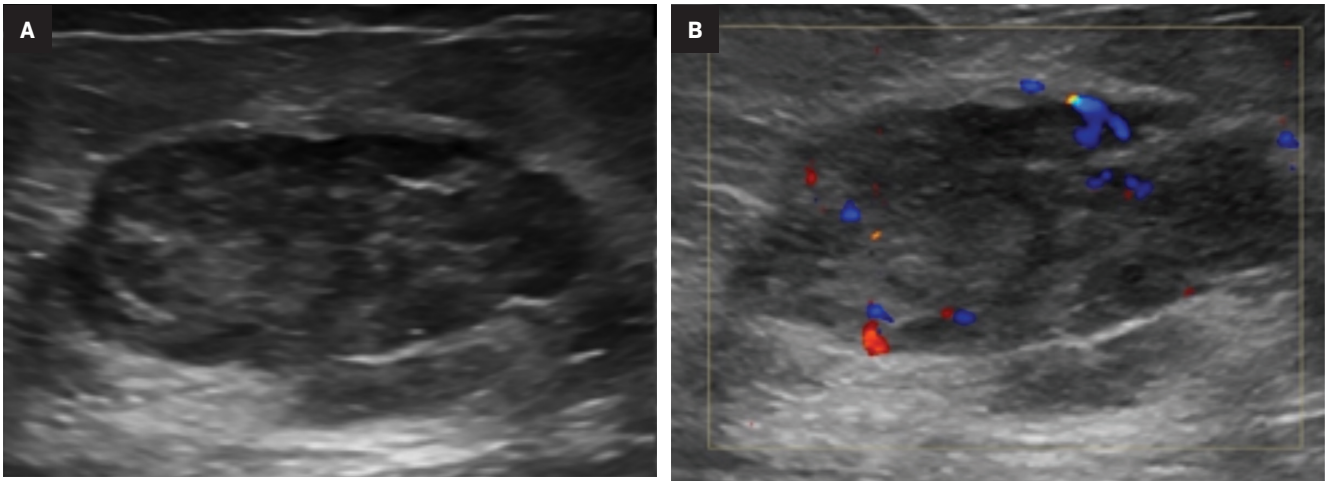

Differential Diagnosis

Radiologists must be aware that RAAS should be included in the differential diagnosis for any skin changes or parenchymal mass in the setting of prior radiation therapy. Decreased prominence of skin thickening and breast density within 2 years after radiation therapy have been reported to be in keeping with the natural course of breast changes following breast conserving surgery and radiation therapy.[24,31-34] Radiologists should be aware of the possibility of recurrent breast carcinoma, inflammatory breast cancer, or mastitis in any patient where an increase in skin thickening or breast density is present years after decreased prominence of these findings. When such findings are accompanied by associated skin discoloration, breast edema, raised skin nodules, papules and/or vesicles, RAAS must be considered in the differential diagnosis.[23,24,29] Observable skin changes or parenchymal masses in a quadrant of the breast distinct from the patient's initial tumour site may further suggest a diagnosis of RAAS.[29]

RAAS ought to also be differentiated from angiosarcoma associated with chronic lymphedema (also known as Stewart-Treves syndrome). While RAAS occurs in the ipsilateral breast or chest wall thereafter radiation therapy, angiosarcoma associated with chronic lymphedema occurs in the ipsilateral lymphedematous extremity after radical mastectomy for the treatment of breast cancer.[5,14]

Diagnosing RAAS

Process

Similar to other neoplasms, diagnosis of RAAS is guided by history and physical examination of the patient, which catalyze appropriate imaging and subsequent histologic confirmation of the disease by tissue diagnosis. For tumors which have a propensity for cutaneous involvement, such as RAAS, skin biopsy may be sufficient for diagnosis though deeper lesions require other techniques.[35] Though fine needle aspiration (FNA) may identify RAAS, core needle biopsy is preferred because of the risk of false negative results secondary to potential inadequate sample volume for appropriate histologic or immunohistochemical evaluation. Of the patients evaluated by Marchal et al (1999), FNA was found to be rarely conclusive.[9] As such, a negative FNA is insufficient to rule out a diagnosis of RAAS in the setting of clinical suspicion for the disease. Should the results of FNA be negative and clinical suspicion for the disease be maintained, core needle biopsy is recommended to obtain an appropriate tissue diagnosis.[8,36-38]

Pathologic and Histologic Features

Tumors may vary significantly in size, with most averaging between 5 to 7 cm. They may be either circumscribed or have infiltrating borders. Areas of hemorrhage may be present. Multifocality is common at the time of presentation and patients may present with extensive involvement of the breast.[14]

The histologic features of RAAS are similar to those of primary angiosarcoma of the breast.[39] However, while nuclear grade usually corresponds to differentiation in primary angiosarcoma of the breast, RAAS generally exhibits poorly differentiated nuclei with

Figure 4. A 79-year-old female with a history of right-sided breast cancer treated with breast conserving surgery, axillary lymph node dissection, and radiation therapy 8 years prior who presented with a painful lump as well as dimpling and contour deformity of the right breast adjacent to the nipple. Mammographic craniocaudal (A) and mediolateral oblique (B) views demonstrated diffuse skin thickening, architectural distortion, and nipple retraction. Ultrasound image (C) demonstrated thickened edematous retroareolar tissue with no distinct mass. Axial T1 (D), T2 fat sat (E), T1 fat sat post-gadolinium subtraction (F), and angiomap (G) MRI images confirmed marked enlargement of the right nipple with edematous patchy involvement and abnormal enhancement extending to the upper outer quadrant of the right breast to the level of the prior surgical scar. Axial CT image (H) demonstrated the right breast being enlarged with increased density in the central breast deep to the nipple with enhancement.

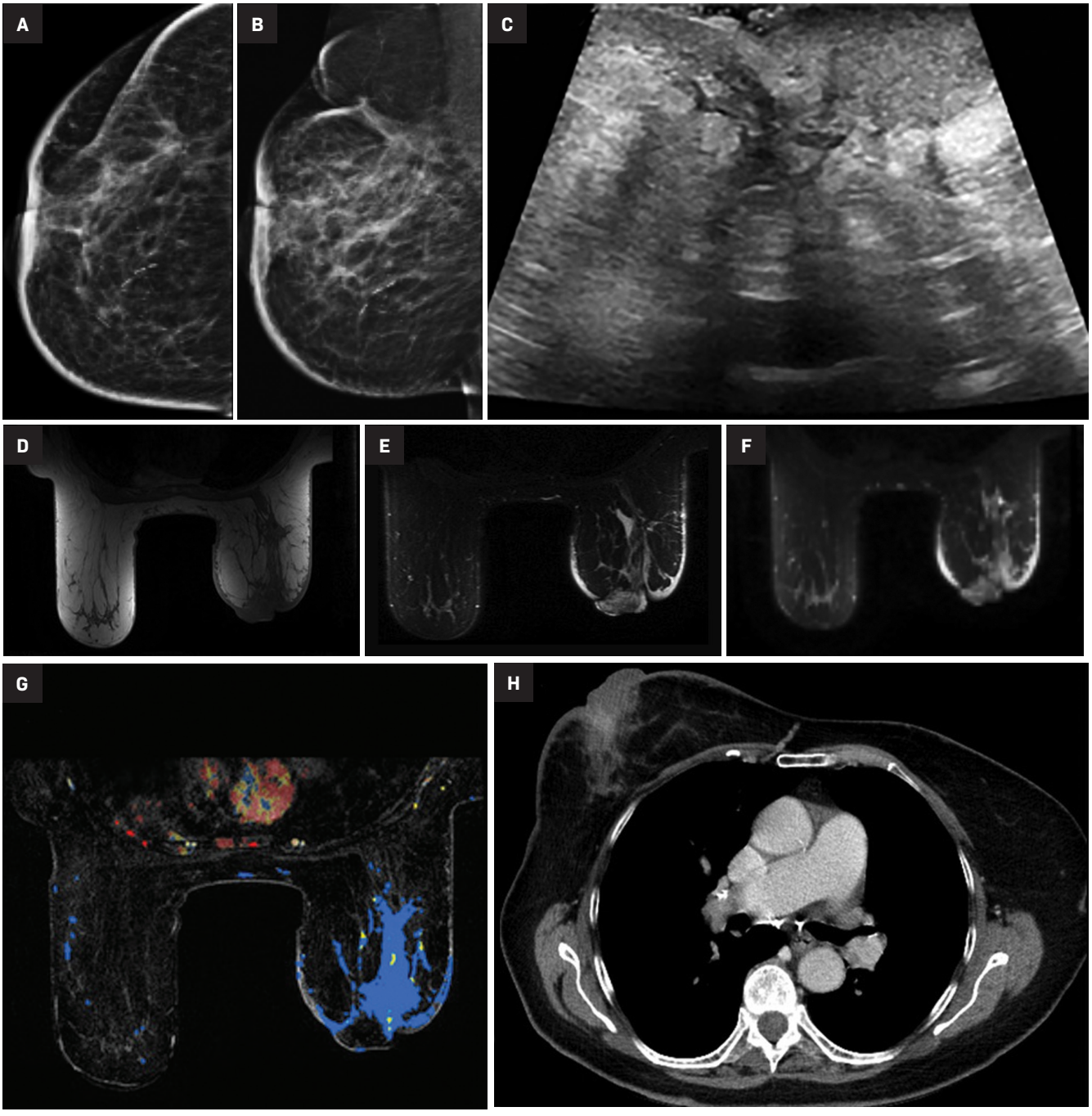

Table 3. Histologic differential diagnosis of RAAS by tumor grade.

TUMOR GRADE	HISTOLOGIC DIFFERENTIAL DIAGNOSIS
High grade	Spindle cell carcinoma Acantholytic variants of squamous cell carcinoma Metaplastic carcinoma
Low grade and intermediate grade	Benign vascular proliferations (hemangiomas, atypical vascular lesions) Nonvascular stromal lesions (pseudoangiomatous stromal hyperplasia, benign papillary endothelial hyperplasia (ie, Masson tumor*)

*Well-known mimic of low-grade angiosarcom

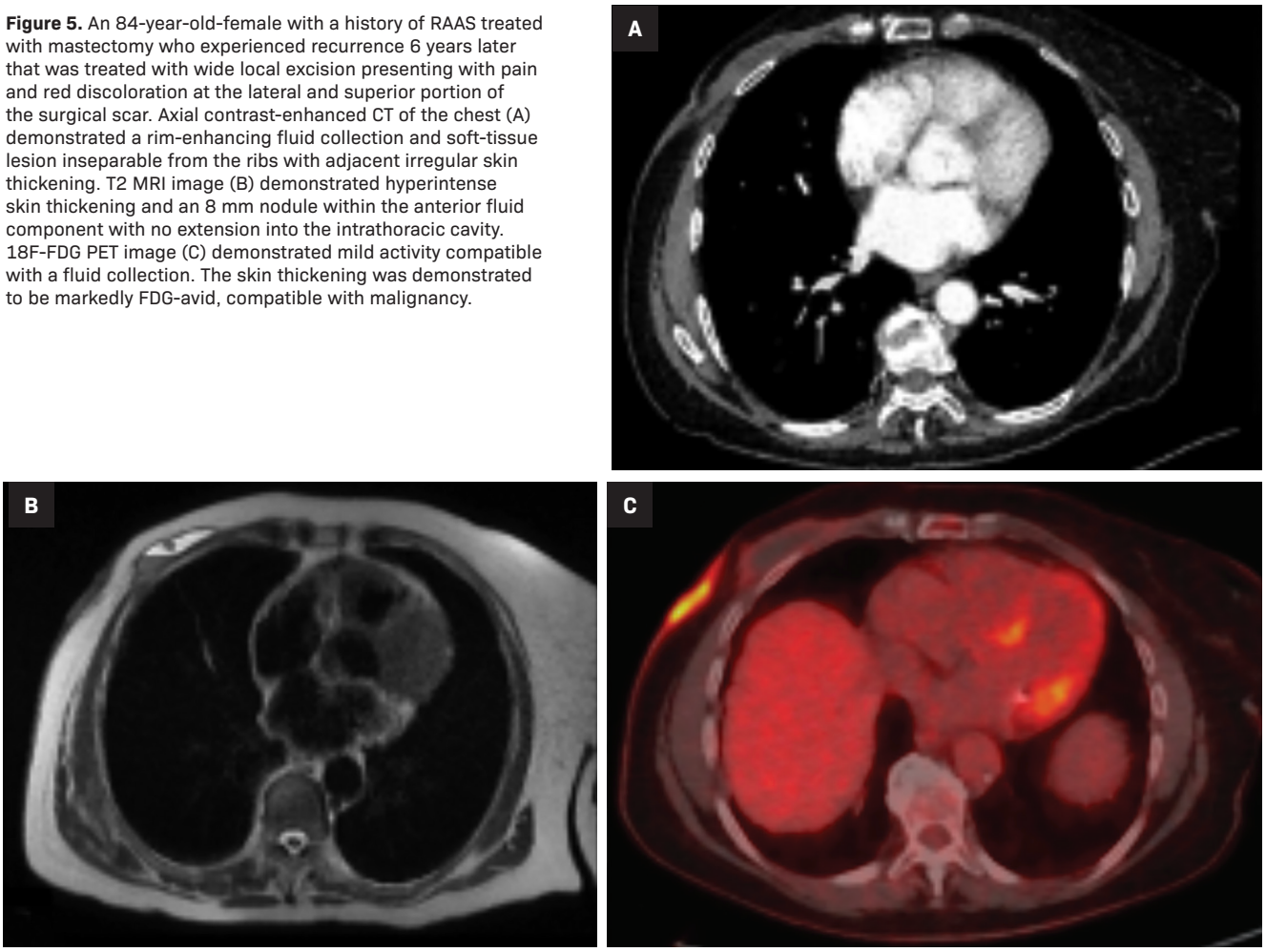

Figure 5. An 84-year-old-female with a history of RAAS treated with mastectomy who experienced recurrence 6 years later that was treated with wide local excision presenting with pain and red discoloration at the lateral and superior portion of the surgical scar. Axial contrast-enhanced CT of the chest (A) demonstrated a rim-enhancing fluid collection and soft-tissue lesion inseparable from the ribs with adjacent irregular skin thickening. T2 MRI image (B) demonstrated hyperintense skin thickening and an 8 mm nodule within the anterior fluid component with no extension into the intrathoracic cavity. 18F-FDG PET image (C) demonstrated mild activity compatible with a fluid collection. The skin thickening was demonstrated to be markedly FDG-avid, compatible with malignancy.

vesicular chromatin, prominent nucleoli, and mitotic activity, and it is usually associated with high grade lesions.[14]

Table 3 summarizes the histologic differential diagnosis of RAAS by tumor grade.[14] There is a lack of consensus with respect to the risk of developing angiosarcoma after the diagnosis of atypical vascular lesions.[14,40,41] While some reports suggest these lesions to be benign, others have documented either subsequent progression to angiosarcoma or the presence of angiosarcoma within the same region.[14,40]

Diagnosis of RAAS is confirmed by means of immunohistochemistry staining with the following being expressed: erythroblast

Box 2. Clinical practice points for radiologists.

1. RAAS must be included in the differential diagnosis for any skin changes or breast parenchymal mass that is observed in the setting of prior radiation therapy.
2. Imaging findings are often nonspecific, with MRI being superior to ultrasonography and mammography in the identification of the disease.
3. A negative FNA is insufficient to rule out a diagnosis of RAAS if there is clinical suspicion of the disease. Core needle biopsy is recommended for diagnosis.

transformation specific related gene (transcription factor that confirms vascular lineage), cluster of differentiation 31 (platelet endothelial cell adhesion molecule), cluster of differentiation 34 (human hematopoietic progenitor cell antigen), factor VIII related antigen, Myc protein, and tyrosine kinase receptor KIT (cluster of differentiation 117).[20,24,42,43]

Staging

Upon diagnosis of RAAS, staging with positron emission tomography (PET) with fluorodeoxyglucose (18F-FDG) may be completed (Figure 5). Lesions with high maximum standardized uptake values (SUV_{max}) have been associated with poor prognosis.[44]

The contralateral breast, chest wall, lungs, liver, and skeleton are frequent sites of metastases.[2,20,45] Metastatic disease may be preceded by one or more instances of local recurrence.[20]

Conclusion

RAAS is a rare but important complication of radiation therapy. With the increased use of breast conserving surgery and radiation therapy in the management of breast cancer, greater awareness and understanding of the disease is required. The clinical presentation of RAAS is variable and appropriate diagnosis is often challenging as skin changes or lesions may be easily mistaken for other entities. Ultrasound may serve as an initial screening modality for the disease but ultrasound findings are nonspecific. Mammographic findings of the disease are likewise nonspecific and may be obscured by expected post-treatment changes after radiation therapy. MRI is superior to ultrasonography and mammography in the evaluation of RAAS. Radiologists must be aware of the disease and its inclusion in the differential diagnosis for any skin changes or breast parenchymal mass that is observed in the setting of prior radiation therapy.

References

1) Cormier JN & Pollock RE. Soft tissue sarcomas. *CA: Cancer J*. 2004;54(2):94-109.

2) Glazebrook KN, Magut MJ, Reynolds C. Angiosarcoma of the breast. *AJR*. 2008;190:533–538.

3) Gaballah AH, Jensen CT, Palmquist S, et al. Angiosarcoma: clinical and imaging features from head to toe. *Brit J Radiol.* 2017;90:0039.

4) Esposito E, Avino F, di Giacomo R, et al. Angiosarcoma of the breast, the unknown-a review of the current literature. *Trans Cancer Res*. 2019; 8:S510-S517.

5) Sheth GR, Cranmer LD, Smith BD, et al. Radiation-induced sarcoma of the breast: a systematic review. *The Oncologist*. 2012;17(3):405.

6) Huang J, Mackillop WJ. Increased risk of soft tissue sarcoma after radiotherapy in women with breast carcinoma. *Cancer*. 2001;92(1):172–180.

7) Mery CM, George S, Bertagnolli MM, et al. Secondary sarcomas after radiotherapy for breast cancer: Sustained risk and poor survival. *Cancer*. 2009;115:4055–4063.

8) Strobbe LJ, Peterse HL, van Tinteren H, et al. Angiosarcoma of the breast after conservation therapy for invasive cancer, the incidence and outcome: an unforeseen sequela. *Breast Cancer Res Treat*. 1998;47:101–109.

9) Marchal C, Weber B, de Lafontan B. Nine breast angiosarcomas after conservative treatment for breast carcinoma: a survey from French comprehensive Cancer Centers. *Int J Radiat Oncol Biol Phys*. 1999;44:113–119.

10) West JG, Quereshi A, West JE, et al. Risk of angiosarcoma following breast conservation: a clinical alert. *Breast J*. 2005;11:115–123.

11) Fodor J, Orosz Z, Szabo E, et al. Angiosarcoma after conservation treatment for breast carcinoma: our experience and a review of the literature. *J Am Acad Dermatol*. 2006;54:499–504.

12) Bentley H, Roberts J, Hayes M, et al. The role of imaging in the diagnosis of primary and secondary breast angiosarcoma: twenty-five-tear experience of a provincial cancer institution. *Clin Breast Cancer*. 2022;23(2):e45-e53.

13) Scow JS, Reynolds CA, Degnim AC, et al. Primary and secondary angiosarcoma of the breast: the Mayo Clinic Experience. *J Surg Onc*. 2010;101:401-407.

14) Shah S and Marilin R. Radiation-associated angiosarcoma of the breast: clinical and pathologic features. *Arch Pathol Lab Med*. 2016;140(5):477-481.

15) Kelly NP & Siziopikou K. A 68-year-old woman with bluish discoloration of the skin of the breast. *Arch Pathol Lab Med*. 2002;126(8):989–990.

16) Kadouri L, Sagi M, Goldberg Y, et al. Genetic predisposition to radiation induced sarcoma: possible role for BRCA and p53 mutations. *Breast Cancer Res Treat*. 2013;140(1):207–211.

17) Hodgson N, Bowen-Wells C, Moffat F, et al. Angiosarcomas of the breast: A review of 70 cases. *Am J Clin Oncol.* 2007;30:570–573.

18) Vorburger SA, Xing Y, Hunt KK, et al. Angiosarcoma of the breast. *Cancer*. 2005;104:2682–2688.

19) Luini A, Gatti G, Diaz J, et al. Angiosarcoma of the breast: The experience of the European Institute of Oncology and a review of the literature. *Breast Cancer Res Treat*. 2007;105:81–85.

20) Abbott R & Palmieri C. Angiosarcoma of the breast following surgery and radiotherapy for breast cancer. *Nat Clin Pract Oncol*. 2008;5(12):727-736.

21) Bonito FJP, de Almeida Cerejeira D, Dahlstedt-Ferreira C, et al. Radiation-induced angiosarcoma of the breast: A review. *Breast J*. 2020;26(3):458-463.

22) Chikarmane SA, Gombos EC, Jagadeesan J, et al. MRI findings of radiation-associated angiosarcoma of the breast. *J Magn Reson Imaging*. 2015;42:763–770.

23) Rubin E, Maddox WA, Mazur MT. Cutaneous angiosarcoma of the breast 7 years after lumpectomy and radiation therapy. *Radiology*. 1990;174:258–260.

24) Chesebro AL, Chikarmane SA, Gombos EC, et al. Radiation-associated angiosarcoma of the breast: what the radiologist needs to know. *AJR*. 2016;207(1):217-225.

25) Burns E, Gupta P, Leonard D. Radiation-induced angiosarcoma of the breast. *Appl Radiol*. 2018;47(3):31A-31C.

26) Mermershtain W, Cohen AD, Koretz M, et al. Cutaneous angiosarcoma of breast after lumpectomy, axillary lymph node dissection, and radiotherapy for primary breast carcinoma: Case report and review of the literature. *Am J Clin Oncol*. 2002;25:597–598.

27) Deutsch M & Rosenstein MM. Angiosarcoma of the breast mimicking radiation dermatitis arising after lumpectomy and breast irradiation: A case report. *Am J Clin Oncol*. 1998;21:608-609.

28) Williams EV, Banerjee D, Dallimore N, et al. Angiosarcoma of the breast following radiation therapy. *Eur J Surg Oncol*. 1999;25:221–222.

29) Moore A, Hendon A, Hester M, et al. Secondary angiosarcoma of the breast: can imaging findings aid in the diagnosis? *Breast J*. 2008;14:293–298.

30) Sanders LM, Groves AC, Schaefer S. Cutaneous angiosarcoma of the breast on MRI. *AJR*. 2006;188:W143–W146.

31) Dershaw DD, Shank B, Reisinger S. Mammographic findings after breast cancer treatment with local excision and definitive irradiation. *Radiology*. 1987;164:455–461.

32) Peters ME, Fagerholm MI, Scanlan KA, et al. Mammographic evaluation of the postsurgical and irradiated breast. *RadioGraphics*. 1988;8:873–899.

33) Harris KM, Costa-Greco MA, Baratz AB, et al. The mammographic features of the postlumpectomy, postirradiation breast. *RadioGraphics*. 1989;9:253–268.

34) Chansakul T, Lai KC, Slanetz PJ. The post-conservation breast: part 2, imaging findings of tumor recurrence and other long-term sequelae. *AJR*. 2012;198:331–343.

35) Vesoulis Z & Cunliffe C. Fine-needle aspiration biopsy of post-radiation epithelioid angiosarcoma of breast. *Diagn Cytopathol*. 2000;22:172–175.

36) Sessions SC & Smink RD. Cutaneous angiosarcoma of the breast after segmental mastectomy and radiation therapy. *Arch Surg*. 1992;127:1362–1363.

37) Majeski J, Austin RM, Fitzgerald RH. Cutaneous angiosarcoma in an irradiated breast after breast conservation therapy for cancer: Association with chronic breast lymphedema. *J Surg Oncol*. 2000;74:208–213.

38) Gherardi G, Rossi S, Perrone S, et al. Angiosarcoma after breast-conserving therapy: Fine-needle aspiration biopsy, immunocytochemistry, and clinicopathologic correlates. *Cancer*. 2005;105:145–151.

39) Lucas DR. Angiosarcoma, radiation-associated angiosarcoma, and atypical vascular lesion. *Arch Pathol Lab Med*. 2009;133(11):1804–1809.

40) Patton KT, Deyrup AT, Weiss SW. Atypical vascular lesions after surgery and radiation of the breast: a clinicopathologic study of 32 cases analyzing histologic heterogeneity and association with angiosarcoma. *Am J Surg Pathol*. 2008;32(6):943-950.

41) Fraga-Guedes C, Gobbi H, Mastropasqua MG, et al. Clinicopathological and immunohistochemical study of 30 cases of post-radiation atypical vascular lesion of the breast. *Breast Cancer Res Treat*. 2014;146(2):347–354.

42) Brenn T & Fletcher CD. Postradiation vascular proliferations: an increasing problem. *Histopathology*. 2006;48:106–114.

43) Morgan EA, Kozono DE, Wang Q, et al. Cutaneous radiation-associated angiosarcoma of the breast: poor prognosis in a rare secondary malignancy. *Ann Surg Oncol*. 2012;19:3801–3808.

44) Cassou-Mounat T, Champion L, Bozec L. Primary and secondary breast angiosarcoma: FDG PET/CT series. *Clin Nucl Med*. 2019;44(1):e33-e35.

45) Billings SD, McKenney JK, Folpe AL, et al. Cutaneous angiosarcoma following breast-conserving surgery and radiation: an analysis of 27 cases. *Am J Surg Pathol*. 2004;28:781–788.

46) Cahan WG & Woodard HQ. Sarcoma arising in irradiated bone; report of 11 cases. *Cancer*. 1948;1:3–29.

47) Arlen M, Higinbotham NL, Huvos AG. Radiation-induced sarcoma of bone. *Cancer*. 1971;28:1087–1099.

Somatostatin Receptor PET Imaging of Physiologic and Benign Processes: Implications for Image Interpretation, Avoiding Pitfalls, and Clinical Applications

William Y. Raynor, MD; Jeffrey S. Kempf, MD

Abstract

Purpose: Somatostatin receptors (SSTR) are expressed by neuroendocrine cells in various organs, including in the spleen, thyroid gland, pituitary gland, and adrenal glands. Neuroendocrine tumors (NETs), which often demonstrate high levels of SSTR2, can be detected by positron emission tomography (PET) imaging with somatostatin analogs labeled with either 68Ga or 64Cu. The most common of these analogues (DOTATATE, DOTATOC, and DOTANOC) bind to SSTR2, with affinity to additional SSTR isoforms variable among the three tracers. Tracer activity due to benign processes and variations in normal tissue SSTR expression has implications for both the interpretation of SSTR PET imaging as well as potential future applications of this modality.

Methods: PubMed was searched separately using "DOTATATE," "DOTATOC," and "DOTANOC" as keywords, and results pertaining to neoplasms such as NET, pheochromocytoma, paraganglioma, and meningioma were excluded.

Results: Relevant original articles, case reports, and review articles were grouped between physiologic and benign observations regarding SSTR PET. A comprehensive review of the literature provided insights into image interpretation and new potential applications in assessing inflammatory disorders.

Conclusions: Variations in splenic and pancreatic tissue can cause diagnostic uncertainty and potential misinterpretation. Preliminary data suggest a role for SSTR PET to characterize atherosclerosis and sarcoidosis.

Keywords: Gallium-68, Copper-64, Biodistribution, Uncinate process, Splenule

Introduction

A neuropeptide first described in 1973,[1] somatostatin generally serves to inhibit the release of other hormones such as growth hormone, insulin, and prolactin in addition to its role as a neurotransmitter.[2] Somatostatin exerts its effects by binding to somatostatin receptors (SSTR), which are expressed on the surface of neuroendocrine cells. The five isoforms of SSTR, identified as SSTR1-5, have different patterns of expression depending on anatomic location. For example, SSTR2 is highly expressed in the spleen,[3] SSTR1 and SSTR2 are expressed in the thyroid gland,[4] while varying levels of SSTR1-5 are expressed by the pancreas.[5]

Because most neuroendocrine tumors (NETs) contain high levels of SSTR2, scintigraphy with the somatostatin analogue ^{111}In-DTPA-octreotide, which binds to SSTR2 with high affinity as well as to SSTR3 and

Affiliation: Department of Radiology, Rutgers Robert Wood Johnson Medical School, New Brunswick, NJ.
Disclosures: The authors declare no conflicts of interest.

SSTR5 to a lesser degree,[6] has been successfully employed for imaging of NETs since the first clinical trials in 1992.[7] Recently, positron-emitting SSTR radiotracers labeled with ^{68}Ga or ^{64}Cu and imaged with positron emission tomography/computed tomography (PET/CT) were able to achieve superior image quality with lower patient radiation exposure given their higher affinity to SSTR2 and shorter radionuclide half-lives compared to ^{111}In-DTPA-octreotide.[8] Of the PET tracers commonly used, DOTATATE binds to SSTR2 with high specificity; DOTATOC, SSTR2 and SSTR5; DOTANOC, SSTR2, SSTR3, and SSTR5.[9] When labeled with the beta-emitting ^{177}Lu, DOTATATE can act as a theranostic agent for the treatment of well-differentiated NETs by exposing tumor cells to reactive oxygen species, resulting in oxidative damage and cell death.[10]

Given the variable expression of SSTR in normal tissues, physiologic uptake can occasionally mimic pathology. Alternatively, SSTR activity associated with benign disorders could lead to new indications for SSTR PET imaging in patients without known or suspected NET.

In this article, we review the sources of potential false positive findings and discuss new potential non-neoplastic indications for PET/CT imaging with radiolabeled DOTATATE, DOTATOC, and DOTANOC.

Methods

A literature search of publications between January 1, 1980, and August 31, 2023, was performed using PubMed. The SSTR PET tracers in clinical use "DOTATATE," "DOTATOC," and "DOTANOC" were used separately as keywords, and results pertaining to neoplastic etiologies, including NET, pheochromocytoma, paraganglioma, and meningioma, were excluded. References contained within the selected articles also received consideration. No restrictions were applied regarding sample size, study design, or outcome measures. Editorials, commentaries, and letters were excluded, as well as pre-clinical studies and those which fell outside of the scope defined by physiologic and benign causes of increased SSTR activity.

Finally, a comprehensive review was created, focusing on false-positive considerations during image interpretation and the potential for imaging of inflammation with SSTR PET.

Results

Physiologic Uptake and Pitfalls

The highest physiologic uptake of ^{68}Ga-DOTATATE is generally in the spleen (Figure 1), where increased SSTR2 expression has been found specifically in the red pulp.[11] Uptake levels in the adrenal glands, pituitary gland, and kidneys demonstrate high intensity, with activity in the kidneys and urinary tract being nonspecific for SSTR expression given the presence of renal excretion.

^{68}Ga-DOTATATE localization to the salivary glands, thyroid, and liver is moderate, with nonspecificity of hepatic activity similarly due to excretion.[12] Similar patterns of intense splenic activity followed by prominent renal and hepatic activity are present in PET/CT images obtained with ^{68}Ga-DOTATOC and ^{68}Ga-DOTANOC.[13,14] Although labeling SSTR tracers with either ^{68}Ga or ^{64}Cu does not affect their biodistribution, the improvement in spatial resolution resulting from the lower positron range of ^{64}Cu suggests that ^{64}Cu-labeled agents may achieve wider clinical use in the future.[15,16]

In a study of 120 patients by Boy et al, the authors observed significantly higher ^{68}Ga-DOTATOC uptake in the uncinate process of the pancreas compared to that in the pancreatic head, body, and tail.[4]

Figure 1. ^{68}Ga-DOTATATE PET/CT maximum intensity projection (MIP) demonstrating normal tracer biodistribution.

This common finding among all SSTR PET agents has been described as a classic pitfall,[17] which is often more diffuse and less intense compared to the well-defined focal uptake associated with NETs in this region (Figure 2).[18] Lakhotia et al considered 775 patients imaged with ^{111}In-DTPA-octreotide, ^{68}Ga-DOTATATE, ^{68}Ga-DOTATOC, and ^{68}Ga-DOTANOC from eight studies and found increased physiologic uptake in the pancreatic head and uncinate process in 229 patients (29.5%).[18-26] Similarly, Tabacchi et al found increased ^{68}Ga-DOTANOC uptake at the uncinate process in

Figure 2. Physiologic uptake of ^{68}Ga-DOTATATE in the uncinate process (arrows) of the pancreas with maximum SUV 5.5 as demonstrated on axial PET (A), CT (B), and fused PET/CT images (C). In the same patient, well-differentiated neuroendocrine tumor is present in the duodenal bulb (arrowheads, D-F), with much higher focal uptake by comparison (maximum SUV 30.8).

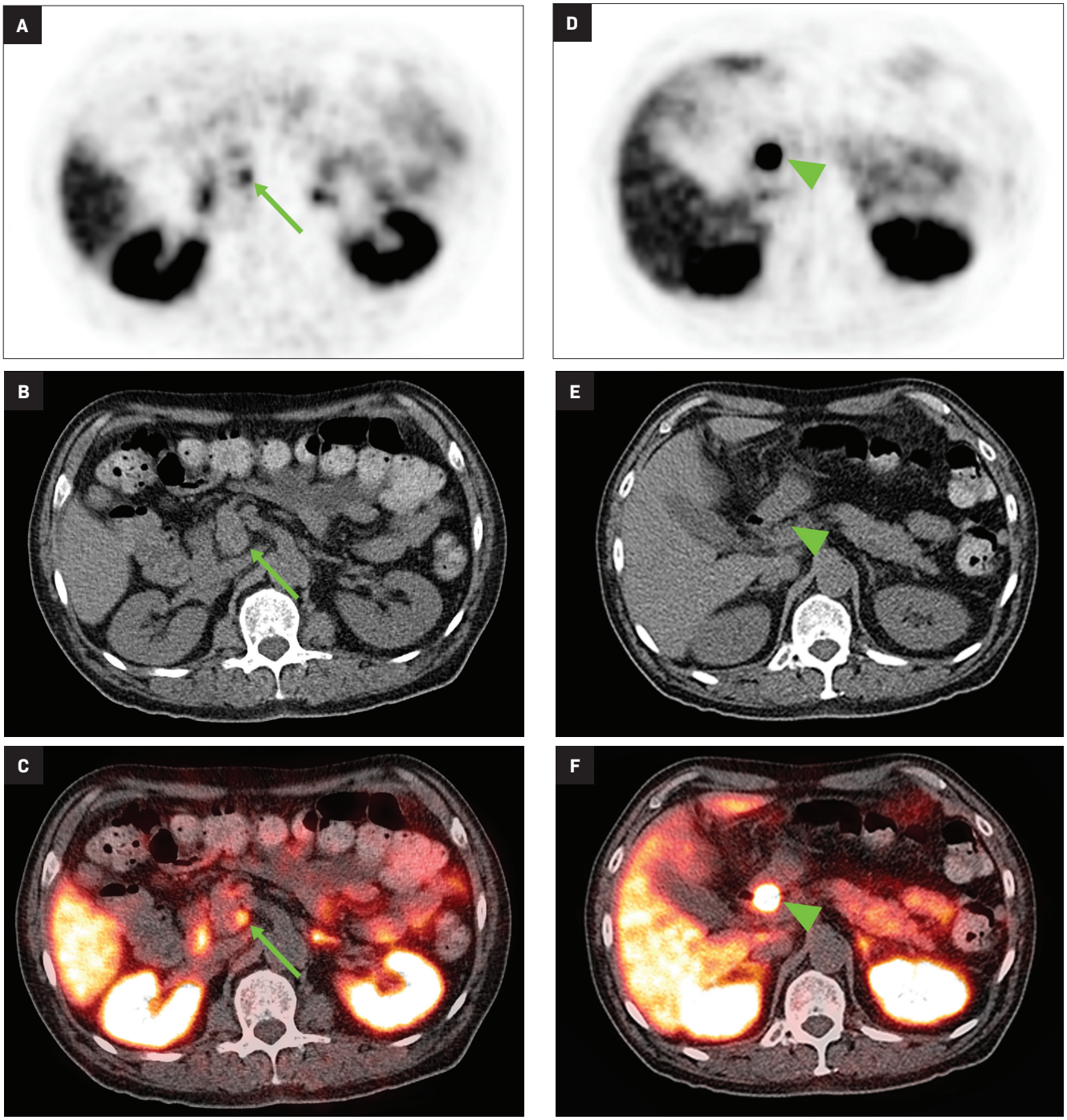

77 out of 172 patients considered (44.8%).[17] The uncinate process in particular has been found to contain an increased numbers of pancreatic polypeptide cells, which highly express SSTR.[27] Brabander et al observed that increased ^{111}In-DTPA-octreotide localization to the uncinate process was more common in patients with diabetes mellitus, which is associated with increased serum pancreatic polypeptide, further supporting pancreatic polypeptide cell hyperplasia as a possible mechanism to explain uncinate

Figure 3. Axial ^{68}Ga-DOTATATE PET (A), CT (B), and fused PET/CT (C) images showing mildly increased tracer uptake (maximum SUV 5.5) regional to the pancreatic tail (arrows). Stable regional tracer activity 16 months later (arrowheads, D-F), maximum SUV 6.4, suggests a benign etiology such as islet cell hyperplasia.

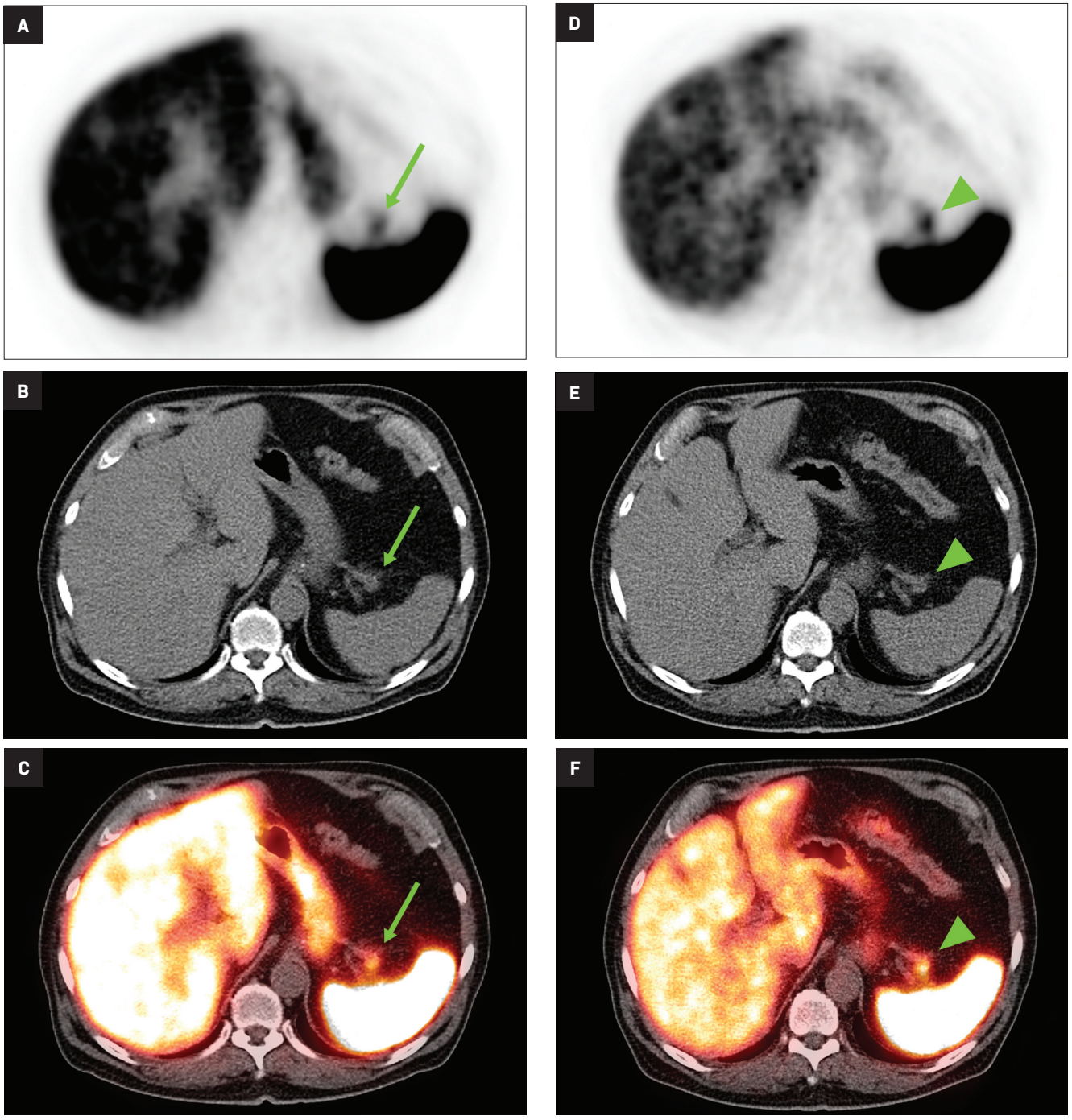

process activity.[20] Although Kroiss et al report successfully using standardized uptake values (SUVs) to differentiate physiologic and pathologic uptake,[28] Krascz found that even in patients with suspiciously high SUVs in the uncinate process, correlative imaging with CT and MRI often reveals no underlying lesion to suggest presence of tumor.[22] Thus, cautious image interpretation taking into account this potential pitfall and consideration of additional evaluation with contrast-enhanced CT or MRI are necessary for

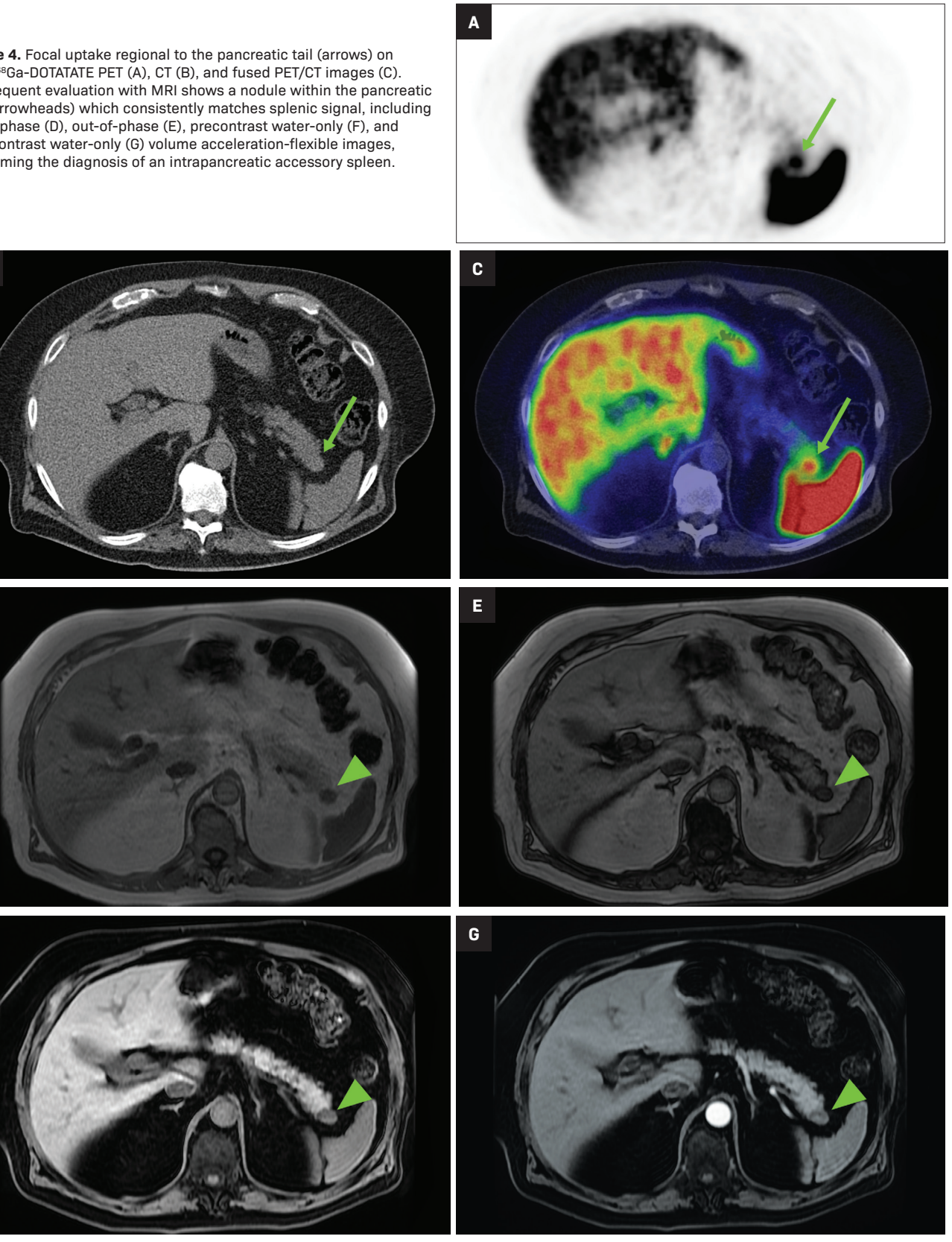

Figure 4. Focal uptake regional to the pancreatic tail (arrows) on axial ^{68}Ga-DOTATATE PET (A), CT (B), and fused PET/CT images (C). Subsequent evaluation with MRI shows a nodule within the pancreatic tail (arrowheads) which consistently matches splenic signal, including on in-phase (D), out-of-phase (E), precontrast water-only (F), and postcontrast water-only (G) volume acceleration-flexible images, confirming the diagnosis of an intrapancreatic accessory spleen.

accurate interpretation of pancreatic uptake in SSTR PET.

Although SSTR radiotracers are not known to localize to the pancreatic tail to the same degree as the uncinate process, variability in this region could similarly lead to diagnostic uncertainty. Focal islet cell hyperplasia has been reported as a possible mechanism causing increased SSTR expression in the pancreatic tail in patients with high physiologic activity (Figure 3).[29] A study in 35 patients by Delbeke et al found that physiologic uptake within the pancreatic tail is typically equal or less than that of the liver.[29] Therefore, quantification with SUVs, as well as correlation with CT or MRI, could play a role in discriminating normal and malignant activity in the pancreatic tail.

Related to the intense physiologic uptake demonstrated by the spleen, accessory spleen SSTR activity is similarly high, which can acquire an appearance suspicious for NET involvement, especially if intrapancreatic (Figure 4).[30-32] Splenosis, often occurring after trauma or splenectomy, represents another atypical splenic tissue distribution that can resemble malignant activity.[33] By assessing whether ^{99m}Tc-labeled sulfur colloid or heat-denatured red blood cell scintigraphy is able to confirm the presence of splenic tissue rather than tumor, misdiagnosis and subsequent high-risk intervention are potentially avoidable.[34]

Imaging of Inflammation

White blood cells such as macrophages are known to express SSTR2, resulting in low grade uptake associated with inflammation. As a result, a variety of inflammatory conditions imaged by SSTR PET/CT have been reported in the literature, including endometriosis, large vessel vasculitis, idiopathic pulmonary fibrosis, and pulmonary tuberculosis.[35-39]

SSTR PET has shown preliminary success in assessing systemic sarcoidosis. ^{68}Ga-DOTATOC PET/CT was compared to ^{67}Ga scintigraphy in a study of 20 sarcoidosis patients by Nobashi et al, who noted ^{68}Ga-DOTATOC-positive lesions in 19 patients and ^{67}Ga-positive lesions in 17 patients.[40] These results not only indicate that SSTR PET is a feasible method of assessing sarcoidosis-related inflammation, but also that its performance may be similar or better than that of ^{67}Ga, which is an established marker of infection and inflammation.

A study which corroborates this finding used ^{68}Ga-DOTANOC PET/CT in 39 patients and observed a sensitivity of 93% and a specificity of 83% in the diagnosis of sarcoidosis, associated with decreased activity after treatment with symptomatic improvement.[41] The described correlation between imaging and clinical improvement thus provides convergent validity for this approach.

A case report showing focal intracranial ^{68}Ga-DOTATATE in the cavernous sinus of a symptomatic patient suggests a role for SSTR PET/CT in neurosarcoidosis, which was confirmed via biopsy.[42] In addition to new potential clinical indications for imaging, these early observations also indicate that presence of sarcoidosis could complicate image interpretation in patients undergoing assessment for SSTR-positive neoplasm.

In light of the growing role of ^{18}F-fluorodeoxyglucose (FDG) PET/CT in cardiac sarcoidosis, experiences using SSTR PET/CT for the same indication have started to appear.[43-48] A 2016 study by Gormsen et al compared PET/CT with ^{18}F-FDG and ^{68}Ga-DOTANOC in a prospective analysis of 19 patients with suspected cardiac sarcoidosis.[49] The authors found that while ^{18}F-FDG findings were inconclusive in 11 patients, there were no inconclusive ^{68}Ga-DOTANOC studies. The overall diagnostic accuracy of ^{18}F-FDG for cardiac sarcoidosis was reported as 79%, compared to an overall accuracy of 100% for ^{68}Ga-DOTANOC in this small cohort.

A more recent study published in 2021 by Bravo et al showed that in 13 subjects with suspected cardiac sarcoidosis, all of whom had positive ^{18}F-FDG findings, only 7 subjects showed definite or probable abnormal cardiac uptake of ^{68}Ga-DOTATATE.[50] However, there was 100% concordance between ^{18}F-FDG and ^{68}Ga-DOTATATE in positive thoracic nodal involvement, suggesting that the role of SSTR PET in cardiac sarcoidosis is less clear compared to the stronger evidence supporting its use in systemic manifestations.

Atherosclerotic disease has also been shown to correlate with SSTR tracer activity due to the presence of macrophages, potentially allowing for the early identification of vulnerable plaques in patients with risk factors.[51,52] By focusing on symptomatic carotid artery plaques in 10 patients planning to undergo carotid endarterectomy, Pedersen et al found that uptake of ^{64}Cu-DOTATATE was higher in symptomatic plaques compared to the contralateral side.[53] After analyzing gene expression in the plaque specimens, the investigators found that tracer activity was correlated with the presence of alternatively activated macrophages.

The advantage of using ^{68}Ga-DOTATATE rather than ^{18}F-FDG for atherosclerosis imaging was illustrated in a study that showed feasible coronary artery disease assessment in all 42 patients assessed with ^{68}Ga-DOTATATE, which was not possible with ^{18}F-FDG in most cases due to high adjacent myocardial activity.[54] SSTR PET has also

shown decreased inflammation in atheromatous plaques in response to medical intervention. Specifically, 22 subjects with type 2 diabetes were imaged with ^{68}Ga-DOTATATE PET/CT before and 3 months after initiating atorvastatin therapy, with a resulting 31% decrease in target-to-background ratio.[55] Similarly, ^{64}Cu-DOTATATE coronary uptake was found to decrease after 26 weeks of liraglutide therapy in 30 patients with type 2 diabetes.[56] Therefore, SSTR PET could help guide clinical decision making by identifying severity of disease and assessing efficacy of treatment.

Discussion

SSTR PET is currently being performed clinically for the primary purposes of staging and following NETs. Although the uptake mechanism of SSTR tracers is more specific than that of ^{18}F-FDG, many nontumor sources of uptake are still present. Familiarity with normal tissues which naturally express SSTR and common variations such as elevated uptake in the pancreatic uncinate process is necessary to avoid interpretive error. Normal splenic anatomy would be unlikely to confuse a reader, but the presence of an accessory spleen in an ambiguous or deceptive location could result in a diagnostic dilemma, warranting identification of splenic tissue with scintigraphic techniques or correlation with additional anatomic imaging.

Splenosis would be of particular concern in patients having undergone resection of NET, which is sometimes accompanied by splenectomy in cases with pancreatic involvement. Subtle morphological signs of splenosis such as the presence of smooth, round nodules combined with knowledge of the patient's treatment course may alert the reader to the possibility of splenosis rather than more concerning pathology such as peritoneal metastasis, additional testing would often be necessary given the lack of specificity of SSTR PET in such cases.

Similar to physiologic phenomena, benign and inflammatory disorders can hinder accurate interpretation if alternative explanations are not considered. For example, a focal ^{68}Ga-DOTATATE-avid lesion in the cavernous sinus may appear classic for meningioma, but in rare instances this may instead represent neurosarcoidosis. SSTR-positive mediastinal or hilar lymph nodes may represent either nodal metastases or reactive, infectious, or inflammatory lymph nodes depending on exposures and co-morbidities.

Although the distinctive vascular pattern and low-level uptake associated with atherosclerosis would be unlikely to pose a diagnostic challenge, the strong association between SSTR activity and presence of activated macrophages in atherosclerotic plaques suggests a possible role in directing therapy.

Conclusion

SSTR PET imaging has quickly revolutionized diagnosis, treatment, and surveillance of NETs and other SSTR-expressing tumors. A nuanced understanding of tracer behavior is necessary for precise image interpretation and optimal utilization.

References

1) Brazeau P, Vale W, Burgus R, et al Hypothalamic polypeptide that inhibits the secretion of immunoreactive pituitary growth hormone. *Science.* 1973;179(4068):77-79.

2) Shamsi BH, Chatoo M, Xu XK, Xu X, Chen XQ. Versatile functions of somatostatin and somatostatin receptors in the gastrointestinal system. *Front Endocrinol (Lausanne).* 2021;12:652363.

3) Ferone D, Pivonello R, Kwekkeboom DJ, et al Immunohistochemical localization and quantitative expression of somatostatin receptors in normal human spleen and thymus: Implications for the in vivo visualization during somatostatin receptor scintigraphy. *J Endocrinol Invest.* 2012;35(5):528-534.

4) Boy C, Heusner TA, Poeppel TD, et al 68Ga-DOTATOC PET/CT and somatostatin receptor (sst1-sst5) expression in normal human tissue: correlation of sst2 mRNA and SUVmax. *Eur J Nucl Med Mol Imaging.* 2011;38(7):1224-1236.

5) Taniyama Y, Suzuki T, Mikami Y, Moriya T, Satomi S, Sasano H. Systemic distribution of somatostatin receptor subtypes in human: an immunohistochemical study. *Endocr J.* 2005;52(5):605-611.

6) Reubi JC, Schar JC, Waser B, et al Affinity profiles for human somatostatin receptor subtypes SST1-SST5 of somatostatin radiotracers selected for scintigraphic and radiotherapeutic use. *Eur J Nucl Med.* 2000;27(3):273-282.

7) Krenning EP, Bakker WH, Kooij PP, et al Somatostatin receptor scintigraphy with indium-111-DTPA-D-Phe-1-octreotide in man: metabolism, dosimetry and comparison with iodine-123-Tyr-3-octreotide. *J Nucl Med.* 1992;33(5):652-658.

8) Hofman MS, Lau WF, Hicks RJ. Somatostatin receptor imaging with 68Ga DOTATATE PET/CT: clinical utility, normal patterns, pearls, and pitfalls in interpretation. *Radiographics.* 2015;35(2):500-516.

9) Cascini GL, Cuccurullo V, Tamburrini O, Rotondo A, Mansi L. Peptide imaging with somatostatin analogues: more than cancer probes. *Curr Radiopharm.* 2013;6(1):36-40.

10) Strosberg J, El-Haddad G, Wolin E, et al Phase 3 Trial of (177)Lu-Dotatate for Midgut Neuroendocrine Tumors. *N Engl J Med.* 2017;376(2):125-135.

11) Reubi JC, Waser B, Horisberger U, et al. In vitro autoradiographic and in vivo scintigraphic localization of somatostatin receptors in human lymphatic tissue. *Blood.* 1993;82(7):2143-2151.

12) hastry M, Kayani I, Wild D, et al Distribution pattern of 68Ga-DOTATATE in disease-free patients. *Nucl Med Commun.* 2010;31(12):1025-1032.

13) Sandstrom M, Velikyan I, Garske-Roman U, et al Comparative biodistribution and radiation dosimetry of 68Ga-DOTATOC and 68Ga-DOTATATE in patients with neuroendocrine tumors. *J Nucl Med.* 2013;54(10):1755-1759.

14) Wild D, Bomanji JB, Benkert P, et al Comparison of 68Ga-DOTANOC and 68Ga-DOTATATE PET/CT within patients with gastroenteropancreatic neuroendocrine tumors. *J Nucl Med.* 2013;54(3):364-372.

15) Conti M, Eriksson L. Physics of pure and non-pure positron emitters for PET: a review and a discussion. *EJNMMI Phys.* 2016;3(1):8.

16) Johnbeck CB, Knigge U, Loft A, et al. Head-to-head comparison of (64)Cu-DOTATATE and (68)Ga-DOTATOC PET/CT: a prospective study of 59 patients with neuroendocrine tumors. *J Nucl Med.* 2017;58(3):451-457.

17) Tabacchi E, Fortunati E, Argalia G, et al. [68Ga]Ga-DOTANOC Uptake at pancreatic head/uncinate process: is it a persistent diagnostic pitfall over time? *Cancers (Basel).* 2022;14(14).

18) Mapelli P, Tam HH, Sharma R, Aboagye EO, Al-Nahhas A. Frequency and significance of physiological versus pathological uptake of 68Ga-DOTATATE in the pancreas: validation with morphological imaging. *Nucl Med Commun.* 2014;35(6):613-619.

19) Lakhotia R, Jhawar S, Malayeri AA, Millo C, Del Rivero J, Ahlman MA. Incidental 68Ga-DOTATATE uptake in the pancreatic head: A case report and a unique opportunity to improve clinical care. *Medicine (Baltimore).* 2020;99(22):e20197.

20) Brabander T, Teunissen J, Kwekkeboom D. Physiological uptake in the pancreatic head on somatostatin receptor scintigraphy using [111In-DTPA]octreotide: incidence and mechanism. *Clin Nucl Med.* 2017;42(1):15-19.

21) Ait Boudaoud A, Verges B, Petit JM, Tatulashvili S, Cochet A, Humbert O. Uptake in the pancreatic uncinate process on the 111In-octreotide scintigraphy: How to distinguish physiological from pathological uptake? *Nucl Med Commun.* 2017;38(9):737-743.

22) Krausz Y, Rubinstein R, Appelbaum L, et al. Ga-68 DOTA-NOC uptake in the pancreas: pathological and physiological patterns. *Clin Nucl Med.* 2012;37(1):57-62.

23) Jacobsson H, Larsson P, Jonsson C, Jussing E, Gryback P. Normal uptake of 68Ga-DOTA-TOC by the pancreas uncinate process mimicking malignancy at somatostatin receptor PET. *Clin Nucl Med.* 2012;37(4):362-365.

24) Kunikowska J, Krolicki L, Pawlak D, Zerizer I, Mikolajczak R. Semiquantitative analysis and characterization of physiological biodistribution of (68)Ga-DOTA-TATE PET/CT. *Clin Nucl Med.* 2012;37(11):1052-1057.

25) Castellucci P, Pou Ucha J, Fuccio C, et al Incidence of increased 68Ga-DOTANOC uptake in the pancreatic head in a large series of extrapancreatic NET patients studied with sequential PET/CT. *J Nucl Med.* 2011;52(6):886-890.

26) Al-Ibraheem A, Bundschuh RA, Notni J, et al. Focal uptake of 68Ga-DOTATOC in the pancreas: pathological or physiological correlate in patients with neuroendocrine tumours? *Eur J Nucl Med Mol Imaging.* 2011;38(11):2005-2013.

27) Wang X, Zielinski MC, Misawa R, et al Quantitative analysis of pancreatic polypeptide cell distribution in the human pancreas. *PLoS One.* 2013;8(1):e55501.

28) Kroiss A, Putzer D, Decristoforo C, et al. 68Ga-DOTA-TOC uptake in neuroendocrine tumour and healthy tissue: differentiation of physiological uptake and pathological processes in PET/CT. *Eur J Nucl Med Mol Imaging.* 2013;40(4):514-523.

29) Delbeke D, Newman G, Deppen S, et al. 68Ga-DOTATATE: Significance of uptake in the tail of the pancreas in patients without lesions. *Clin Nucl Med.* 2019;44(11):851-854.

30) Pang Y, Meng T, Shang Q, Chen Z, Chen H. 68Ga-Exendin-4 PET/CT differentiates insulinoma from accessory spleen in a patient presenting indeterminate MRI and 68Ga-DOTATATE PET/CT findings. *Clin Nucl Med.* 2022;47(3):265-267.

31) Lancellotti F, Sacco L, Cerasari S, et al Intrapancreatic accessory spleen false positive to 68Ga-Dotatoc: case report and literature review. *World J Surg Oncol.* 2019;17(1):117.

32) Bhure U, Metzger J, Keller FA, et al Intrapancreatic Accessory Spleen Mimicking Neuroendocrine Tumor on 68Ga-DOTATATE PET/CT. *Clin Nucl Med.* 2015;40(9):744-745.

33) Sachawars E, Lin M, Sidhom GE. Jumping the gun: traumatic splenosis mimicking 68-gallium-dotatate avid neuroendocrine tumour. *ANZ J Surg.* 2020;90(12):E217-E218.

34) Gezer E, Cetinarslan B, Karakaya D, et al. Differentiation of insulinoma from accessory spleen by (99m)Tc-labelled heat-denaturated red blood cell scintigraphy: case report. *BMC Endocr Disord.* 2021;21(1):6.

35) Fastrez M, Artigas C, Sirtaine N, et al. Value of the (68)Ga-DOTATATE PET-CT in the diagnosis of endometriosis. A pilot study. *Eur J Obstet Gynecol Reprod Biol.* 2017;212:69-74.

36) Corovic A, Wall C, Nus M, et al. Somatostatin receptor PET/MR imaging of inflammation in patients with large vessel vasculitis and atherosclerosis. *J Am Coll Cardiol.* 2023;81(4):336-354.

37) Tarkin JM, Wall C, Gopalan D, et al. Novel approach to imaging active Takayasu arteritis using somatostatin receptor positron emission tomography/magnetic resonance imaging. *Circ Cardiovasc Imaging.* 2020;13(6):e010389.

38) Ambrosini V, Zompatori M, De Luca F, et al. 68Ga-DOTANOC PET/CT allows somatostatin receptor imaging in idiopathic pulmonary fibrosis: preliminary results. *J Nucl Med.* 2010;51(12):1950-1955.

39) Naftalin CM, Leek F, Hallinan J, et al. Comparison of 68Ga-DOTANOC with 18F-FDG using PET/MRI imaging in patients with pulmonary tuberculosis. *Sci Rep.* 2020;10(1):14236.

40) Nobashi T, Nakamoto Y, Kubo T, et al. The utility of PET/CT with (68)Ga-DOTATOC in sarcoidosis: comparison with (67)Ga-scintigraphy. *Ann Nucl Med.* 2016;30(8):544-552.

41) Sharma S, Singh AD, Sharma SK, Tripathi M, Das CJ, Kumar R. Gallium-68 DOTA-NOC PET/CT as an alternate predictor of disease activity in sarcoidosis. *Nucl Med Commun.* 2018;39(8):768-778.

42) Unterrainer M, Ruf V, Ilhan H, et al. Teaching neuroImages: advanced imaging of neurosarcoidosis with (68)Ga-DOTATATE PET/CT. *Neurology.* 2019;92(21):e2512-e2513.

43) Vachatimanont S, Kunawudhi A, Promteangtrong C, Chotipanich C. Benefits of [(68)Ga]-DOTATATE PET-CT comparable to [(18)F]-FDG in patient with suspected cardiac sarcoidosis. *J Nucl Cardiol.* 2022;29(1):381-383.

44) Imperiale A, Poindron V, Martinez M, Ohlmann P, Schindler TH, El Ghannudi S. 68Ga-DOTATOC PET for treatment efficacy evaluation of cardiac sarcoidosis. *Clin Nucl Med.* 2020;45(9):e416-e418.

45) Pizarro C, Kluenker F, Dabir D, et al. Cardiovascular magnetic resonance imaging and clinical performance of somatostatin receptor positron emission tomography in cardiac sarcoidosis. *ESC Heart Fail.* 2018;5(2):249-261.

46) Passah A, Kaushik P, Patel C, Parakh N. Gallium-68 DOTANOC scan in a patient with suspected cardiac sarcoidosis. *J Nucl Cardiol.* 2018;25(6):2177-2178.

47) Lapa C, Reiter T, Kircher M, et al. Somatostatin receptor based PET/CT in patients with the suspicion of cardiac sarcoidosis: an initial comparison to cardiac MRI. *Oncotarget.* 2016;7(47):77807-77814.

48) Reiter T, Werner RA, Bauer WR, Lapa C. Detection of cardiac sarcoidosis by macrophage-directed somatostatin receptor 2-based positron emission tomography/computed tomography. *Eur Heart J.* 2015;36(35):2404.

49) Gormsen LC, Haraldsen A, Kramer S, Dias AH, Kim WY, Borghammer P. A dual tracer (68) Ga-DOTANOC PET/CT and (18)F-FDG PET/CT pilot study for detection of cardiac sarcoidosis. *EJNMMI Res.* 2016;6(1):52.

50) Bravo PE, Bajaj N, Padera RF, et al Feasibility of somatostatin receptor-targeted imaging for detection of myocardial inflammation: A pilot study. *J Nucl Cardiol.* 2021;28(3):1089-1099.

51) Jensen JK, Madsen JS, Jensen MEK, Kjaer A, Ripa RS. [(64)Cu]Cu-DOTATATE PET metrics in the investigation of atherosclerotic inflammation in humans. *J Nucl Cardiol.* 2023;30(3):986-1000.

52) Lee R, Kim J, Paeng JC, et al. Measurement of (68)Ga-DOTATOC uptake in the thoracic aorta and its correlation with cardiovascular risk. *Nucl Med Mol Imaging.* 2018;52(4):279-286.

53) Pedersen SF, Sandholt BV, Keller SH, et al. 64Cu-DOTATATE PET/MRI for detection of activated macrophages in carotid atherosclerotic plaques: studies in patients undergoing endarterectomy. *Arterioscler Thromb Vasc Biol.* 2015;35(7):1696-1703.

54) Tarkin JM, Joshi FR, Evans NR, et al. Detection of atherosclerotic inflammation by (68) Ga-DOTATATE PET compared to [(18)F]FDG PET imaging. *J Am Coll Cardiol.* 2017;69(14):1774-1791.

55) Oostveen RF, Kaiser Y, Stahle MR, et al. Atorvastatin lowers (68)Ga-DOTATATE uptake in coronary arteries, bone marrow and spleen in individuals with type 2 diabetes. *Diabetologia.* 2023.

56) Jensen JK, Zobel EH, von Scholten BJ, et al. Effect of 26 weeks of liraglutide treatment on coronary artery inflammation in type 2 diabetes quantified by [(64)Cu]Cu-DOTATATE PET/CT: results from the LIRAFLAME trial. *Front Endocrinol (Lausanne).* 2021;12:790405.

Vasculitis in the Emergency Room: The Pivotal Role of Imaging in Diagnosis and Management

Sherif B. Elsherif, MD; Manuel Menendez, MD; Carlos Gonzalez Baerga, MD; Matthew Montanarella, DO; Mayur Virarkar, MD;, Daniel Karolyi, MD; Dheeraj Reddy Gopireddy, MD.

Abstract

Vasculitis encompasses a range of conditions characterized by blood vessel inflammation with diverse clinical presentations. Classified by vessel size, vasculitis includes large-vessel vasculitis such as giant cell arteritis, medium-vessel vasculitis like Kawasaki disease, and small-vessel vasculitis like granulomatosis with polyangiitis. Misdiagnosis can have severe consequences such as heart attack and stroke. While biopsy remains the diagnostic gold standard, imaging plays a crucial role given the challenge of tissue sampling. Imaging findings combined with clinical evidence are essential for accurate diagnosis and treatment. This article explores various vasculitis types and their clinical and imaging findings in emergency settings.

Keywords: Vasculitis, Large vessel vasculitides, Giant cell arteritis, Takayasu Arteritis, Kawasaki Disease, Granulomatosis with polyangiitis

Vasculitis, encompassing a broad spectrum of disorders, is a beacon of medical intrigue, primarily characterized by inflammation within the vessels that nourish our organs [1] Vasculitis can be primary or secondary, depending on etiology. According to the 2012 revised Chapel Hill Consensus Conference Nomenclature of Vasculitides, it is intricately categorized by the size of the involved vessels into large-vessel vasculitis (eg, giant cell arteritis, Takayasu arteritis), medium-vessel vasculitis (eg, Kawasaki disease, polyarteritis nodosa), or small-vessel vasculitis (eg, granulomatosis with Polyangiitis, microscopic polyangiitis, eosinophilic granulomatosis with polyangiitis, Henoch-Schonlein purpura, systemic lupus erythematosus, rheumatoid vasculitis, Behçet syndrome) (Figure 1).[2,3] This classification framework is instrumental in comprehensively characterizing the diverse imaging manifestations of vasculitis, thus facilitating accurate diagnosis and timely management.

For many vasculitis patients, their initial presentation occurs in the emergency department. Misdiagnosis and delays in achieving diagnosis can lead to a risk of heightened mortality and morbidities such as myocardial infarction, stroke, mesenteric ischemia, or ruptured aneurysms. The clinical presentation of vasculitis often exhibits similarities to other medical conditions, which can contribute to misdiagnosis (Table 1). The differential diagnosis must consider the possibility of

Affiliations: Department of Radiology, The University of Florida College of Medicine, Jacksonville, Florida (Drs Elsherif, Menendez, Baerga, Montanarella, Virarkar, Gopireddy); Department of Radiology, Virginia Tech Carilion School of Medicine, Roanoke, Virginia (Dr Karolyi).
Disclosures: The authors declare no conflicts of interest or funding with respect to this review article.
Prior publication/presentation: Gopireddy D, Venturella S, Ly N, Agarwal R. Suspecting and diagnosing systemic vasculitis in emergency room - A multimodality pictorial review. The Radiological Society of North America (RSNA) Scientific Exhibition and Annual Meeting. 2010, Chicago, Illinois.

Figure 1. Flowchart of vasculitis classification.

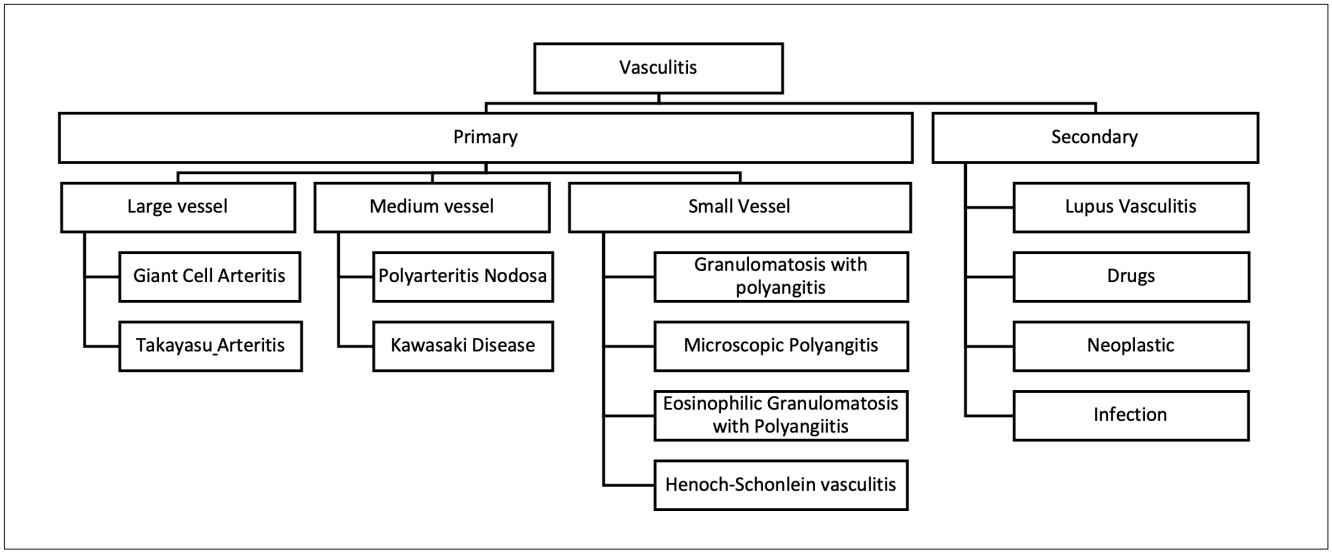

Table 1. Common clinical and laboratory presentation of various vasculitides.

VASCULITIS	CLINICAL FINDINGS	LABORATORY FINDINGS
Giant Cell	Young or middle-aged, especially Asian and female Claudication of upper extremities with absent pulses	Elevated ESR/CRP
Takayasu	Above 50 years of age New headaches with visual disturbances Symptoms of polymyalgia rheumatica Jaw claudication	Elevated ESR/CRP
Polyarteritis Nodosa	Renal failure Gastrointestinal bleeding, nausea Neuropathy and skin lesions	Elevated ESR/CRP Perinuclear-ANCA Positive Hepatitis B serology
Kawasaki	Conjunctivitis (90%) Shock syndrome Rash with Polyarthritis Edema and erythema of extremities	Elevated ESR/CRP Leukocytosis
Granulomatosis with Polyangitis	Oral, nasal, and sinus inflammation Hemoptysis, chest pain, and stridor Renal failure with hematuria Scleritis, uveitis, conjunctivitis	Positive C-ANCA / Anti-PR-3 (85-90% sensitivity)
Microscopic Polyangitis	Pulmonary hemorrhage Renal failure Skin lesions	Positive P-ANCA/ Anti-MPO (35-70% sensitivity)
Eosinophilic Granulomatosis with Polyangiitis	Late-onset Asthma Sinusitis Neuropathy	10% Eosinophilia P-ANCA/ Anti-MPO positive (35-70% sensitivity)
Henoch-Schonlein purpura	Children 3-10 years Skin rash, arthritis, hematuria, and abdominal pain with bleeding	Elevated serum IgA levels in 50 to 70%
Systemic Lupus Erythematosus	Malar rash, discoid rash, photosensitivity, oral ulcers arthritis, serositis, and renal failure, neurologic	Positive ANA (100% sensitivity) Positive Anti-Smith and Anti-DNA

ESR, Erythrocyte sedimentation rate; CRP, C-reactive protein; ANCA, Antineutrophilic cytoplasmic antibody; MPO, Myeloperoxidase.

Figure 2. An adult patient with left arm claudication and chest pain. Angiogram of the aortic arch (A) shows focal stenosis of the left subclavian artery (white arrow). A sagittal reformatted chest CTA image (B) in another patient with chest pain shows multiple pseudoaneurysms of the descending thoracic aorta (white arrowheads). Pathology confirmed giant cell arteritis in both patients. An axial CT image of the neck (C) in a different patient presenting with tender right neck swelling displays hypoattenuating mural thickening of the right common carotid artery (white arrowhead), accompanied by surrounding soft tissue stranding. Corresponding increased metabolic activity is evident in the axial PET/CT image (D). Subsequent confirmation revealed giant cell arteritis in this patient as well.

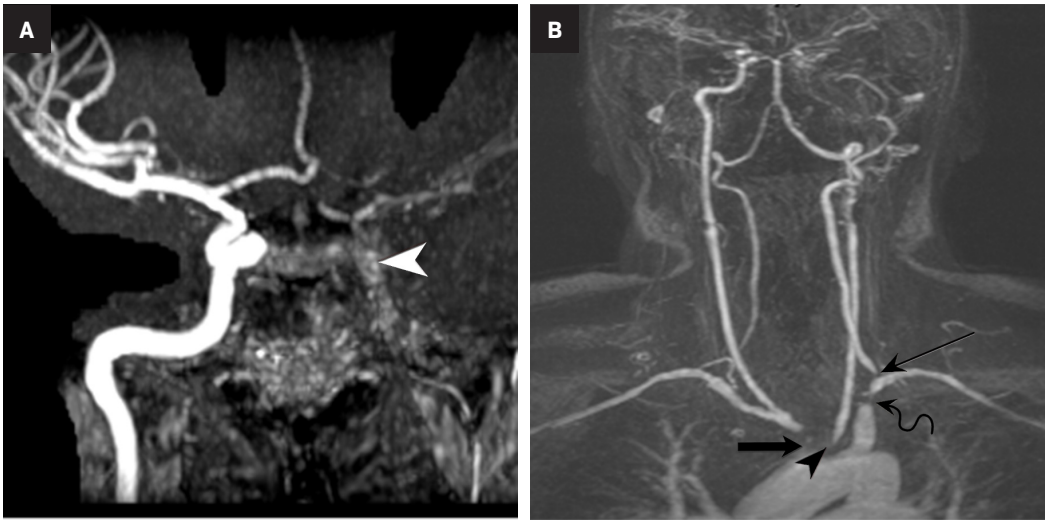

Figure 3. An adult with dizziness and stroke symptoms. Coronal head MRA (A) shows complete occlusion of distal cervical and intracranial left internal carotid artery (white arrowhead). Coronal neck MRA (B) demonstrates multifocal stenoses involving the right brachiocephalic artery origin (thick black arrow), the left common carotid artery origin (black arrowhead), the proximal left subclavian artery (curved black arrow), and the left vertebral artery origin (thin black arrow). Pathology confirmed Takayasu arteritis.

infections, coagulopathies, and drug toxicities.[1,4] Although biopsy is the gold standard of diagnosis, tissue sampling can be challenging, and biopsy may be negative in up to 42% of cases.[5] In this intricate maze, radiologists emerge as invaluable navigators, leveraging imaging to elucidate the causes of vasculitis. In addition, it is essential to image these patients before initiation of therapy, since the sensitivity of imaging notably decreases a few days after the initiation of corticosteroid therapy.[6]

A multidisciplinary approach that harnesses radiological and clinical evidence is essential to enhance diagnostic accuracy, assess disease extent, and enable better treatment selection and monitoring. [7] This article endeavors to traverse the intricate nature of vasculitis, spotlighting the confluence of clinical presentations and imaging findings, especially in the emergency department.

Large-vessel Vasculitis

Giant Cell Arteritis

Giant cell arteritis (GCA) is an autoimmune chronic granulomatous inflammation of the large vessels that stands as the most common inflammatory vasculitides.[8] It often occurs in people over 50 years of age, with a predilection for those of northern European descent.[7] The primary pathology in GCA is transmural inflammation of the vessels, causing luminal occlusion, aneurysm formation, dissection, hemorrhage, and rupture [7], most commonly involving the carotid arteries and, rarely, the central pulmonary arteries.[9] Key clinical presentations in the emergency setting that should trigger a heightened index of suspicion for GCA include the main clinical features outlined in the 2022 American College of Rheumatology

(ACR)-European Alliance of Associations for Rheumatology (EULAR) Classification Criteria such as sudden monocular visual disturbances, new onset headache, jaw claudication, limb claudication, asymmetric blood pressure, or vascular bruits.[8,10-12] Polymyalgia rheumatica is the most common extracranial manifestation in GCA, seen in 45-50% of patients who classically present with severe pain and stiffness of the shoulders, neck, and less frequently the pelvic girdle.[5,8] Suspicious clinical presentation and elevated inflammatory markers should prompt a thorough diagnostic workup for GCA.

Doppler ultrasound (US) of the temporal artery reveals noncompressible hypoechoic circumferential vessel wall thickening, known as the "Halo sign." Computed tomography angiography (CTA) and magnetic resonance angiography (MRA) assess large-vessel involvement, demonstrating vessel wall thickening, arterial stenosis, aneurysms, or dissections (Figure 2). Delayed CTA images can help delineate vessel wall enhancement whereas noncontrast images differentiate true wall thickening from intramural hematoma, seen in acute aortic syndrome.[8] In addition, magnetic resonance imaging (MRI) can accurately assess large-vessel involvement as an increased signal on fat-suppressed T2 images and late enhancement in delayed post-contrast imaging. Cardiac MRI and echocardiography can also assess valvular involvement, most commonly aortic insufficiency, coronary artery disease or, less commonly, myocarditis and pericarditis.[7,13] Steady-state free precession (SSFP) cine sequence in cardiac MRI helps to assess the cardiac function and valvular involvement while delayed enhancement images

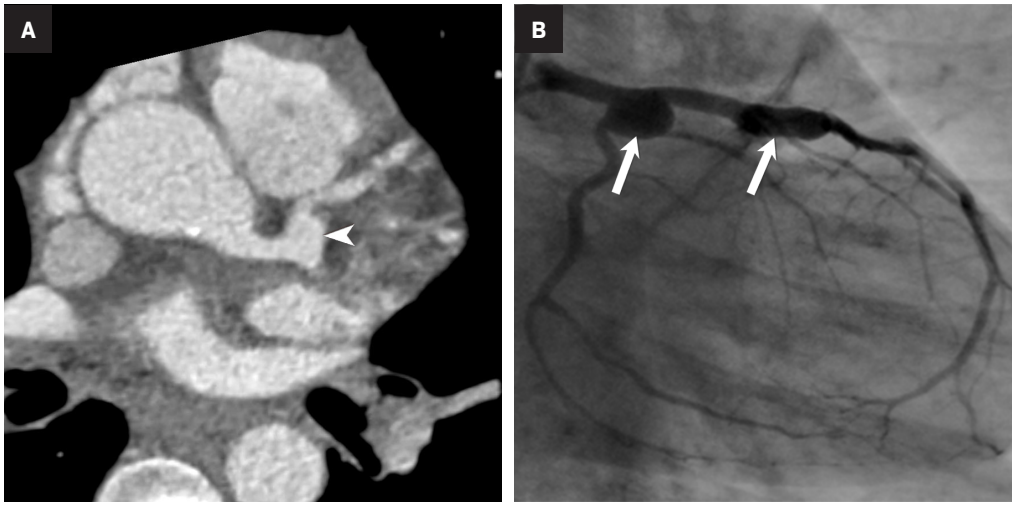

Figure 4. Axial coronary CTA in a child with chest pain (A) shows a 9 mm coronary artery aneurysm (white arrowhead) at the bifurcation of the left anterior descending and circumflex coronary arteries with no thrombosis or stenosis. A coronary angiogram of the left main coronary artery in another child presenting with chest pain (B) shows a saccular aneurysm at the left main coronary artery bifurcation and fusiform aneurysm of the proximal left anterior descending artery (white arrows). Both cases were diagnosed as Kawasaki disease.

accurately depict fibrosis and inflammation.[7] Temporal artery biopsy is the standard but invasive diagnostic test. [11]

Takayasu Arteritis

Takayasu arteritis (TAK) is a rare granulomatous large-vessel vasculitis affecting 1.11 per million people yearly. It commonly affects those younger than 50 years old, distinguishing it from GCA.[6,14] TAK tends to cause panarterial inflammation, leading to luminal narrowing and occlusion,[7] and can present with various clinical manifestations depending on the affected vessels, similarly to GCA.[15]

Early-stage TAK may present with nonspecific symptoms; as result, it is often misdiagnosed, emphasizing the importance of a high clinical suspicion index and comprehensive imaging studies. Alarming clinical presentation in the emergency department for TAK includes one of the key clinical features in the 2022 ACR-EULAR Classification Criteria such as angina, claudication, vascular bruit or systolic blood pressure difference in arms ≥ 20 mm Hg.[12]

Noninvasive imaging modalities are the current standard for diagnosing and assessing disease extent. Ultrasound demonstrates intima-media thickness greater than 1mm and vascular stenosis in TAK involving the carotid and subclavian arteries. However, ultrasound is limited in assessing the aorta or major aortic branches, those most commonly involved in TAK.[16] CTA and MRA are the diagnostic imaging modalities primarily used to diagnose wall thickening (low attenuation ring in delayed phase) and luminal stenosis (Figure 3).[17] Using the fat-suppressed black-blood technique during contrast-enhanced MRI scans enables the identification of early inflammatory vascular changes such as mural thickening, potentially revealing reversible stages, even before there is an appreciable wall thickening.[6,13] Like GCA, cardiac MRI and echocardiography can assess cardiac involvement.[7] PET/CT can help determine disease activity. Conventional angiography used to be the gold standard for evaluating affected vessels; however, it is invasive and cannot assess vascular wall involvement, which occurs earlier in the disease pathogenesis.[15,18]

Medium-vessel Vasculitis

Kawasaki Vasculitis

Kawasaki disease (KD) is a pediatric, medium-vessel vasculitis prevalent in children under five years old. The incidence of KD is notably higher in Japan, with 265 cases per 100,000, in contrast to the 20-25 cases per 100,000 in the United States.[7,19,20] Kawasaki disease is believed to stem from abnormal immune responses. The classic presentation includes fever persisting for at least five days and the presence of at least four of the following criteria: bilateral nonexudative conjunctivitis, oropharyngeal mucosal changes, erythema and desquamation of hands and feet, non-vesicular truncal rash, and cervical lymphadenopathy.[7,19,20]

Kawasaki disease is a major contributor to acquired pediatric cardiovascular diseases, with the most common complication being coronary artery aneurysm, occurring in 15-25% of untreated cases and posing a potential risk of thrombosis and myocardial infarction.[21] Additional possible complications include pericarditis, myocarditis, valvular regurgitation, and aneurysmal formation in noncoronary arteries.

Echocardiography is the preferred diagnostic modality to detect coronary aneurysms, owing to its ability to reveal accular or fusiform arterial dilatation. In chronic phases, echocardiography depicts mural thrombosis of the aneurysm as hyperechogenicity and luminal stenosis.[19]

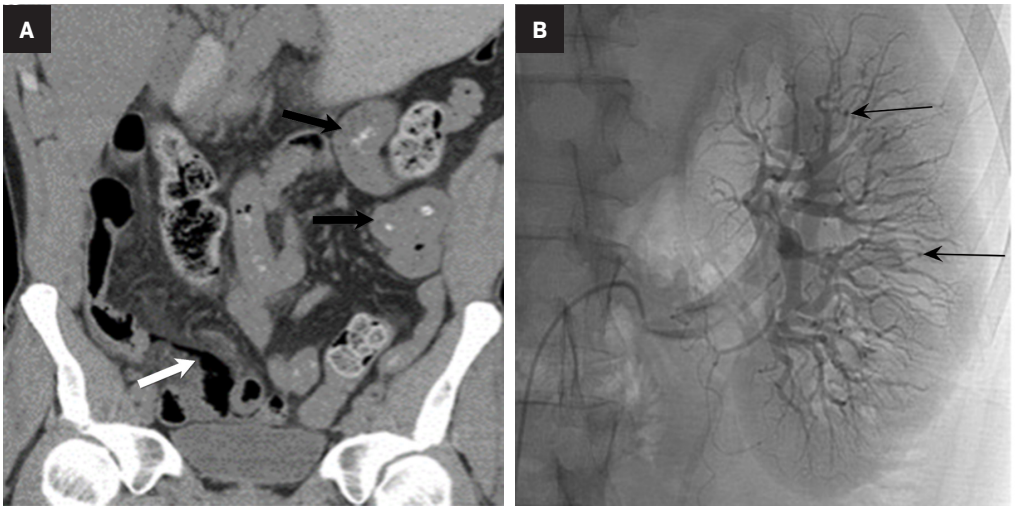

Figure 5. Elderly patient with abdominal pain. Coronal (A) noncontrast abdominal CT image shows multifocal bowel-wall thickening involving the small bowel (black arrows) and cecum (black arrowhead) with free air in the right lower abdomen quadrant (white arrow) indicating bowel perforation. Selective angiogram of the renal artery (B) shows multiple distal small saccular aneurysms (thin black arrows). Pathology confirmed the diagnosis of polyarteritis nodosa.

Figure 6. A patient with massive hemoptysis, eye pain, and blurry vision. Axial chest CT image (A) shows bilateral thick wall cavitating masses (black arrows). Axial postcontrast CT image of the orbit (B) shows thickening of the sclera and marked enhancement (black arrowheads), secondary to episcleritis. Pathology confirmed the diagnosis of granulomatosis with polyangiitis.

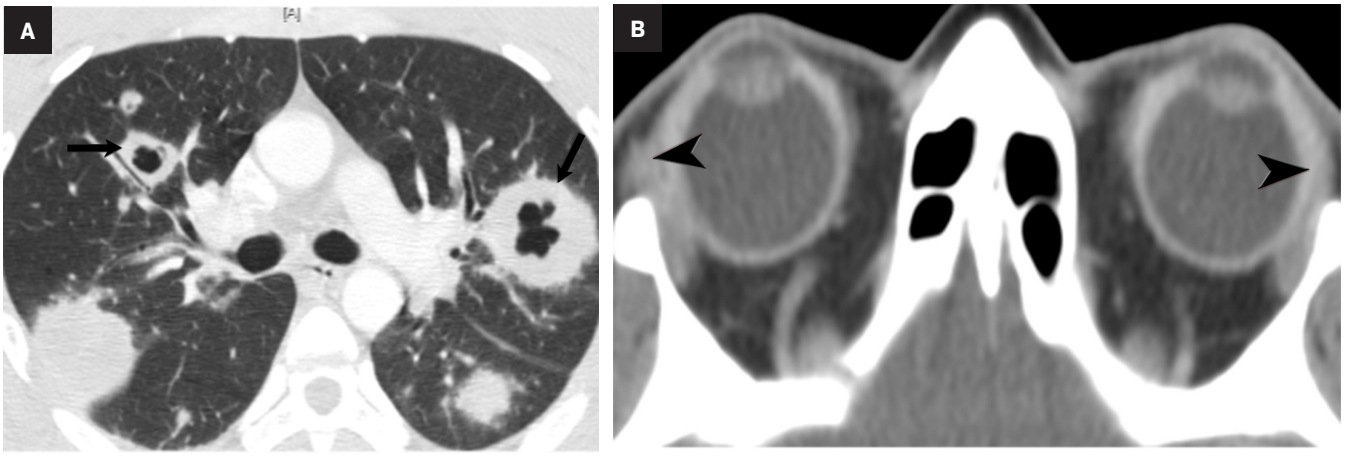

Coronary CTA is a rapid modality that can accurately diagnose coronary artery stenosis in the emergency setting with negative predictive value up to 99%. However, optimal imaging techniques should be applied to lower radiation doses given most of these patients are pediatrics.[21] CTA can also evaluate coronary anomalies, particularly those involving the distal arteries (Figure 4).

MRI is valuable for assessing cardiac function and myocardial viability using a three-dimensional SSFP sequence or non-enhanced black-blood MRA to assess coronary arteries involvement. [7,21,22] Patients can also develop other presentations with nonspecific imaging findings, including pseudo-obstructions, hepatitis, pancreatitis, arthritis, and myositis.[19]

Polyarteritis Nodosa

Polyarteritis nodosa (PAN) is a systemic necrotizing vasculitis that may be triggered either idiopathically or by viral infection such as hepatitis or human immunodeficiency virus (HIV). Compared with Kawasaki disease, PAN typically presents with subacute onset and is more commonly observed in the adult population, particularly among Alaskan and Kuwaiti natives.[7]
The diagnosis of systemic PAN is established by the presence of three of the following: significant weight loss, livedo reticularis, testicular pain, myalgia, neuropathy, hypertension, elevated renal function, hepatitis B infection, angiographic abnormalities demonstrating aneurysms or occlusions and biopsy-proven vasculitis.

A hallmark of PAN is multiple aneurysms, most commonly in the kidneys (80-90%), followed by the gastrointestinal tract (50-70%), liver (50-60%), coronary arteries (50%), spleen (45%) and pancreas

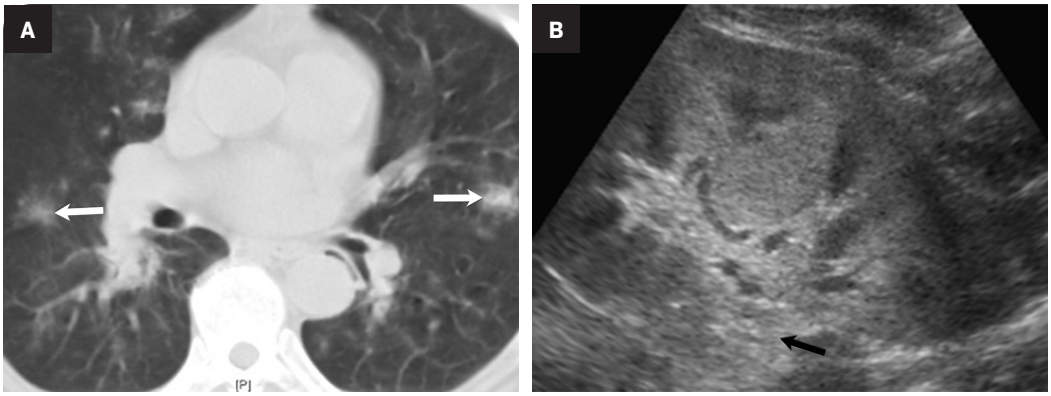

Figure 7. A patient with hemoptysis and rapidly progressing renal failure. Axial chest CT (A) demonstrates patchy ground-glass opacities in both lungs (white arrows) secondary to pulmonary hemorrhage. Greyscale abdominal US image (B) shows an echogenic kidney (black arrow) in keeping with medical renal disease. The patient was later diagnosed with microscopic polyangiitis.

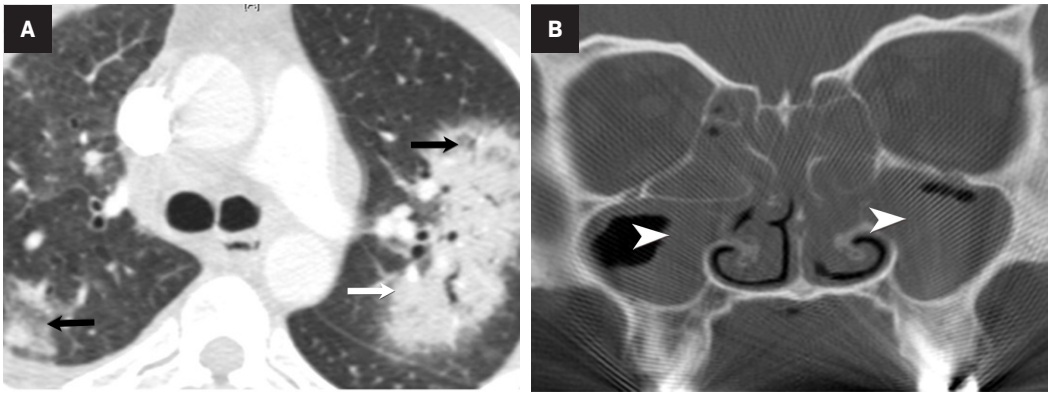

Figure 8. A young patient with asthma and eosinophilia. Axial chest CT image (A) shows consolidative (white arrow) and ground-glass (black arrows) opacities in both lungs. Coronal reformatted CT image of the paranasal sinuses in the bone window (B) shows opacification of bilateral maxillary sinuses, consistent with sinusitis. The patient was later diagnosed with eosinophilic granulomatosis with polyangiitis.

(25-35%). Computed tomography (CT) and MRI vascular findings include segmental mural thickening, submucosal edema, abnormal hyperenhancement with a striated pattern, arterial stenosis, and visceral aneurysms (Figure 5).[23,24] Imaging can also reveal renal or bowel infarcts, perforation, hemorrhage, or intramuscular hematoma.[25,26] The diagnosis often relies on angiographic findings of aneurysms up to 1 cm in diameter with a pathological correlation of fibrinoid necrosis.[7,25]

Small-vessel Vasculitis

Granulomatosis with Polyangiitis

Granulomatosis with polyangiitis (GPA), formerly known as Wegner's granulomatosis, is an angiogenic multisystem necrotizing disease characterized by a triad of upper and lower respiratory tract granulomas, vasculitis, and renal involvement (necrotizing crescentic glomerulonephritis). GPA primarily affects adults between the ages of 64 and 75, with an incidence of 3 cases per million people in the United States. Diagnosis requires at least 2 of the following: urinary sediment containing red blood cell casts, abnormal chest radiograph, presence of oral ulcers or nasal discharge, and granulomatous inflammation on biopsy.[27-29]

Magnetic resonance imaging reveals increased T2 signal and postcontrast enhancement in early disease and low T2 nonenhancing fibrosis in late-stage disease, which can manifest as enophthalmos and subglottic or tracheal stenosis.[27,30] About 25% of GPA patients present with sinonasal disease with nonspecific maxillary mucosal thickening on CT. Late-stage disease may show osseous destruction involving the nasal septum, turbinates, and anterior ethmoid region, potentially leading to a saddle-nose deformity, a hallmark of GPA.[27] Pulmonary findings in CT are nonspecific they include nodules, consolidations, and ground-glass opacities. [28] Renal involvement appears on ultrasound as enlarged echogenic kidneys in early stage- and shrunken kidneys in late-stage disease.

Meanwhile, MRI shows wedge-shaped T2 hyperintensity and hypoenhancement in nephritis or ischemia (Figure 6).[23] Gastrointestinal manifestations encompass segmental hyperenhancing bowel-wall thickening with mesenteric engorgement and, less commonly, granulomatous colitis, granulomatous pancreatic mass, splenic infarct or hemorrhage, and gastritis.[23]

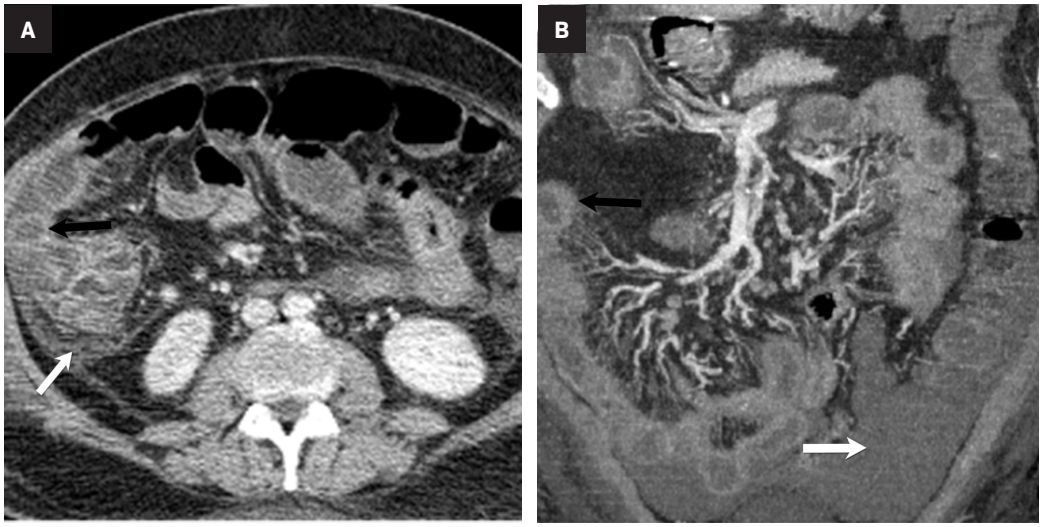

Figure 9. A patient with lower gastrointestingal bleeding and lower extremity rash. Axial (A) and coronal (B) contrast-enhanced abdominal CT images show thickening of the cecum and ascending colon with mucosal hyperenhancement (black arrows) and moderate abdominal ascites (white arrows). The patient was later diagnosed with Henoch-Schonlein purpura.

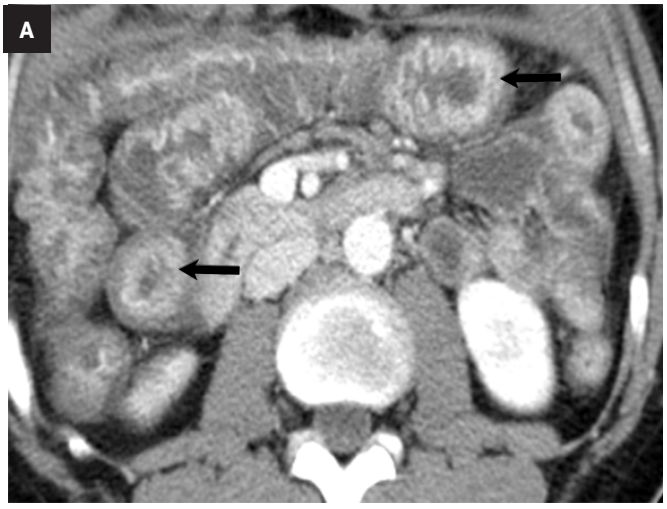

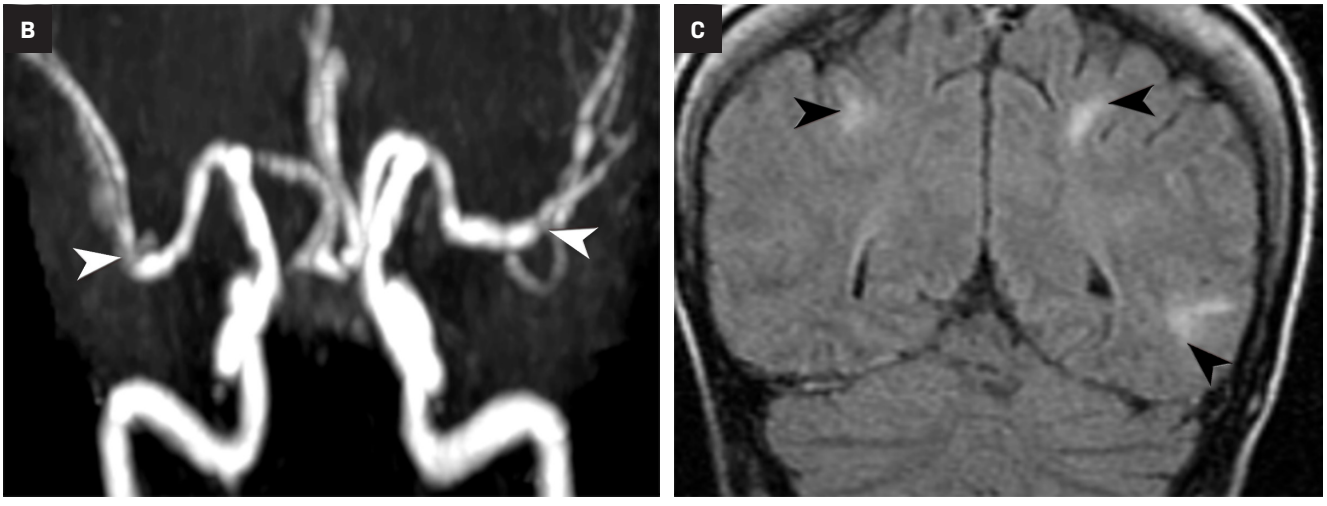

Figure 10. A child with abdominal pain and neurological symptoms. Axial contrast-enhanced abdominal CT image (A) shows diffuse small-bowel wall thickening (black arrow), resulting in Target appearance. Magnetic resonance angiography of the cerebral vessels (B) shows multifocal stenoses in both MCAs (white arrowheads). The patient was later diagnosed with systemic lupus vasculitis. Coronal FLAIR MRI of the brain (C) shows multifocal subcortical white matter lesions (black arrowheads).

Microscopic Polyangiitis

Microscopic polyangiitis (MPA) is a necrotizing vasculitide, like GPA, with predominance in Asian countries such as China and Japan.[31] Clinical and imaging presentation can be variable depending on the affected organs and include kidney failure, hemoptysis, dyspnea, pleuritic pain, and constitutional symptoms (Figure 7).[32] Upper airway complications are less common in MPA compared to GPA. [33] The 2020 ACR-EULAR Classification Criteria for small vessel vasculitis include ANCA subtype as a major criterion between GPA and MPA. [12]

Patients with pulmonary symptoms suspected of having MPA should undergo chest CT, which can demonstrate nodules with or without cavitation, alveolar opacities, or pleural lesions. Non-contrast CT is the preferred imaging study, as these patients may also have renal impairment.[31]

Eosinophilic Granulomatosis With Polyangiitis

Eosinophilic granulomatosis with polyangiitis (EGPA), previously known as Churg-Strauss syndrome, is an eosinophil-rich multisystem necrotizing granulomatous inflammation. The typical clinical presentation typically includes asthma, eosinophilia, palpable purpura, and a positive PR3-ANCA test found in 50% of cases. EGPA commonly involves the lungs, heart, gastrointestinal tract, spleen, and kidneys (Figure 8).

Cardiac involvement carries an unfavorable prognosis and is an independent predictor of mortality. Cardiac MR can assess the extent of cardiac involvement, including cardiomyopathy (30%, with late gadolinium enhancement), pericardial effusion (22%), and valvular disease (mainly affecting the mitral valve).[3,7]

Henoch-Schonlein Vasculitis

Henoch-Schonlein vasculitis, also known as IgA vasculitis, is an IgA-mediated immune vasculitis that primarily affects the kidneys, gastrointestinal tract, skin, lungs, joints, and central nervous system. The condition is commonly observed in pediatric males and typically presents with either an upper respiratory or gastrointestinal infection.[34] Diagnostic criteria include purpura/petechiae with lower limb predominance and at least one of the following: arthritis, diffuse abdominal pain, renal involvement, or histopathology revealing IgA deposits or leukocytoplastic vasculitis.[35]

The gastrointestinal system, commonly the ileum, is involved in 60% of patients, with radiography showing smooth fold thickening, known as thumbprinting or irregular wall thickening.[36] CT features are nonspecific and may include bowel-wall thickening, mural hyperdensity in noncontrast images, indicating submucosal hemorrhage, or focal mural hypoenhancement, indicating ischemia (Figure 9). Differential diagnoses include inflammatory bowel disease, enteritis, ischemic bowel, and malignancy. Imaging also plays an essential role in diagnosing complications such as intussusception, perforation, and obstruction.[23,37]

Lupus Vasculitis

Systemic lupus erythematosus (SLE) is a chronic autoimmune inflammatory condition with a broad spectrum of manifestations, including vasculitis, which can lead to severe morbidity and mortality. [38] Cutaneous lupus vasculitis (19-28%) presents with palpable purpura, petechiae, splinter hemorrhages, and superficial ulcerations. [39] Neuropsychologic SLE secondary to vasculitis (31%) presents with multiple high T2-weighted/FLAIR focal lesions in the subcortical white matter and basal ganglia in MRI.[40,41] Lupus enteritis (0.2-14.2%) presents with dilated bowel, focal, or diffuse bowel-wall thickening, abnormal bowel-wall enhancement, engorged mesenteric vessels, ascites, and lymphadenopathy in abdominal CT (Figure 10). Renal vasculitis coexisting with lupus nephritis increases the risk of end-stage renal disease.[42] Pulmonary vasculitis often leads to diffuse alveolar hemorrhage with ground-glass opacifications and pleural effusions in chest CT.[43]

Conclusion

Vasculitis represents a complex spectrum of disorders characterized by inflammation of blood vessels. Given its myriad presentations in the emergencies and potential for severe complications, timely and accurate diagnosis is paramount.

Although tissue biopsy remains definitive, its limitations underscore the critical role of imaging in diagnosis within emergency settings.

Radiologists equipped with a deep understanding of vasculitis' imaging manifestations are essential to the diagnostic and management process. Collaborative efforts, melding clinical and radiological insights, are vital for optimal outcomes for emergent cases of vasculitis.

References:

1) Jatwani S, Goyal A. Vasculitis. *StatPearls*. 2023.

2) Sreih AG, Cronin K, Shaw DG, et al. Diagnostic delays in vasculitis and factors associated with time to diagnosis. *Orphanet J Rare Dis*. Apr 21 2021;16(1):184. doi:10.1186/s13023-021-01794-5

3) Ha HK, Lee SH, Rha SE, et al. Radiologic features of vasculitis involving the gastrointestinal tract. *Radiographics*. May-Jun 2000;20(3):779-94. doi:10.1148/radiographics.20.3.g00mc02779

4) Suresh E. Diagnostic approach to patients with suspected vasculitis. *Postgrad Med J*. Aug 2006;82(970):483-8. doi:10.1136/pgmj.2005.042648

5) Bahrami M, Mohammadi H, Mirgaloyebayat H, et al. The role of 18F-fluorodeoxyglucose PET/computed tomography in the diagnosis and monitoring of large vessel vasculitides - a review article. *Am J Nucl Med Mol Imaging*. 2023;13(4):127-135.

6) Guggenberger KV, Bley TA. Imaging in vasculitis. *Curr Rheumatol Rep*. Jun 19 2020;22(8):34. doi:10.1007/s11926-020-00915-6

7) Broncano J, Vargas D, Bhalla S, Cummings KW, Raptis CA, Luna A. CT and MR imaging of cardiothoracic vasculitis. *Radiographics*. Jul-Aug 2018;38(4):997-1021. doi:10.1148/rg.2018170136

8) Aghayev A. Multimodality imaging of large-vessel vasculitis, from the AJR special series on inflammation. *AJR Am J Roentgenol*. 2022;218(2):213-222. doi:10.2214/ajr.21.26150

9) Prieto-González S, Arguis P, Cid MC. Imaging in systemic vasculitis. *Curr Opin Rheumatol*. Jan 2015;27(1):53-62. doi:10.1097/bor.0000000000000130

10) Winkler A, True D. Giant cell arteritis: 2018 review. *Mo Med*. Sep-Oct 2018;115(5):468-470.

11) Pepper K. Giant cell arteritis. *Postgrad Med*. Jan 2023;135(sup1):22-32. doi:10.1080/00325481.2023.2190288

12) Ecclestone T, Watts RA. Classification and epidemiology of vasculitis: emerging concepts. *Best Pract Res Clin Rheumatol*. Jul 17 2023:101845. doi:10.1016/j.berh.2023.101845

13) Spira D, Kötter I, Ernemann U, et al. Imaging of primary and secondary inflammatory diseases involving large and medium-sized vessels and their potential mimics: a multitechnique approach. *AJR Am J Roentgenol*. Mar 2010;194(3):848-56. doi:10.2214/ajr.09.3367

14) Rutter M, Bowley J, Lanyon PC, Grainge MJ, Pearce FA. A systematic review and meta-analysis of the incidence rate of Takayasu arteritis. *Rheumatology (Oxford)*. Nov 3 2021;60(11):4982-4990. doi:10.1093/rheumatology/keab406

15) Serra R, Butrico L, Fugetto F, et al. Updates in pathophysiology, diagnosis and management of Takayasu Arteritis. *Ann Vasc Surg*. 2016/08/01/ 2016;35:210-225. doi:https://doi.org/10.1016/j.avsg.2016.02.011

16) Pugh D, Karabayas M, Basu N, et al. Large-vessel vasculitis. *Nat Rev Dis Primers*. Jan 6 2022;7(1):93. doi:10.1038/s41572-021-00327-5

17) Barra L, Kanji T, Malette J, Pagnoux C. Imaging modalities for the diagnosis and disease activity assessment of Takayasu's arteritis: A systematic review and meta-analysis. *Autoimmunity Reviews*. 2018/02/01/ 2018;17(2):175-187. doi:https://doi.org/10.1016/j.autrev.2017.11.021

18) Esatoglu SN, Hatemi G. Takayasu arteritis. *Curr Opin Rheumatol* 2022;34(1)

19) Tsujioka Y, Handa A, Nishimura G, et al. Multisystem imaging manifestations of Kawasaki Disease. *RadioGraphics*. 2022;42(1):268-288. doi:10.1148/rg.210070

20) Hoang MP, Park J. Vasculitis. *Hospital-Based Dermatopathology*. Feb 29 2020:245-96.

21) Srinivasan R, Weller R, Chelliah A, Einstein AJ. Multimodality cardiac imaging in a patient with Kawasaki Disease and Giant Aneurysms. *Case Rep Pediatr*. 2016;2016:4298098. doi:10.1155/2016/4298098

22) Singhal M, Singh S, Gupta P, Sharma A, Khandelwal N, Burns JC. Computed tomography coronary angiography for evaluation of children with Kawasaki Disease. *Curr Probl Diagn Radiol.* 2018/07/01/ 2018;47(4):238-244. doi:https://doi.org/10.1067/j.cpradiol.2017.09.013

23) Amouei M, Momtazmanesh S, Kavosi H, Davarpanah AH, Shirkhoda A, Radmard AR. Imaging of intestinal vasculitis focusing on MR and CT enterography: a two-way street between radiologic findings and clinical data. *Insights Imaging*. Sep 4 2022;13(1):143. doi:10.1186/s13244-022-01284-7

24) Venkatanarasimha N, Irani F. Polyarteritis Nodosa. *Radiology*. 2023/03/01 2022;306(3):e221255. doi:10.1148/radiol.221255

25) Jee KN, Ha HK, Lee IJ, et al. Radiologic findings of abdominal polyarteritis nodosa. *AJR Am J Roentgenol*.. 2000;174(6):1675-1679. doi:10.2214/ajr.174.6.1741675

26) Bixio R, Orsolini G, Fassio A, Rossini M, Viapiana O. Clinical image: ultrasound findings and magnetic resonance imaging comparison in the muscular involvement in polyarteritis nodosa. *Clin Rheumatol*. 2023/03/01 2023;42(3):967-969. doi:10.1007/s10067-022-06461-z

27) Cleary JO, Sivarasan N, Burd C, Connor SEJ. Head and neck manifestations of granulomatosis with polyangiitis. *Br J Radiol*. Mar 1 2021;94(1119):20200914. doi:10.1259/bjr.20200914

28) Li J, Li C, Li J. Thoracic manifestation of Wegener's granulomatosis: computed tomography findings and analysis of misdiagnosis. *Exp Ther Med*. Jul 2018;16(1):413-419. doi:10.3892/etm.2018.6154

29) Garlapati P, Qurie A. Granulomatosis with polyangiitis. *StatPearls*. 2023.

30) Allen SD, Harvey CJ. Imaging of Wegener's granulomatosis. *Brit J Radiol*. 2007/09/01 2007;80(957):757-765. doi:10.1259/bjr/34705892

31) Kitching AR, Anders H-J, Basu N, et al. ANCA-associated vasculitis. *Nat Rev Dis Primers* 2020/08/27 2020;6(1):71. doi:10.1038/s41572-020-0204-y

32) Sacoto G, Boukhlal S, Specks U, Flores-Suárez LF, Cornec D. Lung involvement in ANCA-associated vasculitis. *La Presse Médicale*. 2020/10/01/ 2020;49(3):104039. doi:https://doi.org/10.1016/j.lpm.2020.104039

33) Yaseen K, Mandell BF. ANCA associated vasculitis (AAV): a review for internists. *Postgrad Med J*. 2023/01/02 2023;135(sup1):3-13. doi:10.1080/00325481.2022.2102368

34) Roache-Robinson P, Hotwagner DT. Henoch-Schonlein Purpura. *StatPearls*. 2023.

35) Reamy BV, Servey JT, Williams PM. Henoch-Schönlein purpura (IgA vasculitis): rapid evidence review. *Am Fam Physician*. Aug 15 2020;102(4):229-233.

36) Glasier CM, Siegel MJ, McAlister WH, Shackelford GD. Henoch-Schonlein syndrome in children: gastrointestinal manifestations. *AJR Am J Roentgenol*.1981/06/01 1981;136(6):1081-1085. doi:10.2214/ajr.136.6.1081

37) Nota ME, Gökemeijer JD, van der Laan JG. Clinical usefulness of abdominal CT-scanning in Henoch-Schönlein vasculitis. *Neth J Med*. Mar 1995;46(3):142-5. doi:10.1016/0300-2977(94)00059-i

38) Calle-Botero E, Abril A. Lupus Vasculitis. *Curr Rheumatol Rep*. 2020/08/26 2020;22(10):71. doi:10.1007/s11926-020-00937-0

39) Sharma A, Dhooria A, Aggarwal A, Rathi M, Chandran V. Connective tissue disorder-associated vasculitis. *Curr Rheumatol Rep*. 2016/04/20 2016;18(6):31. doi:10.1007/s11926-016-0584-x

40) Cohen D, Rijnink EC, Nabuurs RJ, et al. Brain histopathology in patients with systemic lupus erythematosus: identification of lesions associated with clinical neuropsychiatric lupus syndromes and the role of complement. *Rheumatology (Oxford)*. Jan 2017;56(1):77-86. doi:10.1093/rheumatology/kew341

41) Shibuya M, Leite CDC, Lucato LT. Neuroimaging in cerebral small vessel disease: Update and new concepts. *Dement Neuropsychol*. Oct-Dec 2017;11(4):336-342. doi:10.1590/1980-57642016dn11-040002

42) Leone P, Prete M, Malerba E, et al. Lupus Vasculitis: an overview. *Biomedicines*. Nov 5 2021;9(11)doi:10.3390/biomedicines9111626

43) Amarnani R, Yeoh SA, Denneny EK, Wincup C. Lupus and the lungs: the assessment and management of pulmonary manifestations of systemic lupus erythematosus. *Front Med (Lausanne)*. 2020;7:610257. doi:10.3389/fmed.2020.610257


Leaders on the Horizon
2023

The 2024 Leaders on the Horizon Residents' Program

This exclusive program is designed to identify, cultivate, and highlight the future stars in medical imaging.

Radiology residents are invited to submit clinical research articles with a focus on any imaging modality or areas related to medical imaging. All articles will be reviewed and considered for publication in a special supplement to *Applied Radiology*.

The winning authors will receive:

- A trip to RSNA where they will be honored at a special reception.
- A scholarship award to support their educational endeavors in medical imaging.

Submission Deadline: September 15, 2024

Scan the QR Code for more details and complete the online registration to submit your topic and a brief description of your article(s).

For more information, visit appliedradiology.com/leaders

This educational opportunity is supported by Bracco Diagnostics, Inc.

BRACCO

LIFE FROM INSIDE

LIFE FROM INSIDE